PASSIVE MACHINE AUGMENTED COMPOSITE FOR MULTIFUNCTIONAL PROPERTIES

A Dissertation

by

JONG HYUN KIM

Submitted to the Office of Graduate Studies of
Texas A&M University
in partial fulfillment of the requirements for the degree of

DOCTOR OF PHILOSOPHY

August 2005

Major Subject: Mechanical Engineering

PASSIVE MACHINE AUGMENTED COMPOSITE FOR MULTIFUNCTIONAL PROPERTIES

A Dissertation

by

JONG HYUN KIM

Submitted to the Office of Graduate Studies of
Texas A&M University
in partial fulfillment of the requirements for the degree of

DOCTOR OF PHILOSOPHY

Approved by:

Chair of Committee,	Terry S. Creasy
Committee Members,	Hung-Jue Sue
	James G. Boyd
	Roger Morgan
Head of Department,	Dennis O'Neal

August 2005

Major Subject: Mechanical Engineering

ABSTRACT

Passive Machine Augmented Composite for

Multifunctional Properties.

(August 2005)

Jong Hyun Kim, B.S.; M.S., Inha Unversity Korea;

M.S., University of Southern California

Chair of Advisory Committee: Dr. T.S. Creasy

This dissertation studies by experiment and numerical analysis an advanced composite material (Machine Augmented Composite or MAC) for enhancement of the passive damping while maintaining its stiffness. This MAC is composed of a pre-buckled wall structure placed within a viscoelastic matrix. The pre-buckled machine can contain viscous fluids for additional energy dissipation.

For the experiments, the MAC was fabricated by using rigid and soft polyurethane as a machine and matrix material respectively. Various viscosity fluids (0.83 ~ 4730 cps) filled the inner-channel of the machine structure. Dynamic properties such as tan δ and the loss modulus (E") of the composite were measured and compared with those of a homogeneous matrix sample over a frequency range of 0.1 to 100 Hz at room temperature through load-controlled cyclic testing. Measured tan δ and loss modulus values for the composite were higher than those of the matrix alone in the 1 to

40 Hz range. However the viscous fluid effects on the overall damping properties were small.

The performance of a theoretical MAC was explored through numerical analysis. The amount of inner-channel gap closure was calculated for various matrix Poisson's ratios, for various Young's modulus ratios between the machine and matrix ($E_{machine}/E_{matrix}$), and for the volume fraction of the machines. The most desirable performance of the composite was obtained when the matrix Poisson's ratio was 0.49, and there was interaction between the $E_{machine}/E_{matrix}$ and the volume fraction of the machines. Also the proper volume fraction range of the machine was predicted to be between 0.15 and 0.2 for the lamina shape MAC.

Based upon the analysis, a sandwich structure MAC was fabricated and tested. This composite showed 11 times higher stiffness than the matrix without loosing the matrix damping property.

This dissertation shows that the research met these objectives: 1) the MAC concept is effective for passive damping of vibrations, 2) that material combinations studied here had optimal combinations for best performance, and 3) that this is a promising field study for future passive and active materials development.

DEDICATION

To Jesus, my parents, my academic advisor, Dr. Terry S. Creasy, my brother, my wife, Inmee, and my daughters, Seayeon and Saerynn.

.

ACKNOWLEDGEMENTS

This document would not have been possible without the encouragement and help from Dr. Terry S. Creasy. My first and deepest appreciation is given to him for his guidance throughout my graduate studies and life in College Station, TX.

I am grateful to my parents for their love, support, encouragement, and prayers. I also thank my wife, Inmee, for her support and encouragement, and my two daughters.

I am also deeply thankful to Dr. Sue, Dr. Morgan and Dr. Boyd for their final proofing of this dissertation. I give my gratitude to my office mates, Sangjin, Adam, and McCutcheon for their assistance while finishing my study. I also give thanks to the technicians Matt and Jeff, in the WERC testing lab for their help in my experiments.

TABLE OF CONTENTS

CHAPTER Page

CHAPTER Page

LIST OF FIGURES

FIGURE Page

FIGURE Page

FIGURE Page

FIGURE Page

FIGURE Page

FIGURE Page

FIGURE Page

LIST OF TABLES

CHAPTER I

INTRODUCTION

The research contained in this dissertation is a collection of preliminary steps on a path that could lead to novel passive and active synthetic multifunctional materials based upon incorporating mesoscale to microscale machines within an advanced composite. These machines can be wholly newly engineered structures or have a foundation in the active structures found in living plants and animals. This dissertation provides the first experiments dealing with one 'machine augmented' material and the first detailed analytical look at the impact of material parameters on the design and use of one particular material.

The research performed here was directed toward making a soft elastomer into a structural material while maintaining as much of its inherent damping as possible. At the same time, the structural material must contain channels that can support an other function or functions, for example, additional energy dissipation by fluid pumping, thermal management by fluid circulation or self repair by autonomic release of a 'healing' fluid. We start with the motivation for creating these advanced materials.

1.1. Motivation

Hawkins [1] suggested that multifunctional composites might be created by adding simple, microscale machines to the mixture of fibers and matrix.

Dissertation style and format follow that of Composite Structures.

Composite materials are widely used because of their high specific strength, their high specific stiffness, and their anisotropic and heterogeneous character. They have tailorable properties as well as viscoelastic characteristics that render them suitable for high performance structural application such as aerospace and automobile structures [2]. However, the damping of fiber reinforced composite materials is often too low for many applications and some form of damping treatment usually required [2].

This is more important and necessary in the aerospace industry because noise from rocket engines can cause vibration and subsequent failure of satellite equipment. During the initial phase of a rocket launch high velocity gases exit from the motor nozzles -- the 3 main engines of the space shuttle develop over 37 million horsepower -- and reflect from the ground. This creates turbulence in the surrounding air and a vibratory response of the rocket structure [3, 4]. During the subsequent ascent phase of a launch and, as the vehicle accelerates through the atmosphere to high velocity, aerodynamic turbulence induces pressure fluctuations that also cause structural vibration [3]. Finally, the engine themselves vibrate the entire structure while they are burning.

This environment places severe stress on flight hardware and it has been shown to severely impact subsystem reliability. The fluctuating pressures associated with acoustic energy during launch can cause vibration of structural components over a broad frequency band ranging from about 20 Hz to 10,000 Hz and above [3]. Such high frequency vibration can lead to rapid structural fatigue. The failure modes produced by acoustic noise excitation are similar to those associated with other types of vibratory structural fatigue and electronic components whose function depends on the motion of

structural parts, such as relays and pressure switches are particularly susceptible [3]. To minimize these hazardous vibration and acoustic noise problems, researchers try to damp the structure and the materials.

Damping is the capacity of a mechanical system to reduce the intensity of a vibratory process. It is also defined as significant dynamic parameter for vibration and sound control, fatigue endurance, and impact resistance [5]. The damping effect for a vibratory process is achieved by transforming or dissipating mechanical energy of the vibratory motion into other types of energy, which is most frequently heat that can be evacuated from system [6, 7, 8, 9, 10].

There are two approaches on improving the damping properties of structures. One is passive damping and the other is active damping. Through active damping more precise and smart damping control can be possible, but active damping requires sensors, controllers, and actuators. These sub-systems make the active damping system complicated and expensive. Because of these costs, passive damping is the major means of suppressing unwanted vibrations.

1.2. Status of the Field

One method of damping an aerospace structure is by placing acoustic blankets on the interior of the structure [6]. The absorption coefficient of the blanket is a function of the material, thickness, and excitation frequency. Typically, the absorption coefficient increases linearly with frequency until it reaches a peak between 300 and 500 Hz and falls off dramatically at higher frequencies as a function of $1/f^5$ where f is the frequency

[6]. The motivation for active acoustic attenuation in the payload fairing is the limited low frequency effectiveness of added mass and acoustic blankets. Acoustic blankets are less effective at low frequencies because lower frequencies require thicker blankets and 2 to 4 inch thick blankets are effective to approximately 300 to 400 Hz. Below those frequencies, the wavelength of sound are too long to be trapped in the blankets and dissipated as heat [6].

There are other ways of enhancing the damping properties of dynamic structures by modification of composite structures. The technology of composite materials has experienced rapid development in the last two decades due to significant progress in materials science and technology in the area of fibers, polymers, and ceramics [11]. For over 50 years, composite materials have been made by embedding fibers or particulates in a matrix material [1]. And for fiber-reinforced composites, the fibers supply special properties such as strength and stiffness to the composite, while the matrix holds the fibers in place and transfer loads among them.

Recently a new concept, which is called Machine Augmented Composite (MAC) was introduced [1]. It utilized specially designed, small, Z-shaped machines as reinforcements in place of some fibers. These machines converted compression displacement into shear deformation. The previous research [1] suggested that this MAC concept could be applied to vibration and noise absorption by applying different types of machines. To this purpose a novel machine, which has two pre-buckled walls to pump a viscous fluid, was proposed. This machine is the focus of this research.

1.3. Objectives

This study has these objectives:

- Experimentally demonstrate and validate the performance of a passive machine augmented composite.
- Numerically explore the performance of the HG-MAC over a range of material design parameters to determine these things:
    1. Is it possible to damp vibration by this method?
    2. Is there an optimum combination of parameter for best performance?
    3. Is this method a promising path for future materials development?

CHAPTER II

LITERATURE REVIEW

This chapter presents a concise summary of the relevant literature with respect to damping in materials and structures. It includes emerging reports of novel materials – such as negative Poisson's ratio – and the analysis of energy dissipation in a fluid-filled machine augmented composite. We begin this chapter by defining damping and discussing method of measuring it.

2.1. Definition of Damping

Damping is the capacity of a mechanical system to reduce the intensity of a vibratory process. The damping effect for a vibratory process is achieved by transforming or dissipating the mechanical energy of the vibratory motion into another type of energy, which is most frequently heat that can be evacuated from system [6, 7, 8, 9]. Damping occurs at the material level – inherent – and at the structural level.

In deformation of a hard solid such as diamond, atoms are displaced from equilibrium positions in fields of force which are quite local in character [12]. In a polymer, on the other hand, each flexible threadlike molecule pervades an average volume much greater than atomic dimensions and is continuously changing the shape of its contour as it wriggles and writhes with its thermal energy. Rearrangements of molecular chains on local scale are relatively rapid, but on a long-range scale, it is very slow. Under stress, new distribution is rapid, the response to the long-range aspects is

slow [12]. Because of these characteristics of polymeric materials, these materials show the in-between characteristics of hard materials and purely viscous (liquid like) materials.

2.2. Measurement of Damping Properties

There are several methods for characterizing the damping of a material. One way of calculating the damping is measuring the phase angle δ by which the resulting sinusoidal stress vector lags the applied sinusoidal strain vector and then calculating what is known as $\tan \delta$ [13, 14, 15]. Figure 2.1 (a), (b), and (c) display the resulting stress for an applied strain of a pure elastic material, a purely viscous material, and a viscoelastic material respectively. A purely elastic material is one in which all the energy stored in the material during loading is returned when the load is removed and, as a result, the stress and strain curves are completely in phase. A purely viscous material does not return any of the stored energy during loading and the resulting stress is completely out of phase with strain.

A viscoelastic material shows both elastic and viscous characteristics and if a sinusoidal force acts on the material the resulting strain will be sinusoidal at the same frequency, but the response is somewhat out of phase like Figure 2.1 (c). The same phase shift holds true if the strain is the input and the stress is the output.

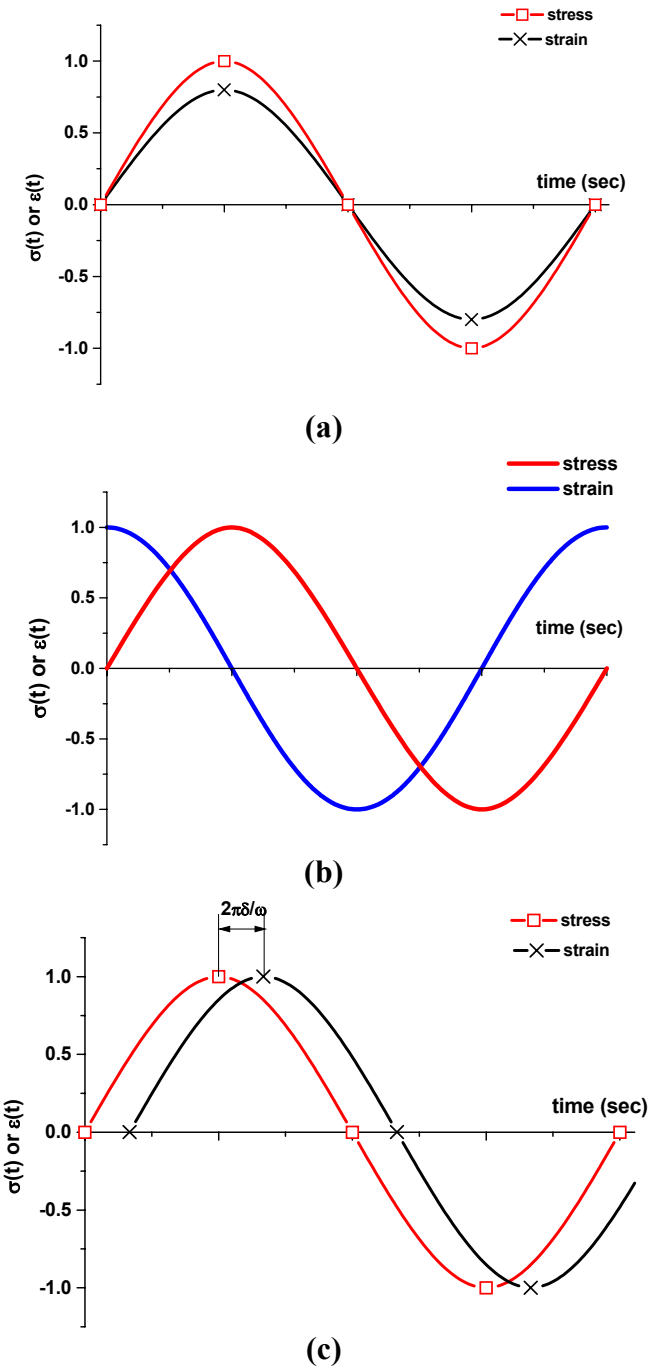

Figure 2.1. Sinusoidal stress and strain of a purely elastic material (a), a purely viscous material (b), and a viscoelastic material (c) at the same frequency. δ is the time (Δt), ω is the circular frequency (rad/s), f is a frequency (Hz) and $\omega = 2\pi f = 1/T$, $\omega t = 2\pi$.

For example, if we apply the strain into a Maxwell spring and dashpot system, the resulting stress will be

$$\varepsilon = \varepsilon_0 \sin(\omega t) \tag{2.1}$$

$$\sigma = \sigma_0 \sin(\omega t + \delta) \tag{2.2}$$

where ω is the circular frequency (radians/sec) and t is the time (sec). When we expand equation (2.2) using the trigonometric identity:

$$\sin (a \pm b) = \sin(a)\cos(b) \pm \cos(a)\sin(b) \tag{2.3}$$

we can show that

$$\sigma = (\sigma_0 \cos\delta)\sin\omega t + (\sigma_0 \sin\delta)\cos\omega t \tag{2.4}$$

Now we can divide Eq. 2.4 by ε_0 and define new modulus values

$$\frac{\sigma}{\varepsilon_0} = (E'\sin\omega t + E''\cos\omega t) \tag{2.5}$$

where $E' = \frac{\sigma_0}{\varepsilon_0}\cos\delta$ is the storage modulus of the material (stiffness of materials) and

$E'' = \frac{\sigma_0}{\varepsilon_0}\sin\delta$ is the loss modulus of the material.

Also the loss modulus E" in equation (2.5) is related to the average power dissipated as heat [15]

$$\dot{W} = \frac{\pi(\varepsilon_0)^2 E''}{2\pi/\omega} = \frac{1}{2}(\varepsilon_0)^2 E''\omega \tag{2.6}$$

The physical meaning of E" in equation (2.6) can be explained by these examples:

Small E" helps to minimize both the energy dissipated and the heat built up in the system. This situation is good for a tire because high temperature causes rapid degradation and wear of the tire as it wastes gasoline.

Large E" dissipates considerable vibration energy as heat rather than transmitting it through the system. This is good for automobile engine block mounts because the unwanted vibration can be absorbed before it reaches the passengers [14].

We define the ratio of E" and E' to be

$$\tan\delta = \frac{E''}{E'} \tag{2.7}$$

Mechanical vibration damping can be defined as the ratio of energy dissipated (D) to the maximum strain energy (W) per cycle of vibration. Energy ratio units are summarized in terms of loss factor η by this equation: [2]

$$\eta = \frac{D}{2\pi W} = \frac{\psi}{2\pi} = \frac{E''}{E} = \tan\varphi = \frac{C}{C_c} \tag{2.8}$$

where η = damping factor or loss factor

D = unit damping energy; specific damping energy; energy dissipated per unit volume per cycle

W = maximum strain energy stored during a cycle = $\sigma^2/2E$

ψ = specific damping capacity

E" = loss (or imaginary) modulus of elasticity

E = storage (or elastic) modulus

φ = angle (phase) by which sinusoidal stress vector lags sinusoidal strain vector in linear system

C/C_c = damping ratio of linear system

C = equivalent linear damping coefficient

C_c = critical damping coefficient for system

2.3. Damping in Homogeneous Materials

2.3.1. Damping of Metals

Numerous and extensive investigations have shown that the interior damping of a metal is strongly affected by relatively small changes in the metal's structure such as may be caused by cold rolling, heat treatment, and irradiation [16]. The physical processes that produce damping in metals are intricate and not yet fully understood. The primary mechanisms responsible for the damping of metals are associated with dislocations in the crystal lattice and with heat conduction between differently strained regions [16].

Table 2.1 [9, 16] summarizes the experimentally measured damping of metals and polymers. With the exception of some compliant metals such as lead and tin, the loss factors of metals in general are considerably smaller than 0.001 [9, 16]. But the great differences in the damping of materials are of little importance for practical structures, because the actual damping of such structures is determined not by the losses in the materials, but by the fraction at supports, interfaces, connections etc. [16].

2.3.2. Damping of Polymers

The mechanical properties of amorphous high polymers characteristically exhibit a very broad transition region between the rigid and the liquid state. In this transition region the long and possibly cross-linked or entangled chains of molecules become increasingly mobile and there occur relaxation mechanisms which lead to loss factors up to 10 [16]. The moduli of elasticity and the loss factors of such materials depend strongly on temperature and frequency.

In addition, all plastics have a glass transition temperature (Tg) and increases with increasing frequency [16, 17]. Below the glass transition temperature, most high polymers have a small loss factor which is less than 0.1 [16]. Above the glass transition temperature there is a rubber-elastic region and, in this region, plastics exhibit rather high loss factors and this is shown in Figure 2.2. In addition, one may obtain significant changes in the temperature-variation of the properties of polymer by adding plasticizers to them [16]. From this behavior one may obtain materials with optimized damping behavior over a prescribed temperature and frequency regions by using appropriate combinations of cross-linked polymers, fillers, and plasticizers.

Table. 2.1. Damping property of metal and polymer materials [9, 16].

Material	Frequency (Hz)	Tan δ	Testing temperature (^{o}C)	Testing method
Metal				
Aluminum	0.1 ~ 10	10×10^{-5}	N/A	N/A
Al 2024-T4	100	7×10^{-4}	N/A	Bending
Al 6063-T6	N/A	5×10^{-4} ~ 5×10^{-3}		
Copper (pure, annealed)	20 ~ 550	2.5×10^{-3} ~ 8×10^{-4}	-73	N/A
Brass	50 ~ 600	3×10^{-3} ~ 6×10^{-3}	N/A	N/A
Iron (pure, cold drawn)	0.83	2×10^{-3} ~ 2×10^{-2}	70	Torsion
Iron alloy (0.001% C)	1	2×10^{-5} ~ 6×10^{-5}	N/A	Torsion
Stainless Steel	N/A	2×10^{-3} ~ 1.5×10^{-2}	N/A	Torsion
Iron alloy (ALSI 403)	N/A	2×10^{-3} ~ 7×10^{-2}	N/A	Torsion
Lead (pure)	20 ~ 160	8×10^{-3} ~ 1.4×10^{-2}	N/A	Bending
Magnesium (pure, casting)	60 ~ 400	6×10^{-2} ~ 1.4×10^{-2}	N/A	Bending
Nickel (pure, casting)	N/A	1.5×10^{-4} ~ 4×10^{-3}	N/A	Torsion
Platinum (pure)	N/A	8×10^{-5}	N/A	N/A
Silver(annealed)	N/A	5×10^{-6} ~ 9×10^{-6}	-23	N/A
Titanium (pure)	0.5	1×10^{-3} ~ 7×10^{-2}	550	N/A
Tungsten (pure)	0.1	2.2×10^{-4}	N/A	N/A
Zinc	1 ~ 5	1.9×10^{-3}	N/A	N/A
Polymer				
Nylon	0.001 ~ 100	0.076 ~ 0.048	30	N/A
Polyethyl Methacrylate	200	0.07	20	Bending
Polyethylene	12	0.23	60	N/A
Polyethyl Chloroacrylate	200	0.02	20	N/A
Polymethyl Methacrylate	0.001 ~ 400	0.021 ~ 0.0196	25	N/A
Polypropylene	10	0.095	20	N/A
Polystyrene	0.1	0.019	25	N/A
Polyvinyl Acetate	500	0.486	10	Torsion
Rubber (vulcanized)	4000	1.5	All range	N/A
Rubber (gum stock)	0.1 ~ 1	0.15 ~ 0.43	20	N/A

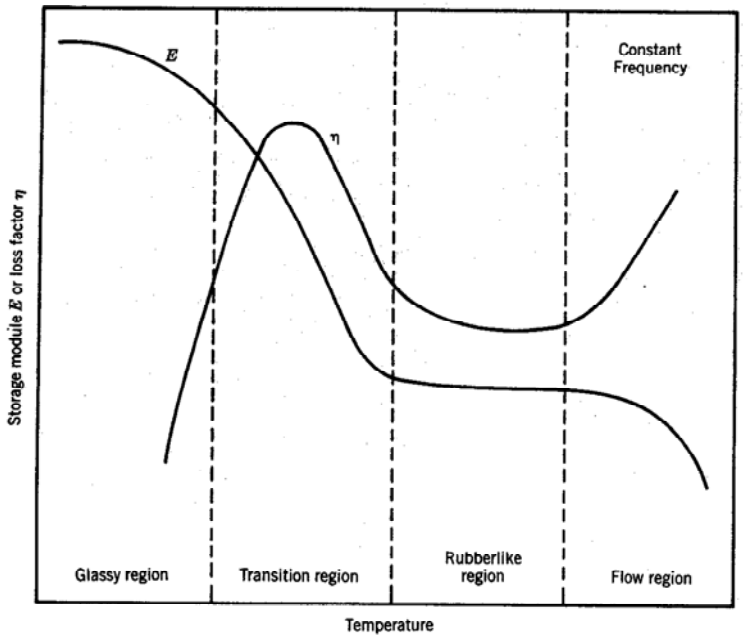

Figure 2.2. Variation of the storage modulus and loss factor with temperature. The vertical axis is a log scale [17].

Figure 2.3 displays typical stiffness and damping properties of some structural materials [18]. One thing to remember about Figure 2.3 is that all materials shown are isotropic materials. Composite materials, which show anisotropic characteristics, are not listed in this figure. With proper structure design and material selections, stiff but high damping composite structures might be fabricated.

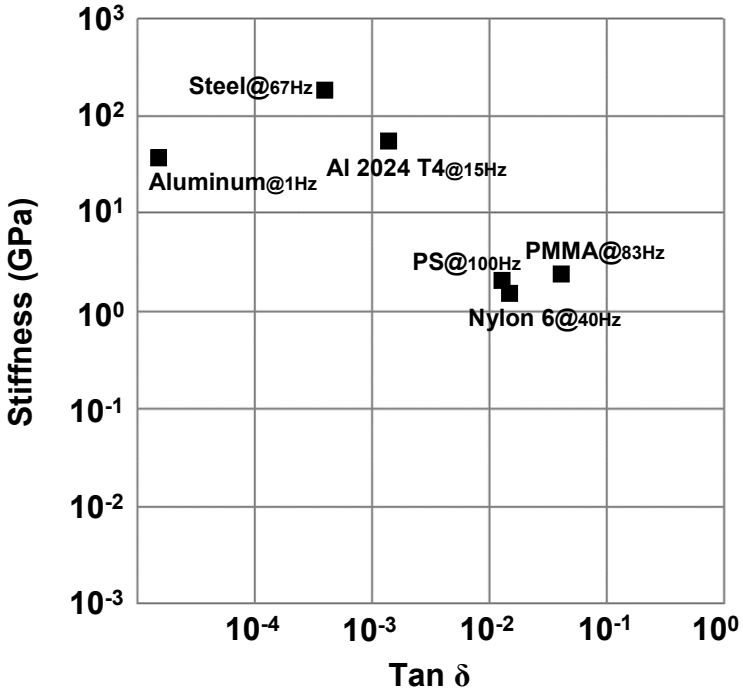

Figure 2.3. Stiffness-loss map of observed behavior of some common materials [18].

2.4. Damping in Composite Materials

This section reviews the basic composite damping mechanisms as well as several analytical approach methods such as micromechanical and macromechanical approaches for understanding the damping of fiber-reinforced composite materials.

2.4.1. Introduction

Polymer matrix composites are known to exhibit significantly higher material damping than most common metals as a result of their heterogeneity [5]. Also, the viscoelastic character of composites render them suitable for high performance structural applications like aerospace, marine, and automotive structures [2]. Since composites are

already preferred in many structural applications due to their high specific stiffness and strength, adding passive structural damping would provide an added advantage to these materials [5].

2.4.2. Composite Damping Mechanisms

Damping mechanisms in composite materials differ entirely from those in conventional metals and alloys. Since the composite is not homogenous like metals and moreover since the matrix – and sometimes fibers – shows highly viscoelastic characteristics, composite materials have complicated damping mechanisms. Also, some previous research demonstrates that composite damping depends on an array of micromechanical and laminate parameters: temperature, moisture, and existing damage [5]. Fiber-reinforced composites dissipate energy by these five methods: [2]

(a) Inherent viscoelastic nature

(b) Interphase damping

(c) Damage damping

(d) Viscoplastic damping

(e) Thermoelastic damping

We next discuss each of these contributions to damping.

First, the matrix and the fiber might be viscoelastic. The major contribution to composite damping can be caused by the matrix. However, fiber damping must be included in the analysis for Kevlar fiber; it has high damping when compared to other fibers. Kevlar fiber is damping coefficient typically is of the same order of magnitude as

the matrix damping coefficient. For carbon and glass fiber composites the fiber behavior may be considered as purely elastic [19].

Also, carbon or glass fiber composite materials have a reversely proportional relationship between damping and the composite's Young's modulus [19]. For Kevlar fiber composite the experimental damping factor is in practice independent of the composite Young's modulus – at least in the range of 6 to 70 GPa [19].

The second source of damping is composite has the interphase. The interphase is the region between fiber and matrix and, because each constituent has different properties, this region plays an important role in damping. Namely, the interphase possesses a considerable thickness [20] and its properties are different from those of both embedded fibers and matrix. Cinquin et al. [21] observed that improving interface bonding decreases damping.

The third damping source in a composite is damage. Energy dissipation in the area of matrix cracks, broken fibers etc. can increase the damping [22]. Also the frictional slippage between fiber and matrix interface or delamination is another source of damping.

The fourth energy dissipation mechanism in composites is viscoplasticity. At large amplitudes of vibration and at high stress levels thermoplastic composite materials exhibit an evident degree of non-linear damping due to the high stress and strain concentrations that exist in local regions between fibers [23]. Thus the elasto-plastic micromechanical behavior is important even for applied stresses that are intended to remain below the apparent elastic limits of composite materials [2].

Finally, the fifth mechanism is thermoelastic damping. This is caused by cyclic heat flow. Thermoplastic composites show high temperature rise that is a function of applied load, frequency, sample thickness, and number of cycles [24].

Composite damping – like other mechanical properties of composite materials – is also anisotropic, but damping exhibits an opposite anisotropy trend from stiffness and strength. Damping has a minimum in the direction of the fibers and maximum in the transverse and shear directions. Also, the structural composite damping was found to be strongly dependent on structural configuration options such as lay up angle, fiber volume fraction, and deformation state [5].

2.4.3. Analytical Prediction of Damping of Composite Materials

Numerous analytical models for predicting damping at the micromechanical, the macromechanical, and the structural level are based on the assumption of linear viscoelasticity and on a basic mechanics of material and elasticity approaches. There are two approaches in this category; one is the correspondence principle and the other is the strain energy method.

The correspondence principle [2] states that the linear elastostatic analysis can be converted to dynamic linear viscoelastic analysis by replacing static stresses and strains with corresponding dynamic stresses and strains, and by replacing elastic moduli or compliances with complex moduli or compliances, respectively. Some general assumptions are that fibers are elastic and nondissipative and that the matrix is elastic in dilation but viscoelastic in shear.

The strain energy method [2, 25, 26] is related to both macromechanical and micromechanical approaches. It is mainly used in micromechanical analysis. The basic assumption is that composite damping strongly depends on the matrix properties rather than those of the fiber i.e., fibers are purely elastic materials.

2.4.3.1. Macromechanical Approach

For the macromechanical approach the individual lamina is the element whose strain and dissipation energies combine to give the overall loss factor of the laminate. The Adam–Bacon criteria [2] states that the energy dissipated in a thin unidirectional lamina is the sum of the separate energy dissipated due to longitudinal stress, to transverse stress, and to shear stress. Consequently, the specific damping capacity can be defined as the ratio of energy dissipated to strain energy stored. It has been observed that in polymeric reinforced composites nonlinear behavior is more significant in shear and in the transverse direction to the fiber due to considerable straining of resin [2]. In addition, defects such as voids, impurities, and imperfections in resin to fiber bonding or debonding are the points of stress concentration that increase damping and add to nonlinearity.

However most of the work on macromechanical damping studies in composite materials relates to prediction of the effect of factors like: fiber orientation, laminate configuration, frequency, and stress dependence of damping rather than considering constituent element effects.

2.4.3.2. Micromechanical Approach

In themicromechanical approach the elements include the constituents such as fibers, matrix, fiber-matrix interaction, void content, and the interphase.

Micromechanical damping analysis of fiber-reinforced composites has provided better insight into the role of damping mechanisms because this approach considers constituent element effects and fiber-matrix interaction in addition to the geometrical parameters [2].

Basic assumptions are that the energy of the composite is equal to the dissipated strain energy of the components, the matrix and fiber exhibit linear viscoelastic behavior that a uniform state of stress exists in the composite, and that there are no interaction stresses concerning damping in material coordinates.

The most widely used analysis method in micromechanics is the strain energy method. The strain energy method states that for any system of linear viscoelastic elements the loss factor can be expressed as a ratio of summation of the product of individual element loss factors and the strain energy stored in each element to the total strain energy [2, 25, 26]. In other words, the whole composite damping can be expressed as this equation [25]:

$$\Psi_C = \frac{\Delta U}{U} \tag{2.9}$$

where ψ_c is the specific damping capacity of the composite, ΔU is the energy dissipated during a stress cycle, and U is the maximum stored strain energy

The energy dissipation of the composite can be separated into three components associated with longitudinal (σ_L), transverse (σ_T), and shear (σ_{LT}) stress as stated by this equation:

$$\Delta U = \Delta U_L + \Delta U_T + \Delta U_{LT} \tag{2.10}$$

We can express each term in Equation (2.10) by these relations:

$$\Psi_L = \frac{\Delta U_L}{U}$$
$$\Psi_T = \frac{\Delta U_T}{U}$$
$$\Psi_{LT} = \frac{\Delta U_{LT}}{U} \tag{2.11}$$
$$\Psi_C = \Psi_L + \Psi_T + \Psi_{LT}$$

where Ψ_L, Ψ_T , Ψ_{LT} are the specific damping capacity in the longitudinal direction, in the transverse direction, and shear direction respectively. Ψ_C is the specific damping capacity of whole composite system.

The specific damping capacity Ψ_{LT} caused by a longitudinal shear (twisting of a bar of an aligned composite) of unidirectional composites can be defined by this equation [26]:

$$\Psi_{LT} = \frac{\Psi_m (1 - V_f)\left|(G+1)^2 + V_f (G-1)^2\right|}{\left|G(1+V_f) + 1 - V_f\right|\left|G(1-V_f) + 1 + V_f\right|} \tag{2.12}$$

where f and m represent fiber and matrix, V_f is the fiber volume fraction, G is the ratio of the shear modulus of the fiber to that of the matrix.

Also the specific damping capacity Ψ_L can be formulized by longitudinal tension/compression tests with this result [26]:

$$\Psi_L = \Psi_m (1 - V_f) \frac{E_m}{E_f} \tag{2.13}$$

where E_m and E_f are the Young's modulus of matrix and fiber respectively.

However, it was found that [26] this expression considerably underestimates the measured value of Ψ_L even when considerable effort has been made to eliminate extraneous loses. Basically, there are several factors contributing to composite damping such as diameter of fibers – which increases in Ψ_L with reduced in fiber diameter due to increase in surface area of fiber per unit volume – cracks, misalignment of fibers and etc. Therefore, to expect precise damping properties other environmental parameters should be considered.

The specific damping capacity in the transverse direction (Ψ_T) is heavily matrix dependent [26]. There is no reliable micromechanics theory for predicting Ψ_T. Many experiments show that transverse damping is largely independent on both fiber type and surface treatment, but, volume fraction of fiber also has a significant effect on Ψ_T [26].

While the various micromechanics theories are sufficiently accurate for predicting moduli, they are generally poor at predicting damping. This is because the various theories do not contain some of the important factors such as microcracks, misalignment, and surface area, which contribute significant effect on damping while having little effect on the moduli [26].

2.5. Method for Damping of Structures

2.5.1. Introduction to Damping Design

The vibrational response of a structure or machine may be controlled in many ways. If it is made particularly stiff and massive, the fundamental frequency may be high enough to limit all vibrations to a level that can be accepted. However the cost of such an approach is usually too high.

Nowadays structures tend to be as light as can be [27]. Therefore, advanced damping system design is necessary more than ever before to meet today's complicated and cost effective structural applications.

The first step to the designing a damping treatment is to determine of how much damping is needed to deal with a given problem. This question cannot be solved unless there exists an understanding of how much damping is in the original structure [17]. To illustrate this matter, consider the difference in structural response between built up structures and welded or integrally machined structures.

Built-up structures are joined by mechanical fasteners such as rivets, bolts, and screws. Examples of such structures are the riveted skin-stringer structures used in aircraft fuselage construction and complex diesel engine blocks [17]. Built-up structures usually have high initial structural damping due to friction in joint to joint damping and to measured loss factor is as high as 0.05 [17]. However, the loss factor of the integrally machined or welded structures such as muffler shells and blades are only 10^{-4} or 10^{-5} for steel or aluminum structures [17]. Therefore, in the design these types of initial structural damping characteristics should be considered first and different damping treatments and

approaches have to be taken to get the best damping results of the structures. In this sub-chapter, two different ways of damping methods; passive damping and active damping approaches to the dynamic structure systems will be reviewed.

2.5.2. Passive Damping

Passive damping is now the major means of suppressing unwanted vibrations. All passive damping treatments share two common goals: to absorb significant amounts of strain energy in the modes of interest and to dissipate this energy through some mechanism [10]. Passive damping may be divided into two classes: inherent and designed-in [10]. Inherent damping exists in a structure due to friction in its joints, intrinsic material damping, rubbing of cables, and etc. Designed-in damping refers to passive damping added to a structure by design. Designed-in passive damping is usually based on one of four damping mechanisms: viscoelastic absorption, viscous flow, magnetic eddy current losses, or passive piezoelectric energy generation [10].

Viscoelastic materials (VEMs) are widely used for passive damping in both commercial and aerospace applications. Viscoelastic materials are elastomeric materials whose long-chain molecules cause them to convert mechanical energy into heat when they are deformed.

Viscous devices dissipate energy via a velocity dependent mechanism, typically by forcing a fluid through a precision orifice. Table 2.2 [10] summarizes these mechanisms briefly. Also Table 2.3 [10] illustrates the primary implementations of passive damping and associated design methods for structures.

Table 2.2. Primary passive damping mechanisms and related information [10].

	Type of Damping Mechanism			
	Viscoelastic materials	**Viscous devices**	**Magnetic devices**	**Passive Piezoelectrics**
Types of treatment	**All**	**Structures & TMDs**	**Structures & TMDs**	**Structure Dampers**
Temperature sensitivity	**High**	**Moderate**	**Wide**	**Wide**
Temperature range	**Moderate**	**High**	**Wide**	**Wide**
Loss factor	**Moderate**	**High**	**Low**	**Low**
Frequency range	**Wide**	**Moderate**	**Moderate**	**Moderate**
Weight	**Low**	**Moderate**	**High**	**Moderate**

Table 2.3. Primary implementations of passive damping and associated design methods for structures [10].

	Type of treatment					
	Strut/Link dampers	**Constrained layers**	**Tuned-Mass dampers**	**Interface dampers**	**Embedded Dampers**	**Free layers**
Target modes	**Global**	**Member bending & extension**	**Narrow frequency range, Any mode shape**	**Local or Global**	**Member bending & extension**	**Member bending & extension**
Primary design method	**Modal Strain energy**	**Modal strain energy**	**Complex eigenvalues**	**Joint test or Modal strain energy**	**Modal strain energy**	**Modal strain energy**
Special features	**Removable/ Light weight**	**Flexible**	**Low cost /Low weight**	**Low weight Low volume**	**Embedded**	**Low cost Easy design**

One of the simplest passive damping methods, but the least weight effective, is the unconstrained or free-layer damping treatment. In this treatment high modulus, high loss-factor material is applied to a surface of the vibrating structure [16]. Free layer treatments must be fairly thick in order to absorb sufficient amounts of strain energy, and are therefore not weight efficient.

Constrained layer treatments are surface treatments where the damping material is sandwiched between the base structure and a constraining layer. The constraining layer causes shear in the damping material as the structure deforms. The next sections provide details about these treatment strategies.

2.5.2.1. Free-layer Damping Treatment

Extensional damping is one of the most commonly used treatments; sometimes this treatment is referred to as the unconstrained or free-layer damping treatment [17]. This treatment is coated on one or both sides of a structure, so that whenever the structure is subjected to cyclic bending, the damping material will be subjected to tension-compression deformation. [17] This type of damping treatment is illustrated in Figure 2.4.

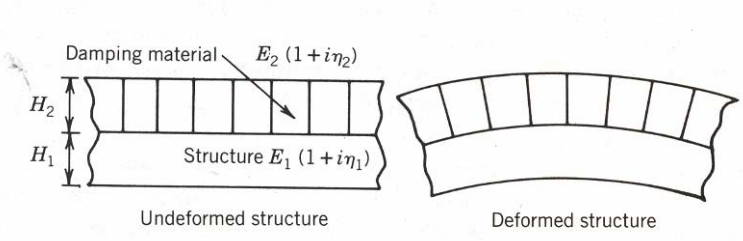

Figure 2.4. Free-layer damping concept and its deformed shape [17].

The governing equation of deformation of surface damping treatment structures was developed by Ross, Ungar, and Kerwin (RKU analysis) [28] and the basic assumption of this RKU analysis is that the structure (beam or plate) is simply supported, the connections between the layers are rigid and the damping of the base structure is zero [17].

For this free-layer damping treatment, the governing equations are [17]:

$$\frac{EI}{E_1 I_1} = \frac{1 + 4(E_2/E_1)h_2 + 6(E_2/E_1)h_2^{\,2} + 4(E_2/E_1)h_2^{\,3} + (E_2/E_1)h_2^{\,4}}{1 + (E_2/E_1)h_2} \tag{2.14}$$

$$\frac{\eta}{\eta_2} = \frac{(E_2/E_1)h_2\{3 + 6h_2 + 4h_2^{\,2} + 2(E_2/E_1)h_2^{\,3} + (E_2/E_1)^2 h_2^{\,4}\}}{(1 + E_2/E_1\, h_2)(1 + 4(E_2/E_1)h_2 + 6(E_2/E_1)h_2^{\,2} + 4(E_2/E_1)h_2^{\,3} + (E_2/E_1)h_2^{\,4})} \tag{2.15}$$

where E is the Young's modulus of elasticity, I is the second moment of inertia, $h_2 = H_2/H_1$, H is the layer thickness, η is the loss factors and subscript 1 refers to the base structure, subscript 2 to the damping layer and no subscript refers to the composite system.

According to these two equations, the optimum damping properties of the free-layered damping treatment structure is affected by several design and environment factors such as temperature, thickness ratio, frequency etc.

The maximum loss factor is achieved when the product of E_2 and the loss factor η_2 is a maximum and this product is a maximum in the transition region of the viscoelastic materials therefore it is expected that the performance of the unconstrained layer damping treatment, as a function of temperature, will be a maximum only in such a region [10]. However, one can broadening the temperature range over which high damping can be achieved by selecting several materials with different properties.

For the thickness of damped layer, as we increasing the thickness of the viscoelastic material, higher damping can be achieved in the system. And again, the damping of the composite system depends on the product of E_2 and the loss factor η_2, the damping layer must not only thick and have a high loss factor and high modulus of elasticity as possible [16]. Therefore, soft materials, such as felt or soft rubber are not good for structural damping. Useful damping materials generally consist of filled high-polymer plastics. However, it is also evident that this increase in damping is not a linear function of thickness. This is because if the damping material thickness is much greater than that of a structure, the composite system damping approaches that of viscoelastic material itself, and it is not possible to obtain higher composite damping than that of the viscoelastic materials [17]. Also as the thickness of damping material increases, the temperature at which the damping is a maximum also increase, this is because as the thickness increases, so does the resonant frequency, especially at low temperatures. Therefore, as the thickness of the unconstrained-layer treatment increases, the resonant frequency of the system increases, and the peak damping occurs at a higher temperature [17].

The effect of frequency for many practical applications is rather small and can be ignored unless there is a need to considerably wide frequency range [17].

2.5.2.2. Constrained-layer Damping Treatment

For a given weight, the shear or constrained layer damping treatment is more efficient than the free-layer treatment [17, 29]. This treatment is similar to the free-layer type, except the viscoelastic material is constrained by metal layer.

Therefore, whenever the structure is subjected to cyclic bending, the metal layer will constrain the viscoelastic material and force it to deform in shear and this shear deformation dissipate energy. This concept is shown in Figure 2.5 [17].

This constrained-layer treatment is also affected by several external variables. For example, at low temperatures the material is in its glassy region; both the structure and the constrained layer become rigidly coupled. Little shear deformation occurs in the middle layer, and hence the energy dissipation is also small [17]. At high temperature the viscoelastic material is in its rubbery region and soft. Both the structure and constrained layer become almost uncoupled. The energy dissipation in this case is also minimal even though the shear deformation in the middle layer is high. If the temperature is high enough the shear modulus of the middle layer is low [17]. So the constrained-layer damping design should consider this temperature effect.

The maximum shear deformation in the middle layer is a function of the modulus, the thickness of the constraining layer, the thickness of damping layer, the wavelength of vibration, and the properties of the damping material [17]. Usually, it is desirable to have the constraining layer as stiff as possible to introduce the maximum shear strains into the

viscoelastic layer. However, the constraining layer stiffness should not exceed that of the base structure. Therefore the maximum amount of shear strains is usually accomplished whenever the constraining layer is of the same type and geometry as that of the base structure to be damped [17] like the sandwich damping treatment in Figure 2.5 (b).

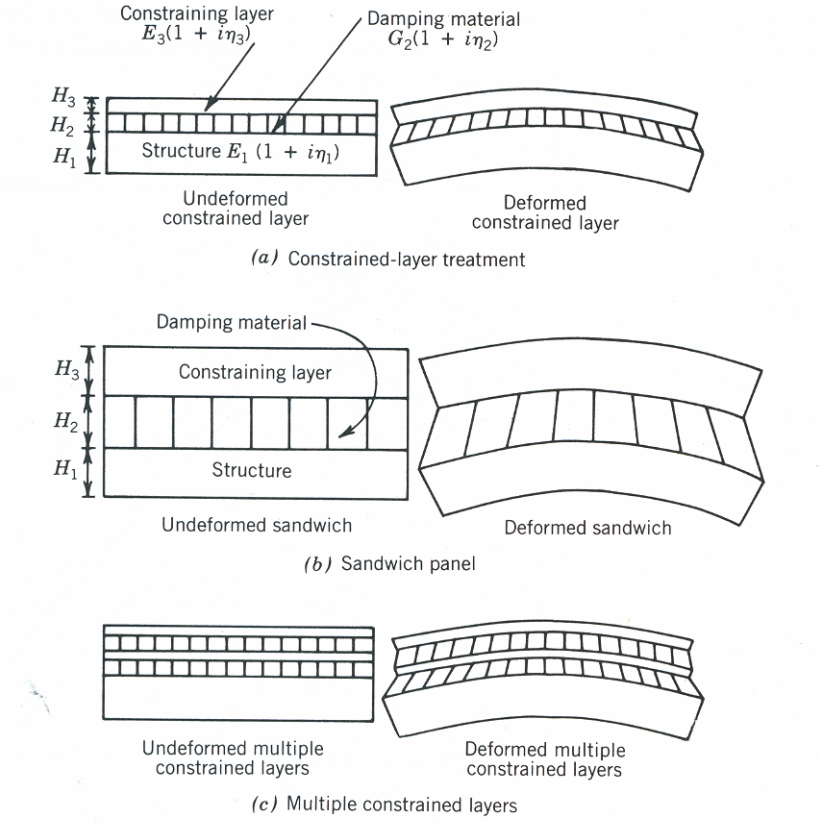

Figure 2.5. Various constrained damping treatments (a) constrained-layer treatment (b) sandwich panel (c) multiple-constrained layers [17].

Another important difference between free-layer and constrained-layer damping treatment is the loss factor of the constrained-layer plates with viscoelastic interlayer is

somewhat frequency dependent whereas the free-layer damping treatment is frequency independent [16]. This frequency-dependence comes about because the cover plate is stretched more at low frequency whereas at high frequencies, the bending energy increases more rapidly than the shear energy [16]. The frequency at which maximum damping occurs depends on the shear modulus, on the thickness of the cover plate, on the flexural wavelength, and thus also on the properties of the base plate [16].

Also for a single-layer treatment, the damping is proportional to the product of E_2 and the loss factor η_2, but the damping of constrained-layer treatments does not vary as the product $E_2\eta_2$ [16]. In fact, the shear modulus of viscoelastic layer does not affect the magnitude of the loss factor maximum and the shear modulus of viscoelastic layer only determines the frequency at which this maximum occurs [16].

In summary, constrained-layer plates with viscoelastic interlayers deform in shear and the magnitude of the maximum loss factor depend on the loss factor of the viscoelastic material (but not on its shear modulus), on the moduli of elasticity of the base plate and the cover plate, and on the dimensions. Also use of a spacing layer again enables one to increase the loss factor considerably [16].

2.5.3. Active Damping

Active damping uses sensors to measure the response at each instant and actuators automatically apply forces to oppose the measured vibration response in a prescribed manner [10]. Figure 2.6 illustrates the concept of an active system [30].

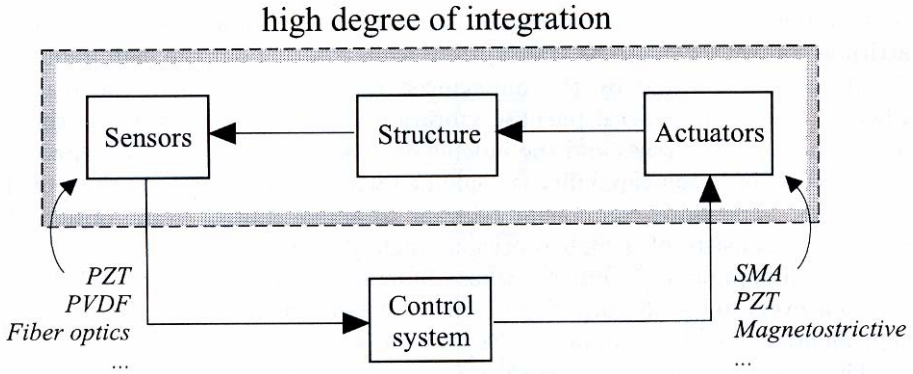

Figure 2.6. Schematic diagram of active system [30].

The sensor detects the external conditions, and the controller generates proper signal to drive the actuators. The process cycles until the optimum damping condition is achieved.

Piezoelectric material actuators (piezo-ceramics, piezo-polymers) are widely used because the properties of these materials can be changed according to the input signal. Figure 2.7 shows two basic types of piezoelectric actuators [30]. The length of the bodies can be changed actively.

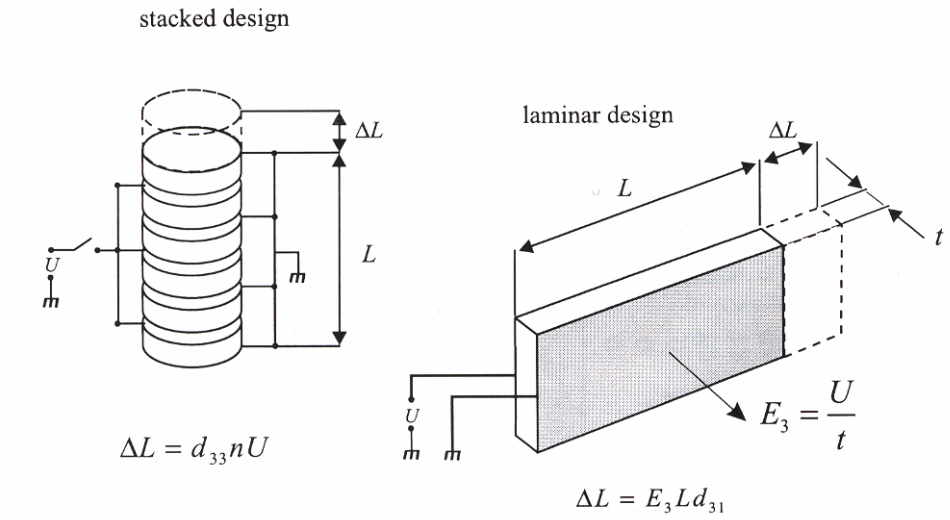

Figure 2.7. Piezoelectric actuator (a) stacked design (b) lamina design [30].

2.6. Negative Poisson's Ratio Structures

Poisson's ratio (υ) is defined as the ratio of transverse contraction/extension to longitudinal extension/contraction strain (ε) in the direction of stretching force. And the Poisson's ratio can be expressed in this equation [31, 32, 33, 34]:

$$\upsilon = -\frac{\varepsilon_{trans}}{\varepsilon_{longitudinal}} \tag{2.16}$$

For isotropic, homogeneous materials, the range of Poisson's ratio is between -0.5 and 1, because for the material to be stable, the bulk modulus (K) and shear modulus (G), which are defined as equation (2.17) and equation (2.18) must be positive [31, 32, 33, 34].

$$K = \frac{E}{3(1-2\upsilon)} \tag{2.17}$$

$$G = \frac{E}{2(1+\upsilon)} \tag{2.18}$$

where E is the Young's modulus of the material and this value is also positive

But the mathematical and thermodynamic requirements on the elastic constants of orthotropic materials are somewhat different from those of isotropic materials because an orthotropic material has three orthogonal planes of symmetry. The six possible Poisson's ratios (υ_{12}, υ_{23}, υ_{31}, υ_{21}, υ_{32}, υ_{13}) are related each other by the ortotropic identity condition:

$$\frac{\upsilon_{ij}}{E_{ii}} = \frac{\upsilon_{ji}}{E_{jj}} \tag{2.19}$$

where ij represents directional index.

The compliance matrix of orthotropic materials is defined as

$$[S] = \begin{bmatrix} 1/E_1 & -(\nu_{21}/E_2) & -(\nu_{31}/E_3) & 0 & 0 & 0 \\ -(\nu_{12}/E_1) & 1/E_2 & -(\nu_{32}/E_3) & 0 & 0 & 0 \\ -(\nu_{13}/E_1) & -(\nu_{23}/E_2) & 1/E_3 & 0 & 0 & 0 \\ 0 & 0 & 0 & 1/G_4 & 0 & 0 \\ 0 & 0 & 0 & 0 & 1/G_5 & 0 \\ 0 & 0 & 0 & 0 & 0 & 1/G_6 \end{bmatrix} \tag{2.20}$$

and the stiffness matrix $[s]^{-1} = [C]$ is expressed as

$$[C]=\begin{bmatrix} (1-\nu_{23}\nu_{32})/E_2E_3\Delta & (\nu_{21}+\nu_{31}\nu_{23})/E_2E_3\Delta & (\nu_{13}+\nu_{12}\nu_{23})/E_1E_2\Delta & 0 & 0 & 0 \\ (\nu_{12}+\nu_{13}\nu_{32})/E_1E_3\Delta & (1-\nu_{13}\nu_{31})/E_1E_3\Delta & (\nu_{32}+\nu_{12}\nu_{31})/E_1E_3\Delta & 0 & 0 & 0 \\ (\nu_{31}+\nu_{21}\nu_{32})/E_2E_3\Delta & (\nu_{23}+\nu_{21}\nu_{13})/E_1E_2\Delta & (1-\nu_{12}\nu_{21})/E_1E_2\Delta & 0 & 0 & 0 \\ 0 & 0 & 0 & G_4 & 0 & 0 \\ 0 & 0 & 0 & 0 & G_5 & 0 \\ 0 & 0 & 0 & 0 & 0 & G_6 \end{bmatrix} \quad (2.21)$$

where $\Delta = \dfrac{(1-\nu_{12}\nu_{21}-\nu_{23}\nu_{32}-\nu_{13}\nu_{31}-\nu_{12}\nu_{23}\nu_{31}-\nu_{21}\nu_{32}\nu_{13})}{E_1E_2E_3}$

The sum of the work done by all stress components must be positive in order to inhibit the creation of energy. This provides a thermodynamic constraint on the elastic constants. Formally, the condition requires the elastic matrixes to be positive definite, i.e., to have positive principal values or invariants [35].

When we apply only one normal component of stress σ_{ij} at a time to the material, the strain is determined from the corresponding diagonal element of the compliance matrix. So these must all be positive elements:

$$E_1, E_2, E_3, G_4, G_5, G_6 > 0 \quad (2.22)$$

Similarly when only one normal component of strain is applied to the material, the corresponding stress is determined by the appropriate diagonal element of the stiffness matrix so that these must all be positive elements:

$$(1-\upsilon_{23}\,\upsilon_{32}) > 0,\ (1-\upsilon_{13}\,\upsilon_{31}) > 0,\ (1-\upsilon_{12}\,\upsilon_{21}) > 0 \quad (2.23)$$

$$\Delta = 1-\upsilon_{12}\,\upsilon_{21}-\upsilon_{23}\,\upsilon_{32}-\upsilon_{13}\,\upsilon_{31}-\upsilon_{12}\,\upsilon_{23}\,\upsilon_{31}-\upsilon_{21}\,\upsilon_{32}\,\upsilon_{13} > 0 \quad (2.24)$$

From the orthotropic identity Eq. (2.19) and Eq. (2.23) and (2.24), the Poisson's ratio range of an orthotropic material can be written as

$$|\nu_{12}| < (E_1/E_2)^{1/2} \qquad |\nu_{21}| < (E_2/E_1)^{1/2}$$

$$|\nu_{23}| < (E_2/E_3)^{1/2} \qquad |\nu_{32}| < (E_3/E_2)^{1/2} \tag{2.25}$$

$$|\nu_{31}| < (E_3/E_1)^{1/2} \qquad |\nu_{13}| < (E_1/E_3)^{1/2}$$

and

$$\nu_{12}\nu_{23}\nu_{31} < \frac{\{1 - \nu_{12}^{\,2}(\frac{E_1}{E_2}) - \nu_{23}^{\,2}(\frac{E_2}{E_3}) - \nu_{31}^{\,2}(\frac{E_3}{E_1})\}}{2} < \frac{1}{2} \tag{2.26}$$

This condition shows that all three Poisson's ratios cannot have large positive values at the same time, as their product must be less than one half. If one is negative, however, no restriction is placed on the other two [35].

Recently, new materials showing a negative Poisson ratio have been introduced by R. S. Lakes [36, 37, 38, 39, 40, 41] and there are many current research reports [42, 43, 44, 45, 46, 47] regarding fabrication and analysis of such materials or structures.

The meaning of negative Poisson's ratio is that structure will fatten when stretched and thin under compression and because this phenomenon is a contrast to conventional material behavior, negative Poisson's ratio materials are called anti-rubber [48].

Also since the negative Poisson's ratio materials easily undergo volume change (K << G) unlike conventional materials (K >> G), it is called dilatational material [49], or auxetic material [44]. And because these typed structures are highly anisotropic, the

range of the Poisson's ratio value is open to much larger than for isotropic structures or foams [46]. Figure 2.8 shows several negative Poisson's ratio structures and their deformation characteristics by Lakes [44] and Evans [49].

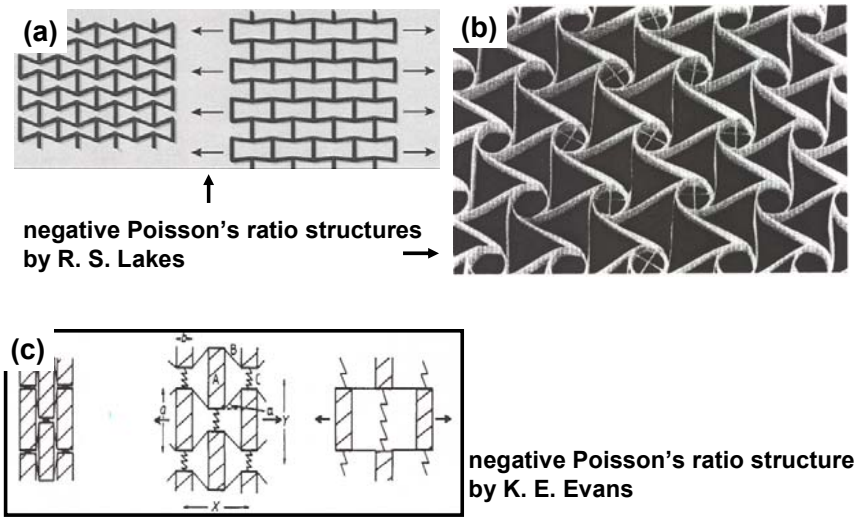

Figure 2.8. Negative Poisson's ratio structure (a), (b) by Lakes [44] (c) by Evans [49].

To achieve negative Poisson's ratio on both the honeycombs and foams, substantial porosity is required, therefore, these negative Poisson's ratio structures are substantially less stiff than the solids from which they are made and this cause limitations on the structural applications of the negative Poisson's ratio structures [8]. But negative Poisson's ratio structures show enhancement of several other mechanical properties such as shear modulus, indentation resistance or plane strain fracture toughness [1, 8, 14, 50]. Also unlike the conventional foam, which can be linearly compressed up to 5 %, these new concept structure can be compressed more than 40 %

[7]. Since in real dynamic situations, the system is continuously attacked by cyclic loading and unloading, these typed negative Poisson's ratio structures have great advantages in service life as well as absorbing the external vibrations.

2.7. Machine Augmented Composite Structures

For several decades, composite materials have been fabricated using viscoelastic matrix and many types of fibers. But these kinds of fiber-reinforced composites have limitations in many structural applications such as damping. Recently to overcome these limitations, new concept composite structure, which is based on the hierarchical composite structures; materials that contain structures of multiple-length scales with large but finite deformation [1, 51, 52, 53] has proposed and analyzed. This composite is composed of specially designed simple machines in place of some fibers or particulates typically used as reinforcements and matrix [1] and with this reason, this composite is called Machine Augmented Composites. (MAC)

The mechanical and physical properties of the MAC can be tailored easily through modification of embedded machine geometry. Through this process, material can have special properties that are not currently available with traditional materials. [1] According to the previous research on the MAC [1], simple stress-conversion machine (Z-machine) embedded MAC (Z-MAC) can convert tensile/compression force into shear forces and vice versa. Figure 2.9 shows (a) individual Z machine, (b) and (c) are Z-MAC and its deformation behavior respectively. Also like Figure 2.10, there was a linear relation between input compressive displacement and output shear displacement.

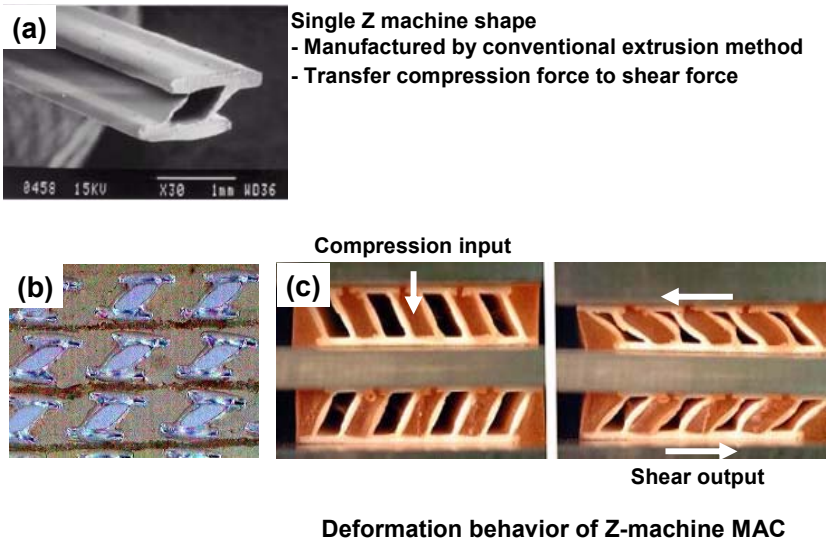

Figure 2.9. (a) Individual Z-machine, (b) Z machine embedded composite structure (c) deformation behavior of Z-MAC [1].

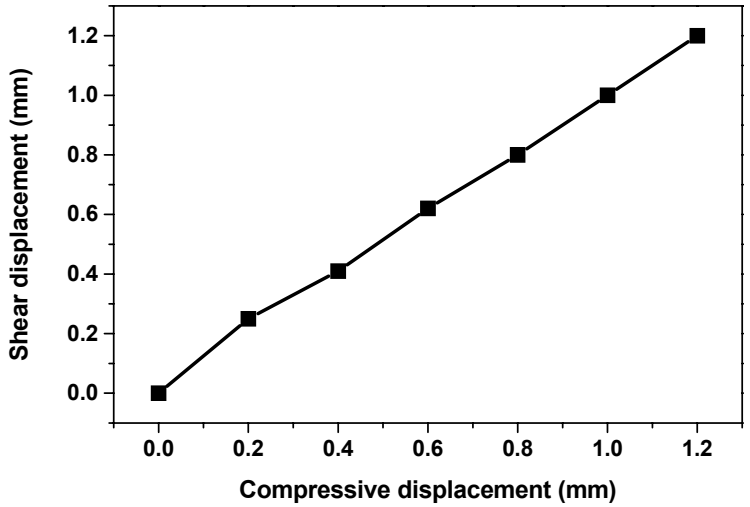

Figure 2.10. The relation between shear stress output and compressive stress input on the Z-MAC sample [1].

This research also suggested several additional machine designs and those are shown in Figure 2.11. The machine in Figure 2.11 (a) changes the modulus of the MAC in a nonlinear manner. Namely, if this machine is pulled in tension from above and below, the central arm initially bends like a cantilever beam, but after a certain strain, the arm is caught within the machine and bends as a fixed-pinned beam. Theoretically, the beam is 30 times stiffer than the cantilever and consequently the MAC would increase its stiffness. A material containing these machines would have a nonlinear modulus that could be predetermined in a controlled manner by the material architecture [1].

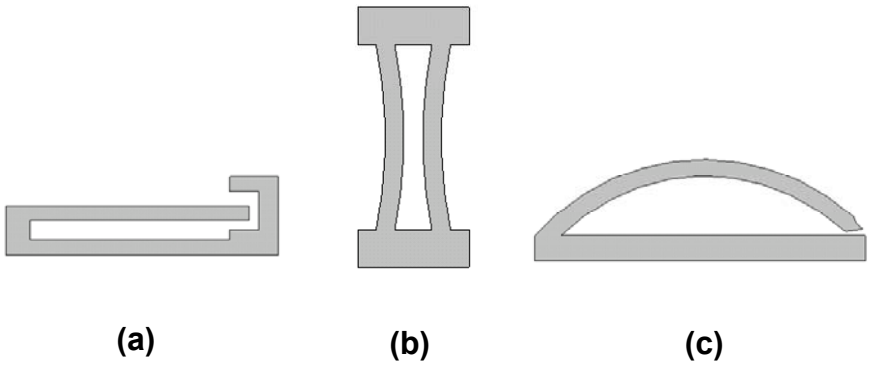

Figure 2.11. Conceptual designs of machines that when embedded in a material exhibit different mechanical properties (a) nonlinear modulus (b) negative Poisson's ratio (c) extended strain to failure can be expected. [1]

Figure 2.11 (b) shows the cross section of a machine that causes a negative Poisson's ratio and the machine shape is envisioned that absorb energy for shock absorbers. Figure 2.11 (c) is a leaf spring that controls the modulus of the material and extends a material's compressive strain or isolation bearing in building.

2.7.1. Energy Loss by Viscous Dissipation

Another work related with this study was performed numerically using different machine shape and material properties [54]. The study used a modified geometry machine shape to reduce the stress concentration at the inner corner of the channel as well as to increase the performance of fluid/solid interactions and this machine shape is displayed in Figure 2.12.

The stiffness and Poisson's ratio of his machine were 2000 MPa and 0.35 respectively and those of matrix were 30 MPa, 0.4995, and 3 MPa, 0.4995 respectively and the machine and the matrix were treated as hyperelastic materials. That is the solid material possesses no viscoelastic properties and the damping is only from viscous fluid flow.

Also, the performance of the MAC was calculated from this specific damping capacity definition:

$$\text{Energy dissipated / Energy stored} = (\text{Efficiency})_{/\text{cycle}}/[1-(\text{Efficiency})_{/\text{cycle}}] \quad (2.27)$$

This was a more convenient method of quantifying the dissipation because the reciprocating fluid flow had a variable phase shifting, i.e., the resulting stress does not lag the input strain by a constant phase angle δ like conventional case. McCutcheon's results indicate [54] that the specific damping capacity of his model reached 0.8 (maximum specific damping capacity = 1) as the product of fluid viscosity (μ) and angular frequency (ω) increase. Finally the specific damping capacity increased as the hydraulic diameter of inner-channel was decreased.

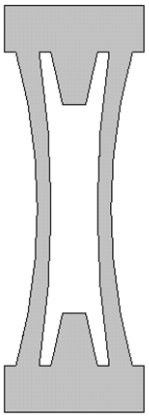

Figure 2.12. Modified HG machine shape for better performance [54].

2.7.2. Stiffened Structure that Maintains Inherent Damping

The main task of this study is create a stiffer panel that has good channel-closing performance for pumping a fluid while maintaining the inherent damping at least minimizing loss of damping.

CHAPTER III

EXPERIMENTAL PROCEDURES

In this chapter we introduce the hourglass machine augmented composite (HG-MAG) structure. These structures were built and tested as scaled up versions of the desired structures. Once the fabrication methods are presented, this chapter presents the experimental procedures for the HG-MAC. We begin by describing the HG concept.

3.1. Introduction to the HG Machine and HG-MAC

Figure 3.1 (a) shows the individual HG machine and its dimensions, which are scaled relative to the sidewall radius R. The wall thickness t and the height h may vary for the best performances but in this study, the values of t and h are fixed as 0.0385R and 0.538R respectively. The top and bottom flanges prevent the HG machine pulling out from the matrix and evenly distribute external force to the walls of the HG machine for the uniform deformation.

Figure 3.1 (b) displays the HG machine reinforced composite (lamina) and its running mechanism respectively.

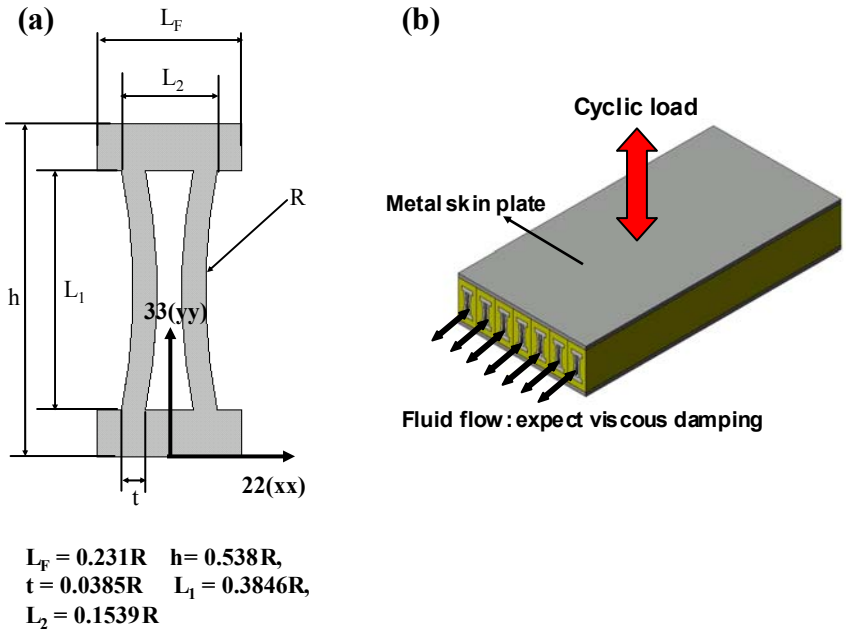

Figure 3.1. (a) Individual HG machine. (b) HG-machine embedded composite lamina under compression loading.

3.2. Fabrication Procedure of the Model HG Machine

The HG machine and other shape machines were fabricated by a room temperature injection molding technique. These machines have hollow interior channels. The molding resin was excluded from the channels by mandrels placed into the machine molds before the polymer was injected. Whole fabrication procedures are composed of several sub-steps Figure 3.2 exhibits the whole fabrication and testing procedures of this study in the flow chart format.

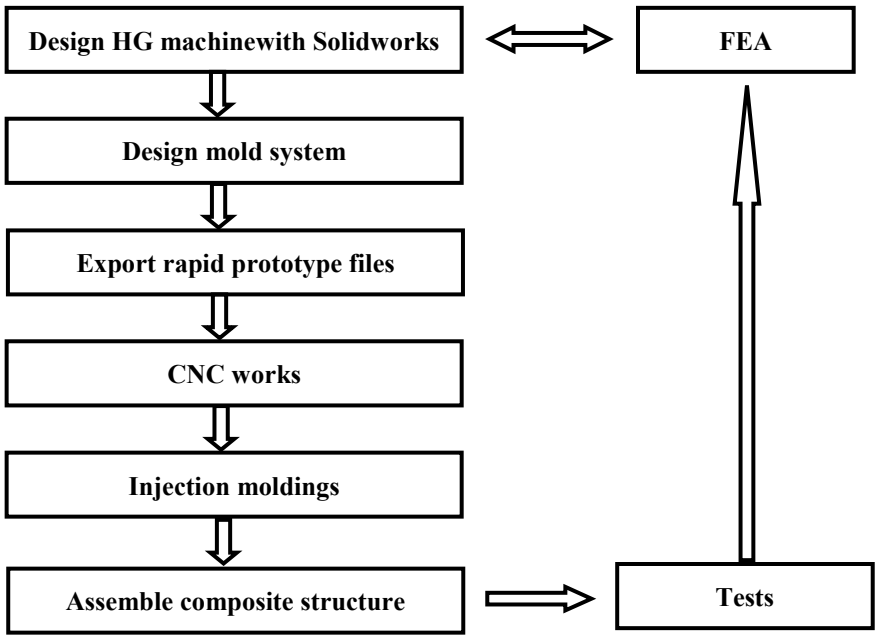

Figure 3.2. Overall fabrication and testing and analysis procedure of this study

3.2.1. Mold Design

After several attempts, we found successful mold shapes, which are shown in Figure 3.3. The workable mold size was 5 times bigger than the default size of an hourglass and at this scale the CNC machine can cut every detail part exactly same as the Solidworks design and, moreover, functional mandrels could be fabricated at this size.

Figure 3.3 (a) and (b) display the detail dimension of the half-mandrel and machine molds respectively. Each assembled mold is composed of mirror image female mold halves and the assembled mold has a 4 mm diameter polymer inlet and 1 mm diameter vent. After several attempts with different vent diameters, the 1 mm diameter

vent produced the best parts. That is, the specimen had no visible bubbles on the parts and the molds were fully filled with resin. Also, shrinkage problem of the cured polymer was not a significant factor. The indicated long rectangular portions of the mandrel mold in Figure 3.3 (a) allow the CNC to machine the full curvature of the HG machine walls. And at the time of injection molding, these negative rectangular portions were filled with exactly the same dimensional rectangular blocks that were also made by injection molding.

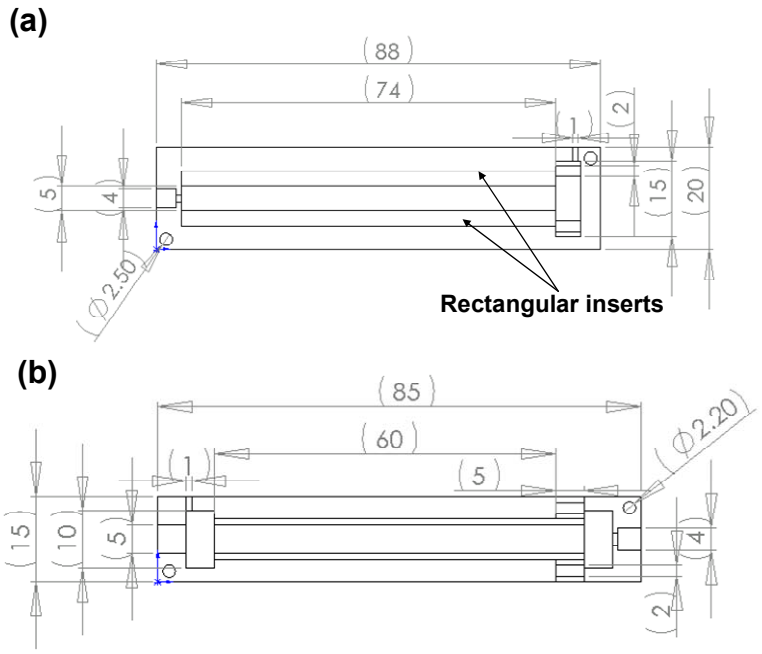

Figure 3.3. (a) Half Mandrel mold and (b) Machine mold dimensions in mm.

These mold designs were cut into green wax blocks for room temperature injection molding.

3.2.2. CNC Machining

Figure 3.4 (a), (b) and (c) show the Roland model PNC 300 CNC machine, an aluminum injection mold, and the machine in the Creasy group lab respectively.

The CNC machine can cut soft materials such as wax, brass, aluminum and thermoplastic polymer materials. Also the X, Y, and Z precision of the machine is 10 $\pm$ 1.25 μm and total workable area is 120 mm by 100 mm by 100 mm. The CNC machine is supported by the precisely surfaced stone and to minimize the vibration of the CNC machine, rubber blocks were used under the 4 corners of the CNC machine and stone. Also to hold wax or metal blocks securely, vacuum technique was applied like Figure 3.4 (c) and all machining procedures were controlled by the Modela software.

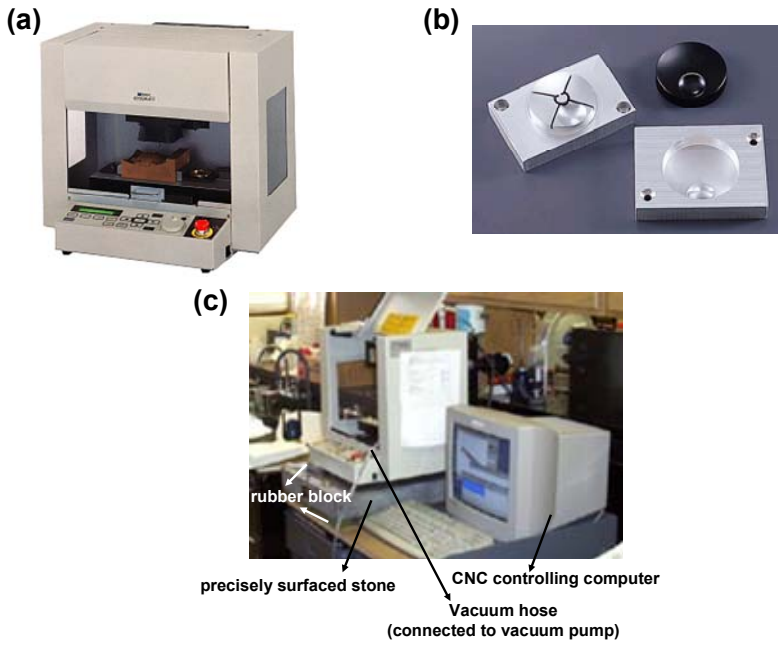

Figure 3.4 (a) CNC machine by Roland Co. (b) fine products from CNC machine (c) CNC machine set up for making parts.

Figure 3.5 shows the final shape of mandrel and machine molds by green wax block.

Figure 3.5. (a) Mandrel and (b) machine molds in a green wax block.

The first step of machining is converting Solidworks drawing file from PRT to STL file format because the CNC machine only recognizes the STL format. After that, surfacing both sides of the working block with a 6 mm diameter mill to make precise flat surfaces and then start to make parts from the draft mode for rough cut with a diameter of 2 mm mill to fine mode with a diameter of 0.381 mm using the converted STL file like conventional printing procedures.

3.2.3. Assembly and Injection Molding of Mandrel

After placing the mold-release-treated rectangular blocks into their socket of the mandrel mold, the female molds were clamped and resin was injected. Figure 3.6 illustrates this procedure. The whole injection set up is composed of several sub-parts

such as injection gun, which can generate proper pressure for resin flow, resin cartridge, mixing nozzle and clamped molds.

The resin and hardener can be mixed by desired volume fraction through resin cartridge and when the mixed resin travels the nozzle, bubbles were collapsed each other and finally bubble free parts were obtained. The resin system for mandrel and machine was rigid polyurethane (Repro 1075) and more detail information of this resin will be presented in sub section 3.2.5.

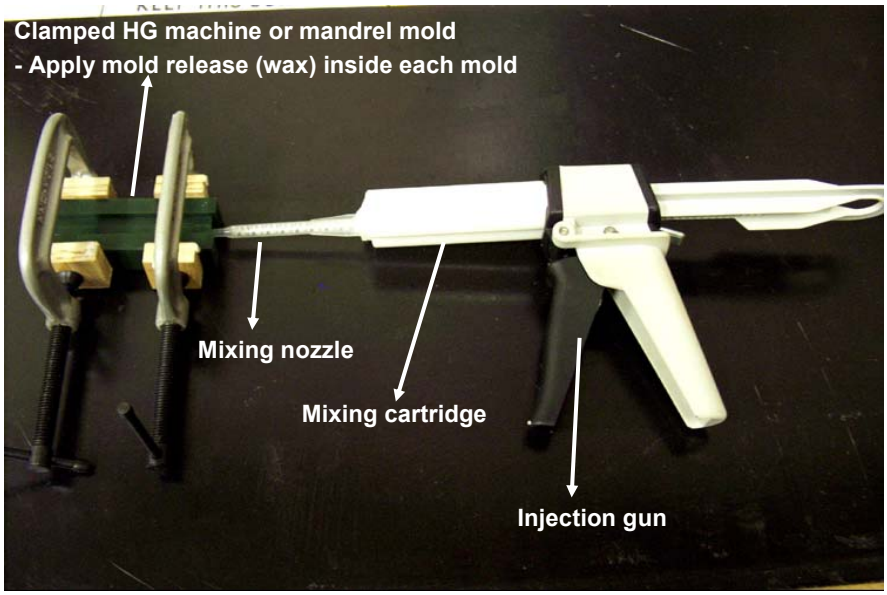

Figure 3.6. Room temperature injection molding set up.

3.2.4. Making a HG Machine

Figure 3.7 displays the step-by-step procedure of machine fabrication. After making a mandrel, the edges of mandrel were carefully smoothed with #1500 sand paper

and the surface of the mandrel was coated with release wax (Freeman wax release) to ease mandrel extraction from the cured HG machine. Surface coating of the mandrel is very important; too little coating lets the mandrel stick to the machine. Excess coating causes many small defects (holes) in the machine parts.

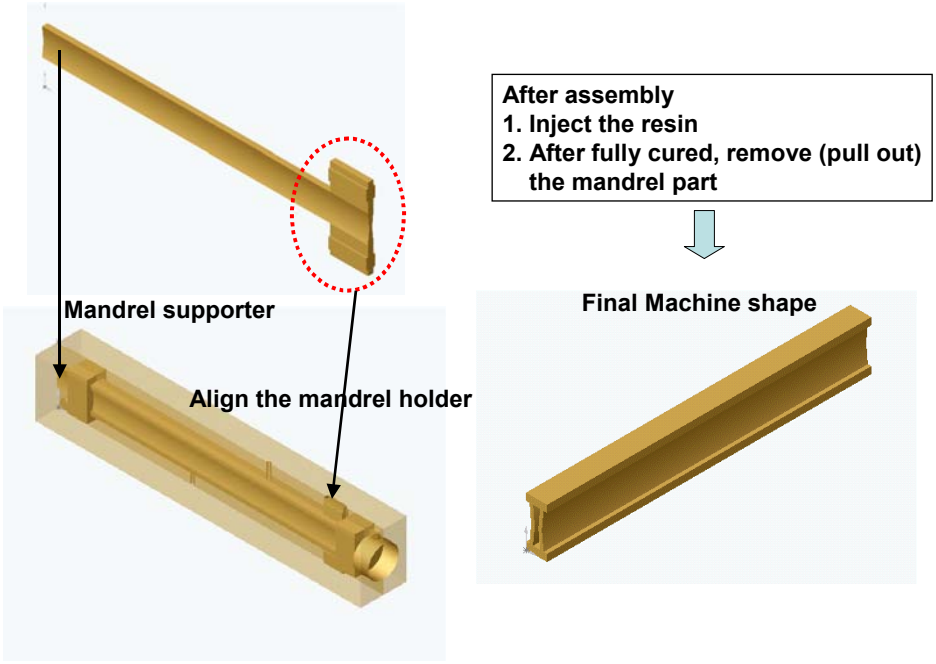

Figure 3.7. Step-by-step procedure of making a machine structure.

Figure 3.7 shows a treated mandrel assembled into the machine mold. That is, place the head and end part of the mandrel into the machine's mandrel holder and the mandrel support position and then inject the resin (Repro 1075) in the same manner with mandrel making. After curing the resin, pull out the machine from the mold and cut top portion of the machine part (mandrel holder portion) and then pull out the mandrel.

Figure 3.8 displays the history of machine fabrication with different resin systems.

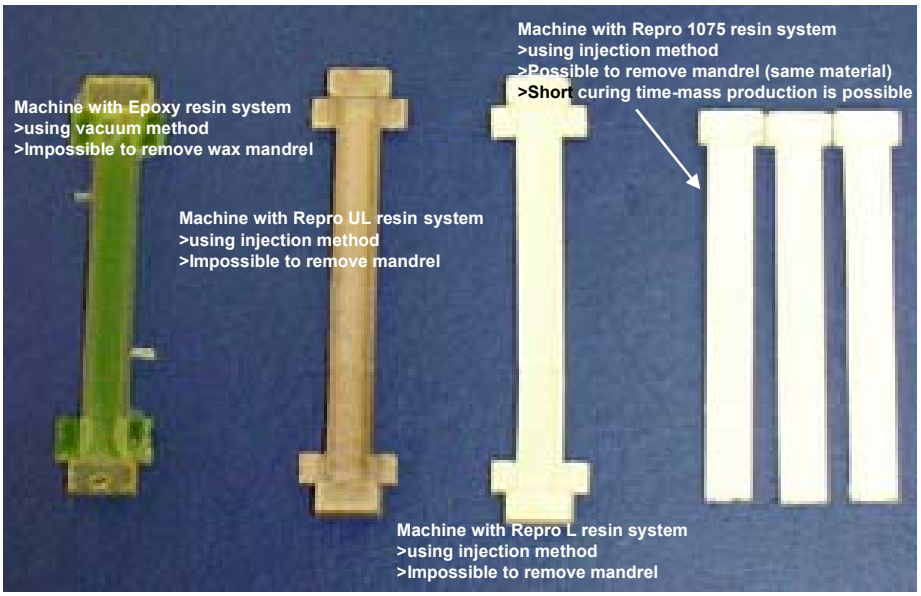

Figure 3.8. History of machine fabrication from epoxy resin to Repro 1075 rigid polyurethane.

First we tried epoxy resin system with green wax mandrel and in this case, we used 150 ^{o}C temperature oven to melt out the mandrel but the mandrel could not be fully removed due to the surface tension of the green wax and moreover the epoxy part became very brittle. For the second and third trials, Repro Ultralight (Repro UL) and Repro light (Repro L) resin system were applied and in both cases, the materials did not have proper resilience and due to this reason, the mandrel could not be pulled out successfully. Finally when we changed the material to Repro 1075 rigid polyurethane,

the mandrel could be pulled out successfully and we could make the HG machines as in Figure 3.9. All other machine shapes in Figure 3.9 were generated through the same procedure with the HG machine and the inner-channel areas and the remaining parts area of all machines were same.

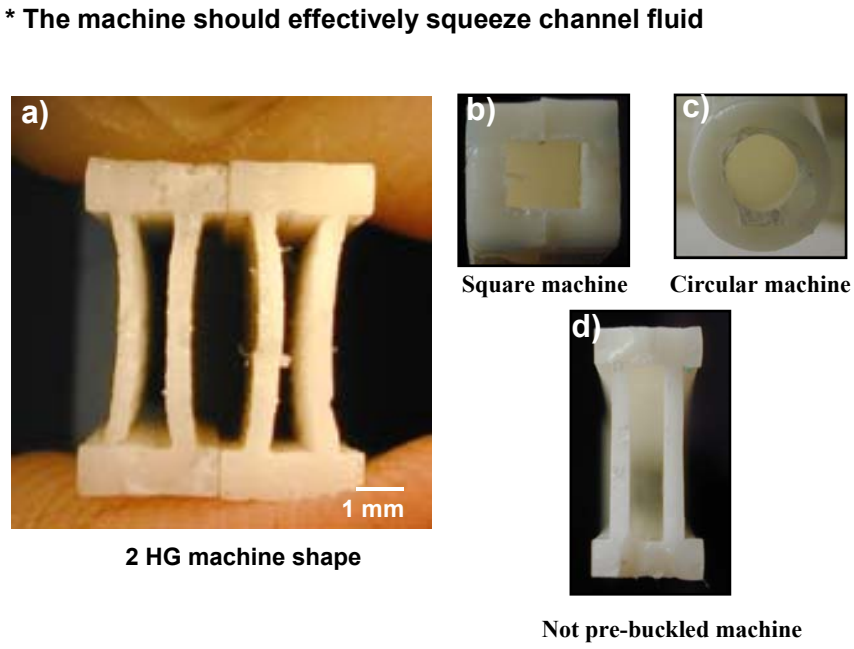

Figure 3.9. Various machines' cross sectional views (a) two HG machines, (b) square machine, (c) circular machine (d) not pre-buckled machine.

3.2.5. Material Properties of Repro 1075 Rigid Polyurethane

The required mechanical properties of the HG machine should be flexible but have some resilience property because the working environments of the HG machine is under cyclic loading and unloading at ambient temperature, the machine structure should

not broken at many cyclic loading. Also to pull out the mandrel part from the cured HG machine, the material should have proper resilience property.

To meet this requirements, similar material properties to nylon 6 is needed and Repro 1075 rigid polyurethane meet this criteria. The mechanical properties of Repro 1075 are very similar to those of nylon but the greatest advantage of the Repro 1075 resin system is that injection molding is possible at room temperature because of its low flow viscosity. (200 cps) The mixing ratio of resin to hardener of Repro 1075 was 100 : 52 by volume or 100 : 50 by weight.

The Repro 1075 resin came from Freeman Company U.S. and the mechanical properties such as ultimate tensile/compression strength and Young's modulus of this material were determined by static tension (ASTM D638-01) and compression tests (ASTM D695-96) using MTS machine with strain rate of 0.014 mm/sec.

The Poisson's ratio of Repro 1075 was also obtained by ASTM D638-01 and other properties were obtained from manufacturer's data sheet.

Figure 3.10 shows the tensile test results of the Repro 1075, and to verify the results, tests were performed 5 times. According to Figure 3.10, the averaged Young's modulus of Repro 1075 was 1649 $\pm$ 90 MPa and the measured ultimate tensile strength was 37.5 $\pm$ 1.8 MPa.

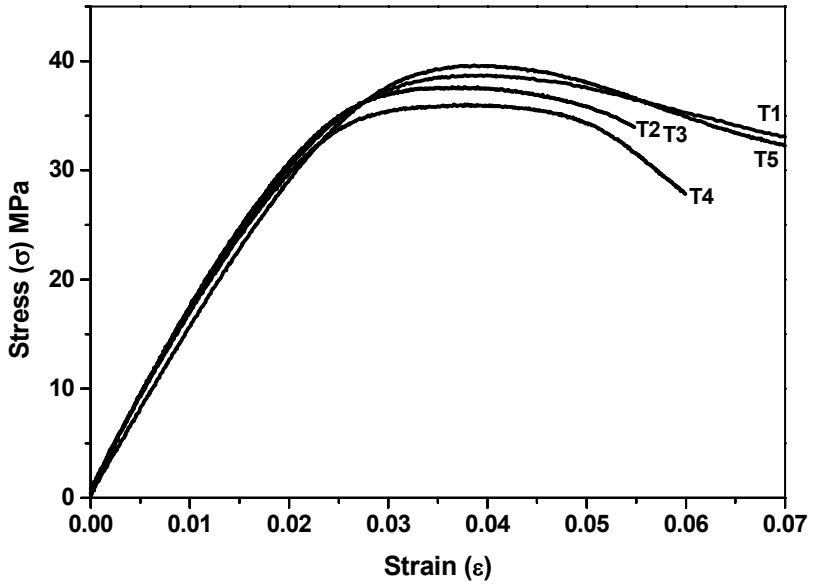

Figure 3.10. Tensile test results of Repro 1075 rigid polyurethane.

To measure the Poisson's ratio, two strain gauges (Type EA-06-125TG-350) were attached to the gauge length portion. The calculated Poisson's ratio of Repro 1075 was 0.33. This value compares well with other types of rigid polymer materials.

The compression behavior was also measured because the HG machine is used mostly under the compression state. Figure 3.11 displays the compressive stress-strain curves of Repro 1075 and for comparison purpose, one tensile stress-strain curve is inserted.

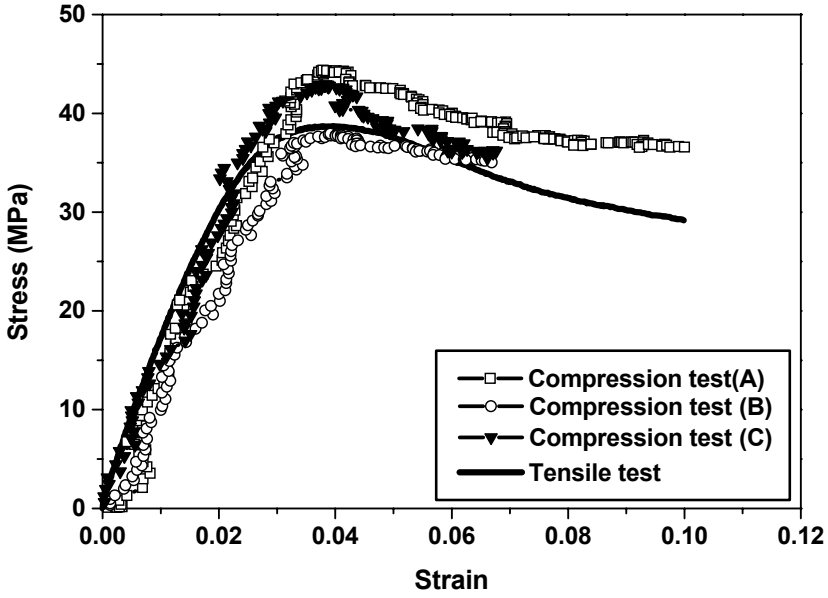

Figure 3.11. Compressive and tensile stress-strain curves of Repro 1075 rigid polyurethane.

The obtained Young's modulus in compression test is 1702 $\pm$ 113 MPa, and compared with the tensile test result, which is only ~ 3.2 % higher than tensile results. The difference of ultimate strength between tensile (37.5 $\pm$ 1.8 MPa) and compression tests (40.7 $\pm$ 2.7 MPa) was ~ 8.5 %. From these results, we suspected that the material properties of Repro 1075 are not much affected by testing methods and Table 3.1 summarizes the whole test results.

Table 3.1. Basic material properties of rigid polyurethane (Repro 1075).

Material	[1]Viscosity @ RT (cps)	[1]Gel time @ RT (min)	[2]$\sigma_{u(T)}$ (MPa)	[3]$\sigma_{u(C)}$ (MPa)	E_T (MPa)	E_C (MPa)	[2]υ
Repro 1075 (Rigid polyurethane)	**200**	**7**	**37.5 ± 1.8**	**40.7 ± 2.7**	**1649 ± 90**	**1702 ± 113**	**0.33**

[1]Mamufacturer's data sheet, [2]ASTM D638-01, [3]ASTM D695-96

3.3. Fabrication Method of HG Machine Reinforced Composite (HG-MAC)

The HG-MAC was fabricated with procedures similar to the HG machine fabrication.

Fabrication follows these steps:

- Design the mold dies with Solidworks software
- Transfer the design files to the CNC machine and making molds using green wax block
- Assemble the pre-made HG machines into the mold and then inject the resin
- Pull out the HG-MAC from the mold and cut the front and back portions of the p art and clear the inner-channel of each machine

3.3.1. Mold Design

Figure 3.12 (a) displays the dimensions of the HG-MAC mold. The HG-MAC mold is also composed of male and female molds and each single HG-MAC mold can contain 4 HG machines. The distance between machine to machine was set as 5 mm and

the height of the HG-MAC was 10 mm and this makes the volume fraction of the HG machine equal to 0.18.

Figure 3.12 (b) shows the back part of the HG-MAC mold and the hole diameter of the nozzle holder is slightly smaller than the nozzle diameter. The role of the nozzle holder is preventing the pulling out the nozzle from the mold due to the back-pressure of the injected resin. The nozzle holder was made separately and attached to the HG-MAC mold by using Epoxy glue.

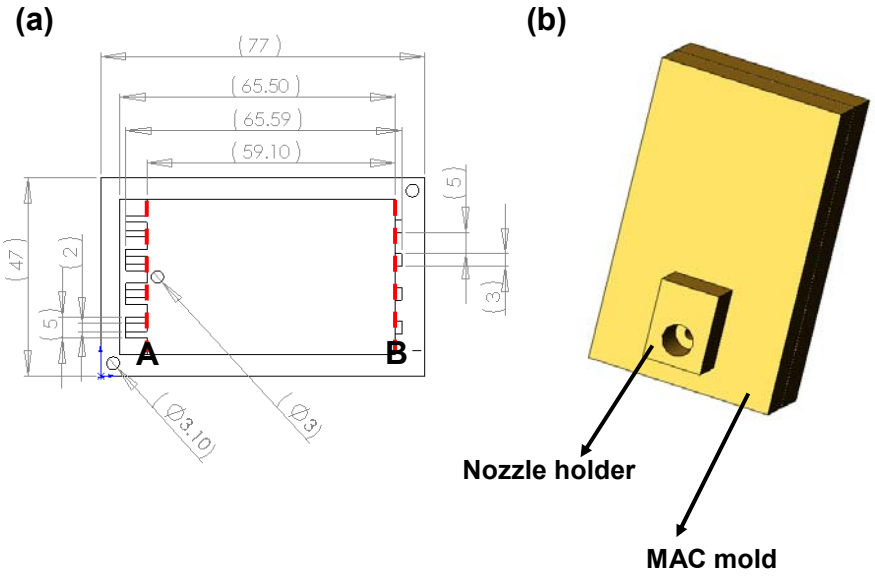

Figure 3.12. (a) Dimensions and (b) back part of the half HG-MAC mold.

A more detailed procedure of assembling the machine into the HG-MAC mold is shown in Figure 3.13. Once assembled, inject soft polyurethane (Repro 1040) resin into

the mold and cure. Before injection of Repro 1040 resin, the ends of each machine's open channel were filled to prevent possible infiltration of resin into the machines.

After the resin is injected and cured, pull the part from the mold and cut the front and back portions of the HG-MAC along with the dashed-lines A and B, which are indicated in Figure 3.12 (a) with stiff blade band saw for straight cut and then clear the inner channel of each machine with air compressor.

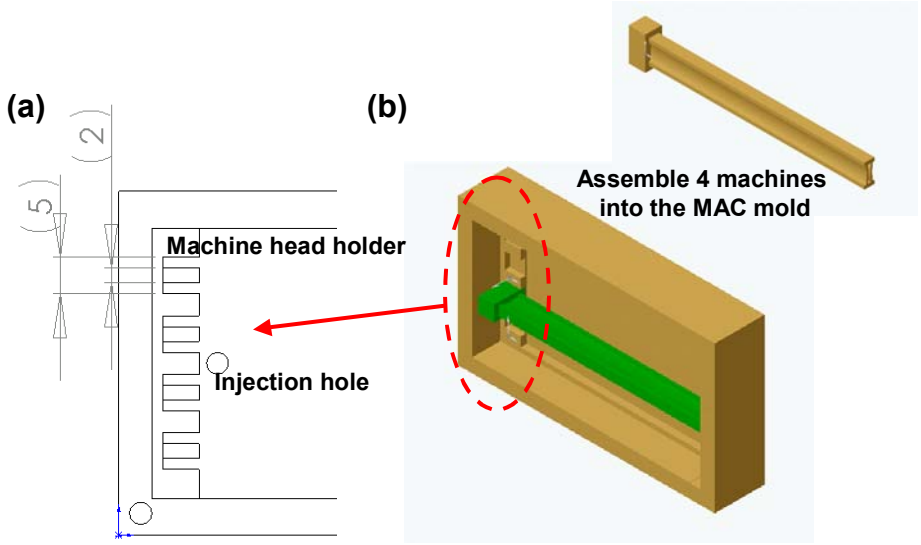

Figure 3.13. (a) Detailed view of machine holder portion (b) assembling the HG machine.

Also after some trial and errors, an adequate injection method was found to be vertical injection molding.

Figure 3.14 shows both the vertical injection molding set up as well as 4 HG machine reinforced composite shape. As shown in Figure 3.14 (b), all surfaces were flat.

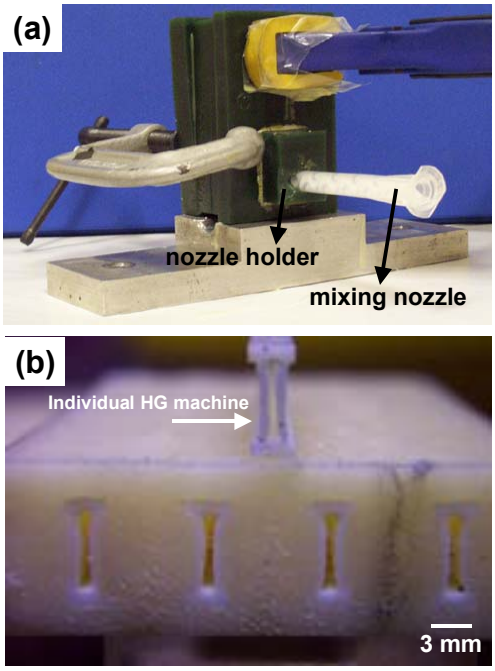

Figure 3.14. (a) Vertical injection molding set up (b) 4 HG machine reinforced composite shape.

3.3.2. Material Properties of Repro 1040 Soft Polyurethane

The compressive Young's modulus and Poisson's ratio of Repro 1040 soft polyurethane were obtained by the ASTM D695-96 static compression test. The platen speed was 0.014 mm/sec and the Poisson's ratio was calculated by the ratio of axial strain to transverse strain, which was measured by calipers.

The measured compressive Young's modulus and Poisson's ratio were ~4.24 ± 0.11 MPa and 0.49 respectively. Figure 3.15 shows the compression test curves and Table 3.2 summarizes the basic mechanical properties of Repro 1040 soft polyurethane.

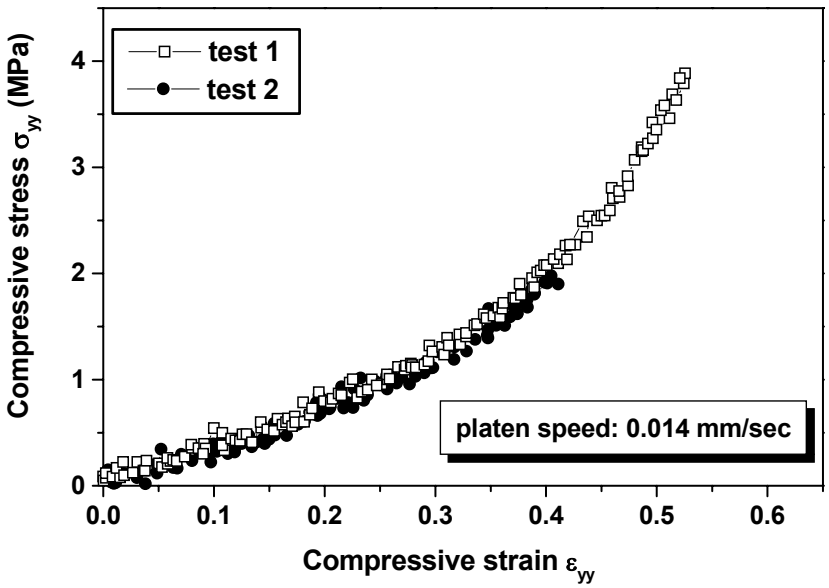

Figure 3.15. Compressive stress-strain curves of Repro 1040 soft polyurethane.

Table 3.2. Basic material properties of soft polyurethane (Repro 1040).

Material	[1]Viscosity @ RT (cps)	[1]Gel time @ RT (min)	[2]$\sigma_{u(T)}$ (MPa)	[3]$\sigma_{u(C)}$ (MPa)	E_T (MPa)	E_C (MPa)	[2]υ
Repro 1040 (Soft polyurethane)	**1350**	**28**	**8.2**	**N/A**	**N/A**	**4.24 ± 0.11**	**0.49**

[1]Manufacturer's data sheet, [2]ASTM D638-01, [3]ASTM D695-96

3.4. Static Experiments on the HG Machine

Figure 3.16 shows the cross sectional shapes of various candidate machines. All the cross sectional areas and inner-channel areas of the different machines were equal, i.e., inner-channel areas were set as 3.38 mm^2 and the remaining machine areas were 11 mm^2 to compare the true inner-channel area variations between different machines.

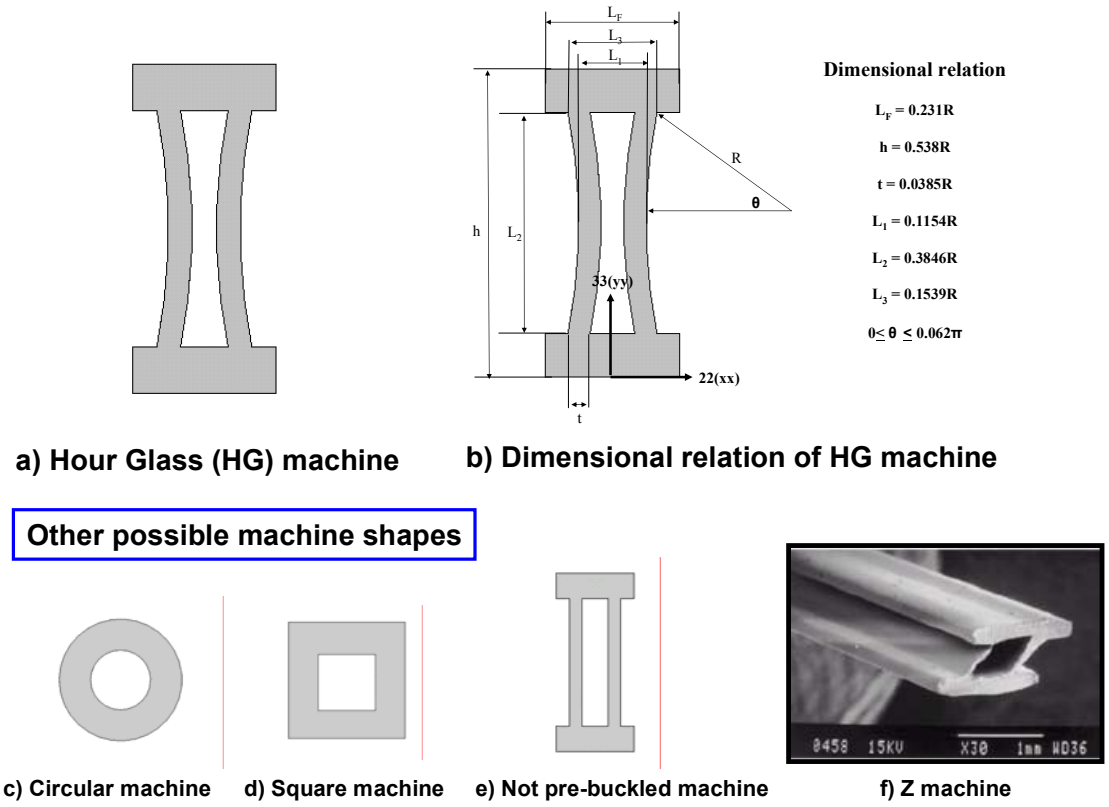

Figure 3.16. Cross sectional shapes of various candidate machines.

Since the machine augmented composite was designed for vibration absorption purpose through mechanical deformation as well as viscous damping, the most important function of the machine to squeeze out the viscous inner-channel fluid from the outer compressive loading. Because the fluid has incompressible characteristic, large area reduction should generate high pressure and cause high velocity movement of fluid and finally we can expect large amount of damping effect from this fluid movement.

To compare the inner-channel area reductions of different shaped machine, numerical analysis using Algor V14 was performed by applying the same compressive displacement (0.15 mm) to the 33 direction at the linear mode. The boundary conditions for this analysis were fixed at the bottom and at the top, every degree of freedom except Y directional degree of freedom was also fixed and detail boundary conditions analyses are described in Chapter IV.

After deformed each machine, inner-channel area changes were measured using Solidworks software. In other words, after deformed the machines, pick every inner-channel node of machines one by one and get the ΔX, ΔY, and ΔZ values of each node and draw the deformed shape with these points and after connect every point, the deformed area was automatically calculated by Solidworks software program.

The second condition must be considered is the scaled-up problem. Our model is 5 times larger than the default shape, i.e., the default wall radius (R) was 2.6 mm but that of our real model was 13 mm. To check this matter, several scaled-up specimens, i.e., 20, 30, 40 and 50 times bigger machines were fabricated and tested with compressive platen strain rate of 0.014 mm/sec. All specimens were fabricated with the geometric similarity

condition [1], which is defined as a model and prototype are geometrically similar if and only if all body dimensions in all three coordinates have the same linear-scale ratio is applied. The thickness of the specimens was same as the wall thickness, i.e., 0.0385 R to the 11 (zz) direction in every scaled-up case to apply plain strain condition; cut small portion from the infinitely long structure and not to violate the geometric similarity condition.

To make these scaled-up specimens, the open mold was cut from the green wax using CNC machine and these molds are shown in Figure 3.17.

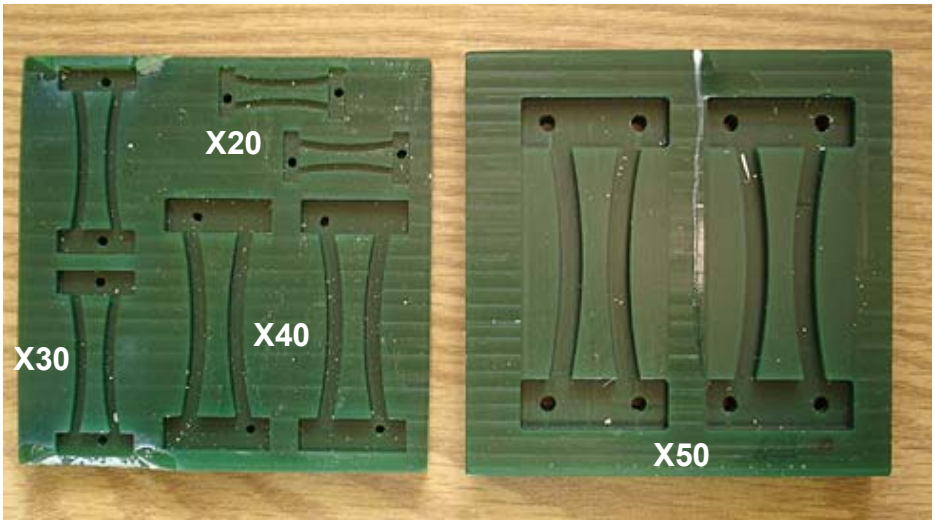

Figure 3.17. Scaled-up specimen open molds.

After cut the mold, pour Repro 1075 resin into the mold and make surface flat by using razor blade. And then remove the cured parts from the molds and glue them in the aluminum plate with epoxy glue. Figure 3.18 exhibits the glued scaled-up specimens.

Figure 3.18. X20, X30, X40, and X50 scaled-up HG machines.

Also to measure the horizontal movement of the HG machine's wall, another compression test was performed using X50 scaled up specimen with platen speed of 0.014 mm/sec and the test set up is shown in Figure 3.19.

From this experiment, we could measure the horizontal and vertical displacements of the HG machine simultaneously and finally Poisson's ratio of the HG machine could be estimated.

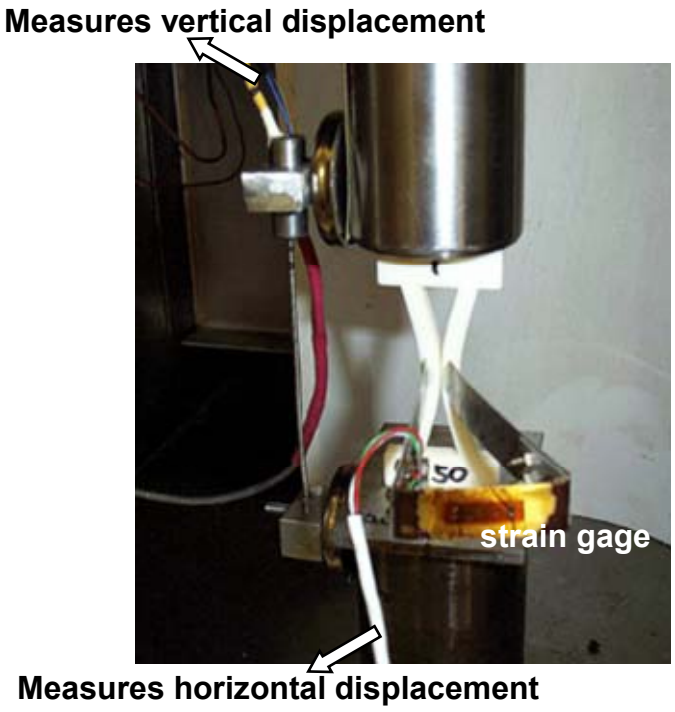

Figure 3.19. Test set up for measuring Poisson's ratio of the HG machine (using X50 scaled up machine).

3.5. Static Experiments on the HG-MAC

The main purpose of the compressive static test on the HG-MAC and matrix (no machine inside) is to set the amplitude of the cyclic dynamic testing. The compressive load was applied at the platen speed of 0.014 mm/sec until all four HG machine's side walls touched each other.

In all testing cases, no lubricant was used both on top and bottom to simulate the sandwich panel as shown in Figure 3.1. This approximates a fixed boundary condition at the bottom and allows only Y directional degree of freedom at the top.

Although dynamic properties of circular, square, and not pre-buckled machine augmented composites, which were fabricated in the same way of the HG-MAC were not measured, same static compression tests were performed on these composites to compare the compressive stress and strain behaviors.

3.6. Dynamic Experiments on the HG-MAC

To measure the dynamic properties of the HG-MAC, load-controlled dynamic testing was performed in the frequency range of 0.1 - 100 Hz at room temperature and the schematic drawing of cyclic test set up is shown in Figure 3.20 (a).

To explore the viscous fluid effect on the HG-MAC, the HG-MAC was submerged into a fluid pool when tested. To do this, the square plexiglass container with precisely surfaced 316 Stainless Steel bottom plate was used and the machine channels were pre-filled with air, 0.83, 9.5, 985 and 4730 cps fluids by vacuum technique like Figure 3.20 (b) and Figure 3.20 (c) displays the detail real experimental set up.

Before running the dynamic testing, rubber was tested first at the frequency range of 0.1 to 100 Hz to verify the correctness of the testing parameter such as amplitude, which was obtained from the static testing. Also in all testing cases, apply same small amount of pre-load to the specimen to hold the specimen in position. The testing data were recorded after several cycles to get the stable response.

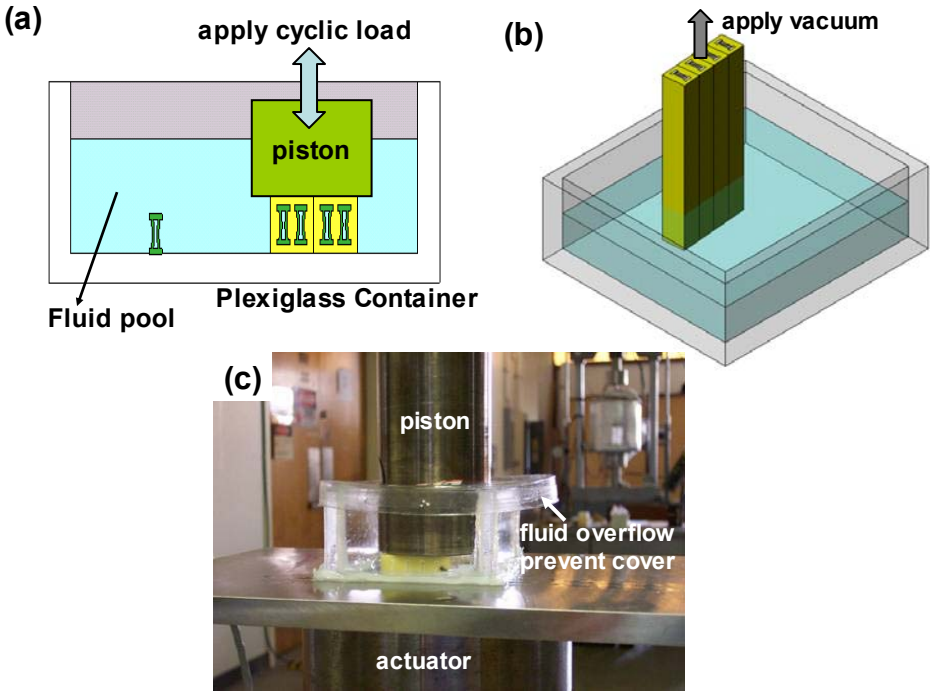

Figure 3.20. (a) Schematic drawing of dynamic testing set up (b) vacuum technique to insert fluid into the HG-MAC (c) real dynamic testing set up.

To check the heat rise during cyclic tests, the temperature of the neat matrix and air-filled, water-filled, and 4730 cps fluid-filled HG-MAC was measured as a function of frequency. Temperature was measured with a fine, 0.2 mm diameter thermocouple. The matrix temperature was measured ~ 3.5 mm down from the top surface of the 10 mm thick specimen. The thermocouple tip was placed in the center of the 24 mm by 50 mm face of the specimen. The HG-MAC temperature was measured by inserting the thermocouple into one of the HG machine so that the tip of the sensor touched the inner wall of the machine. In all cases, initial temperature was recorded first and then the temperature rise was measured ~ 1 minute after for each frequency testing. (20 to 25

seconds waiting for input load stabilization and ~ 40 seconds waiting for temperature stabilization).

Also in order to confirm the flow of silicon, air bubbles were introduced by a syringe just before starting the cyclic tests at each frequency.

Finally to check the possibility that immersion of the matrix and HG-MAC samples contributed to damping by a displacement driven diffusion of the surrounding fluid into the elastomer. Static soak test was performed so that the susceptibility of the elastomer to each fluid could be quantified.

3.7. Summary

The HG machine and HG machine augmented composite structure (HG-MAC) were successfully fabricated by and room temperature injection molding. All fabricated specimens had 5 times scaled up dimensions to the default dimensions.

The materials for HG machine and matrix of HG-MAC were rigid polyurethane (Repro 1075) and soft polyurethane (Repro 1040) respectively. The mechanical properties of Repro 1075 were similar to those of nylon 6 and Repro 1075 resin system shows almost no differences in tension and compression behaviors and the Repro 1040 shows rubber like characteristics.

To verify the scaled-up issue, X20, X30, X40, and X50 times bigger HG machine was fabricated based on the geometric similarity condition and tested statically. The thickness of each specimen was same as the wall thickness of each scaled-up specimen to assume the plain strain condition.

The HG-MAC and other shaped machine augmented composite were also tested statically to get the amplitude of dynamic testing and to compare the stress-strain behavior differences.

The dynamic testing was performed on the HG-MAC in the frequency range of 0.1 to 100 Hz at room temperature. To measure the viscous damping effect, dynamic tests were performed with the fluid-filled HG-MAC. The inner-channel of the HG machines were filled with various viscous fluids such as air, 0.83, 9.5, 985 and 4730 cps fluids by vacuum technique.

CHAPTER IV

ANALYSIS OF HG-MAC SYSTEM

The experimental results presented in Chapter IV showed that no fluid in the viscosity range tested could improve the damping of the composites. This result shows that detailed analysis of the HG-MAC is necessary to determine whether the experiments contradict our assumption that fluid/solid interaction will be an important constituent of damping or that the design used in the experiments was too far from an optimum to show good performance. We begin this chapter with finite element analysis (FEA) of four HG machine embedded MAC structure.

4.1. HG machine

4.1.1. Inner-channel Area Variation

Figure 4.1 shows the statically deformed shape of various candidates machine elements, which are shown in Figure 3.16 by FEM analysis. To squeeze out the inner channel fluid effectively - in other words, to maximize the viscous damping effect through viscous fluid flow- the inner-channel area of the machine should be reduced greatly when loaded. Only the HG machine shows the desired function due to its flexible structure deformability.

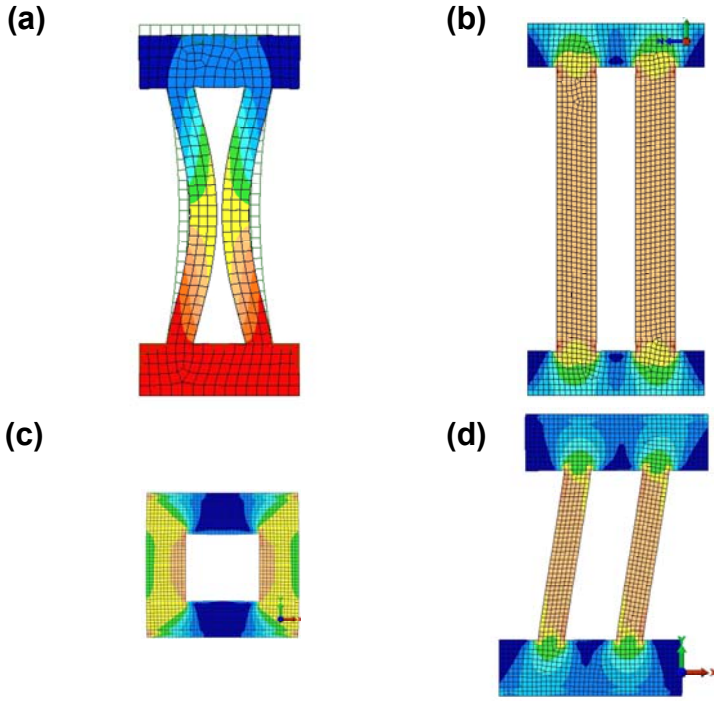

Figure 4.1. Deformed machine shape of (a) HG machine (b) not pre-buckled machine (c) square machine (d) Z-machine.

The other machines, which have the same cross sectional area as the HG machine do not deform easily like the HG machine. For example, the walls of the square machine are too thick to deform laterally. These walls would not bend much both inward and outward and with this reason, the inner-channel area reduced only ~ 5.75 %. The other machines showed similar poor performance.

Through this analysis, the inner-channel area variations were determined and these results appear in Figure 4.2. The HG machine shows ~ 6 times higher area reduction than other machines.

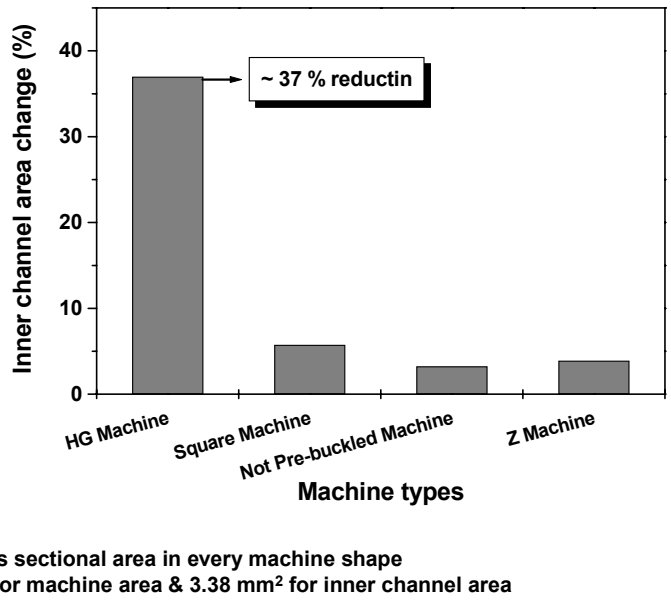

Figure 4.2. Comparison of the expected inner channel area reduction between HG machine and other shape machines.

This large inner-channel area reduction is due to the pre-buckled walls of the HG machine. Namely the HG machine is structurally unstable because of its highly anisotropic nature and inverted walls, therefore only small amount of compressive displacement can cause large reduction of inner-channel area.

4.1.2. Deformation Behaviors of the HG Machine

The deformation behaviors of the HG machine were studied and compared experimentally and numerically. Since most increased damping properties of the HG-MAC are assumed to be come from the bending of the inverted walls of the HG machine (mechanical damping) as well as flow of its viscous inner-channel fluids (viscous damping), the most important parameters of the HG machine depend on the vertical i.e.,

33 (yy) directional deformation and with this reason, the 33 directional properties are of interest here.

First, the 33 directional elastic modulus of the HG machine was measured and secondly the Poisson's ratio (υ_{32}) of the machine was studied.

Figure 4.3 displays the compressive stress-strain curves of scaled-up HG-machines. The averaged $E_{33}^{\text{HG-machine}}$ value of the scaled up specimens was 352 $\pm$ 30 MPa. The variation was within ~ $\pm$ 10 %. In all cases the obtained Young's modui are similar up to ~0.6 % strain. The possible cause of differences of $E_{33}^{\text{HG-machine}}$ values as scaled down might be come from the factors such as out-of plane buckling as well as possible misalignment between piston and the specimen. In other words, since the thickness of the specimens became thinner as we scaled down from 50 to 20 (5 mm to 2 mm), the out of plane buckling mode is easy to occur and this cause decreasing the $E_{33}^{\text{HG-machine}}$ value.

From this, we can suspect that the scaled-up issue does not affect general deformation behaviors of the HG machine as long as the HG machine is long enough to the 11 (zz) direction (plain strain condition) like conventional fibers because out of plane buckling will not occur.

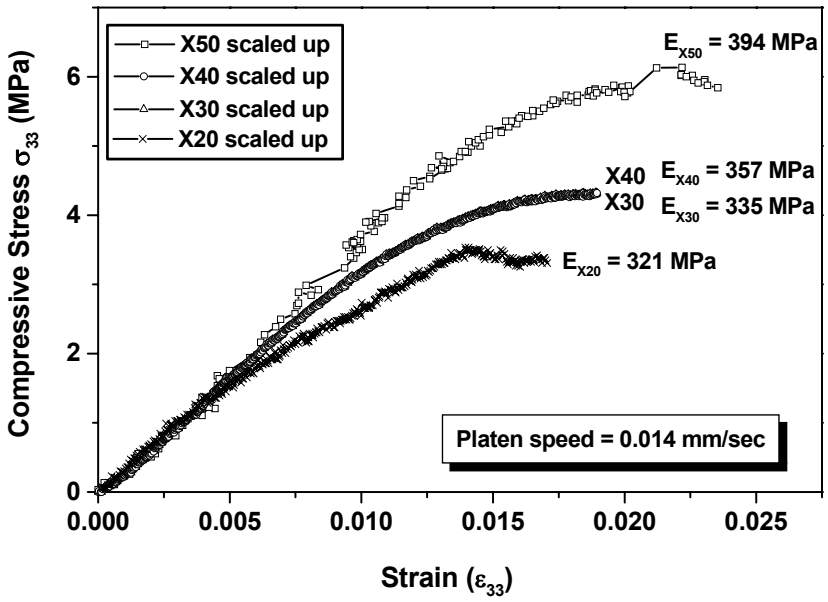

Figure 4.3. Compressive stress-strain curves of the scaled-up HG machines.

To compare the experimental results with those of numerical approach, same scaled-up specimens were generated and analyzed using FEM. Several boundary conditions were explored first to find out the same boundary conditions as the experimental case. Since we assume the plain strain condition, the $\pm$ 11 directional movements (ε_{11}) should be zero, but in real experiment, no proper constraint was applied to the 11 direction.

Table 4.1 summarizes these boundary conditions and Figure 4.4 exhibits the resulting compressive stress-strain curves using 50 times bigger dimension machine. The scaled-up issue did not make any differences in FEM analysis as long as the scaled-up dimension was based on the geometric similarity condition.

Table 4.1. Various boundary conditions for FEM analysis.

	Boundary conditions
BC 1	**Fixed bottom, Free top**
BC 2	**Fixed bottom, Free top, Z symmetry on both walls**
BC 3	**Fixed bottom, Z symmetry on both walls, X symmetry on one side of the top flanges**
BC 4	**Fixed bottom, Z symmetry on both walls, X symmetry on each side of the top flanges**
BC 5	**Fixed bottom, X and Z nodal constraint on the top flange**
BC 6	**Fixed bottom, Z displacement fixed at the top flange**
BC 7	**Fixed bottom, Z displacement fixed at the top flange (sampling rate = 40)**

In BC 1 case, because the top flange can move freely, the highly out of plane buckling deformation has occurred. And in BC 2, BC 6, and BC 7 cases, out of plane deformation did not occur because of the proper constraints, but at this time, the structure slides in-plane and due to this problem, desired gap closure can not be expected.

In the BC 3, BC 4, and BC 5 cases, the HG machine was deformed correctly without out of plane buckling or in-plane sliding. But since BC 3 and BC 4 constrained both two walls of the HG machine as well as one side or two sides of the upper flange, the resulting deformation behaviors would not be the same as the real testing conditions i.e., make E_{33} of the HG machine stiffer. Therefore, BC 5 corresponds to the same boundary condition as the real testing condition.

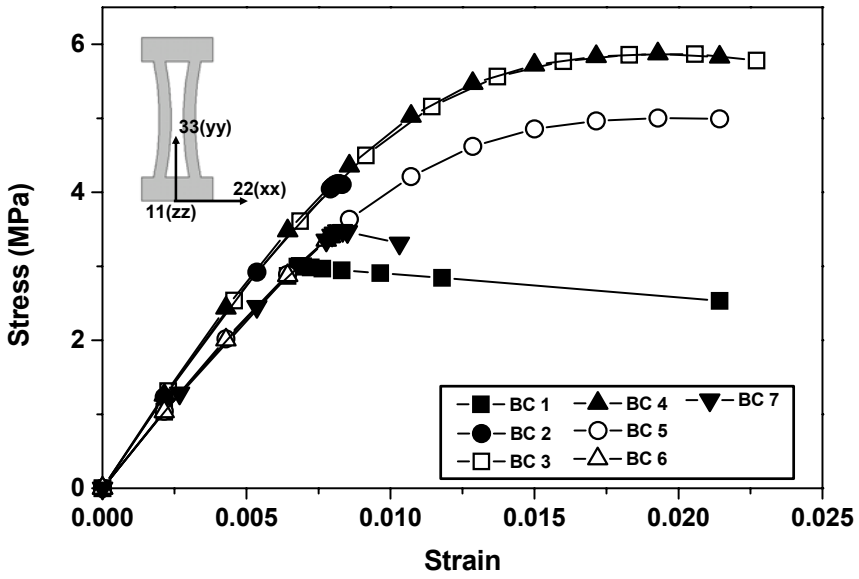

Figure 4.4. FEM compressive stress strain curves of the HG machine using various boundary conditions. BC 5 corresponds to the experimental condition.

The comparison between numerical and experimental test results is shown in Figure 4.5. The experiments were performed in the same fashion as before but at this time, to minimize the possible experimental error such as dimensional imperfection, the X40 and X50 scaled-up specimens were re-fabricated by using close mold. The difference of $E_{33}^{\text{HG-machine}}$ values between the averaged experiment (422 MPa) and numerical analysis (456 MPa) was ~ 8 %.

Still possible out of plane buckling due to the misalignment of the specimen with piston and lack of proper out of plane constraint, this difference is within in the acceptable range.

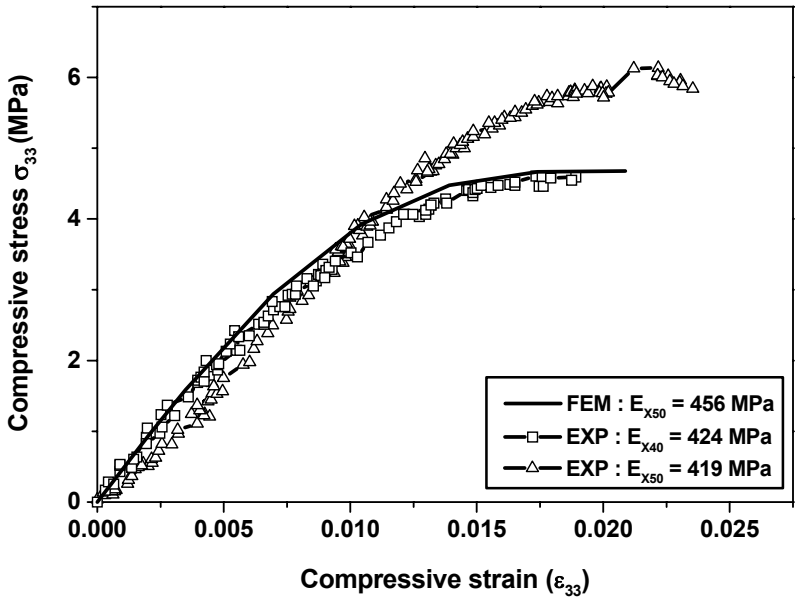

Figure 4.5. Compressive stress strain behavior comparison between numerical and experimental results.

Also since current numerical boundary condition (BC 5) is well fit to that of experimental conditions, we can expect the $E_{33}^{\text{HG-machine}}$ value of the plain strain conditioned HG machine without performing experiment by simply adding additional constraints to the $\pm$ 11 directions of the numerical HG machine model. Under this modified boundary condition, the measured $E_{33}^{\text{HG-machine}}$ value was 505 MPa.

Also the longitudinal stiffness ($E_{11}^{\text{HG-machine}}$) of the HG machine can be calculated by the conventional rule of mixture relation [11, 55, 56, 57, 58] with $E_{\text{inner-channel}} = 0$, i.e.,

$$E_{11}^{\text{machine}} = V_{inner-channel}E_{inner-channel} + V_{machine}E_{machine} = 0.76 \times 1649 = 1261 \text{ MPa} \qquad (4.1)$$

where V represent the volume fraction of the constituent

The structural Poisson's ratio ($\upsilon_{32}^{\text{HG-machine}}$) of the HG machine was also measured both numerically and experimentally. Since the inner-channel area reduction is mostly depend on this parameter, this constant value is very important on the overall function of the HG-MAC.

Figure 4.6 compares the resulting 22 directional strain variations when we apply the 33 directional compressive strains. Because of the geometry of the HG machine, the 22 directional strain is also negative. Also the horizontal movement of the middle plane of the structure is larger than the vertical movement and due to this behavior, the HG machine can have large negative Poisson's ratio. From Figure 4.6, we can calculate the Poisson's ratio of the HG machine.

Since the definition of the Poisson's ratio is the negative ratio of the laterally extension/contraction strain to axially contraction/extension strain, the negative slope values of the Figure 4.1.6 are the Poisson's ratio of the HG machine structure. The negative slope of the experimental result is -14.69 and that of FEM result is -14.35 (~ 2.4 % difference) respectively.

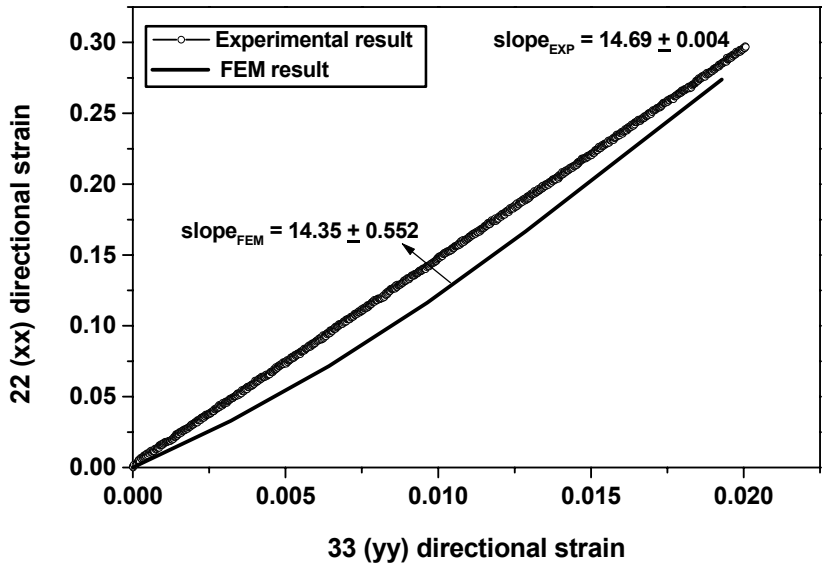

Figure 4.6. Poisson's ratio (υ_{32}) comparison between numerical and experimental tests.

4.1.3 Comparisons of HG Machine Deformation Behavior

Table 4.2 compares the experimental and numerical results of several elastic constants of the HG machine.

Table 4.2. Elastic constant values.

	Experimental approach	**Numerical approach**	**Analytical approach**	**Differences (%)**
$\mathbf{E_{11}^{HG\text{-}machine}}$			1261 MPa	
$\mathbf{E_{22}^{HG\text{-}machine}}$			< 2.45[1] MPa	
$\mathbf{E_{33}^{HG\text{-}machine}}$	422 MPa	456 (505[2]) MPa		8.1
$\boldsymbol{\upsilon_{32}^{HG\text{-}machine}}$	-14.69	-14.35		2.4

[1] using Equation 2.5.9 in chapter II, [2] under plane strain condition

4.2. HG-MAC

Figure 4.7 exhibits the static compressive stress and strain curves of the 50 mm long HG machine, 4 HG machine reinforced composite and matrix. The measured E_{33} values of machine, matrix and HG-MAC were 102.94 MPa, 6.82 MPa, and 15.78 MPa respectively. Since these E_{33} values are the transverse directional property, and moreover, the HG machine has the empty inner-channel, the stiffness of the HG-MAC in the transverse direction was not high, but compared with that of matrix value, the HG-MAC is ~131 % stiffer in this direction and when we calculate the longitudinal stiffness ($E_{11}^{HG\text{-}MAC}$) using rule of mixture equation [11, 54, 55, 56, 57], the calculated $E_{11}^{HG\text{-}MAC}$ is ~ 233 MPa.

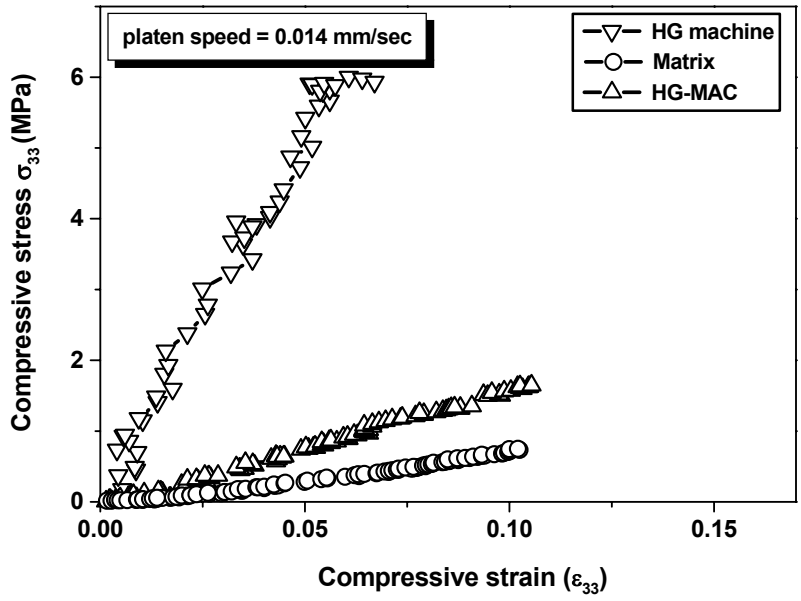

Figure 4.7. Compressive stress-strain curves of HG machine, matrix and HG-MAC in the transverse direction.

Compare with the experimental transverse directional stiffness, the HG-MAC shows almost 15 times stiffer in the longitudinal direction than transverse direction.

Figure 4.8 compares the static compressive stress and strain curves of the different machine element embedded composite structures and the II MAC represent the not-pre buckled machine augmented composite and shows the highest stiffness of them all because of its straight wall.

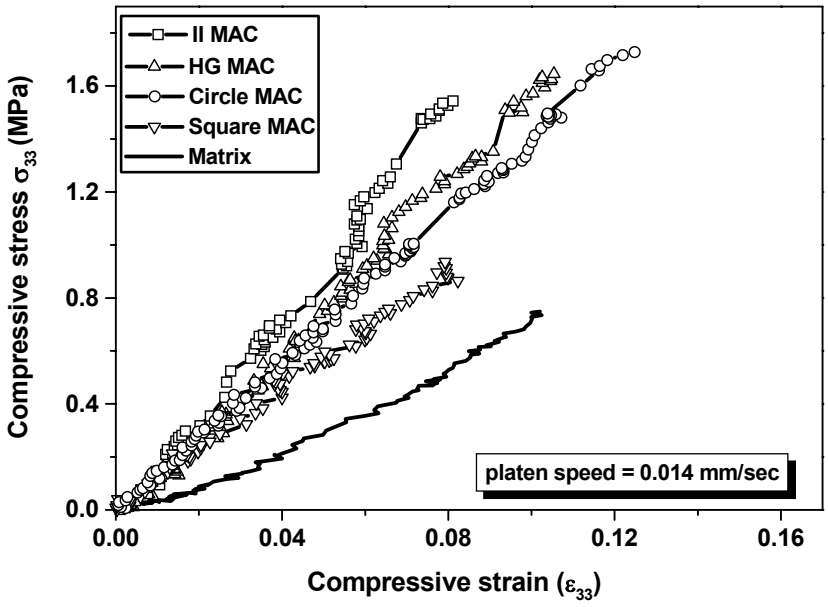

Figure 4.8. Compressive stress-strain comparison of several MACs (transverse directional property).

The reason that square and circular MAC has lower stiffness than HG-MAC is the machine height of these composite structures is much shorter than that of HG-MAC. Namely to make all cross sectional area including inner-channel area of the different shaped machine as same, the height of the machine should be adjusted and as a result,

these 2 machines have a short height but thicker wall thickness. Also form this test, we obtained the required strain (ε_{33}) for the inner-channel gap closing of the HG-MAC and this value was 0.105. But other MAC cases, this strain amount was not sufficient to close the inner-channel gap and this means, the HG-MAC is more efficient than any other candidate machine augmented composite structure.

4.3. Dynamic Properties of HG-MAC

The dynamic properties of viscoelastic materials are strongly depend on environment factors such as temperature, frequency, dynamic load, and static preload etc. [17] and in this study, frequency is the only external variable and other variables were set as constant during all tests.

Damping properties of the viscoelastic materials can be determined by either measuring the phase angle (δ), which is defined as equation 2.7 in Chapter II between stress and strain sinusoids or by calculating the hysteresis loop area of the stress and strain diagram. The tan δ is proportional to the energy loss per cycle within the framework of linear viscoelasticity [43].

The damping properties of the HG-MAC and matrix were determined by using the phase angle between stress and strain curves. Namely, the tan δ values of the HG-MAC and matrix were calculated from the time difference (Δt) of the sinusoidal stress-strain curves at each frequency and Figure 4.3.1 through Figure 4.3.5 represent the sinusoidal stress-strain curves of matrix (a) and air filled HG-MAC (b) at 0.1, 1, 10, 20 and 40 Hz conditions.

Also Table 4.3 compares the properties between Repro 1040 (matrix) and various conditioned HG-MAC.

Table 4.3. Properties comparison between matrix and fluid filled HG machine reinforced MAC.

	Material	E_{33} (MPa)	Weight (g)	Volume (cm^3)	ρ (g/cm^3)
Matrix	**Soft Polyurethane (Repro 1040)**	**6.82**	**19.6**	**17.9097**	**1.094**
HG MAC	**Rigid Polyurethane (Repro 1075) reinforced Composite**	**15.78**	**19.03 (empty)** **19.43 (0.83 cps)** **19.63 (4730 cps)**	**17.7296**	**1.073** **1.096 (0.83 cps)** **1.107 (4730 cps)**

From table 4.3, the weight of the HG MAC increase as the inner channels of the HG machine were filled with viscous fluid. Also we know that the HG MAC has most advantage in density when the inner channel was empty but still has advantage even the inner channel is filled with highest viscosity fluid. (only ~ 1.2% higher weight)

Figure 4.9 through Figure 4.13 exhibit the input stress and output strain curves at each frequency of the matrix (a) and the HG-MAC (b), which is filled with air. From these stress and strain curves, the tan δ can be calculated.

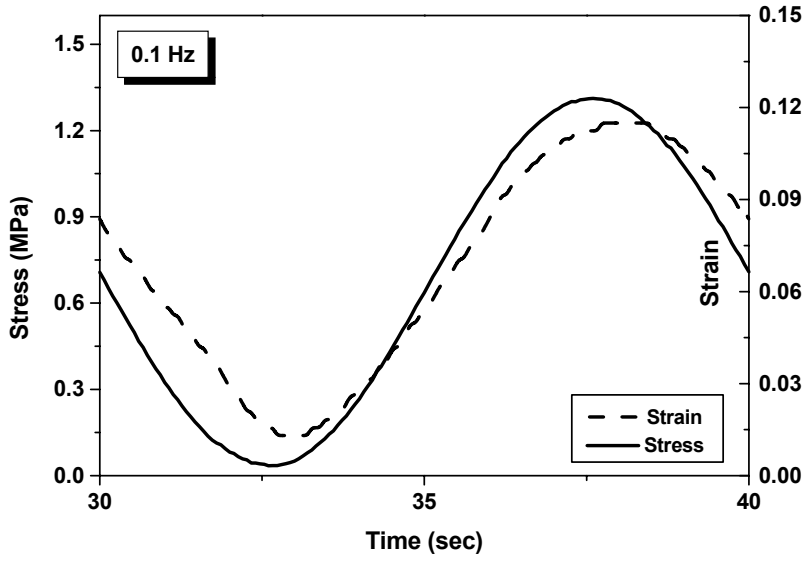

(a)

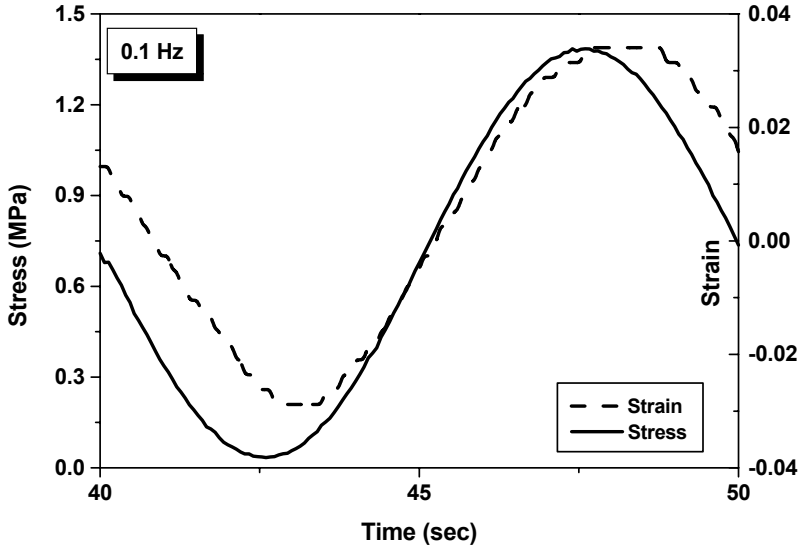

(b)

Figure 4.9. Sinusoidal stress-strain curves of (a) matrix (b) HG-MAC with air at 0.1 Hz.

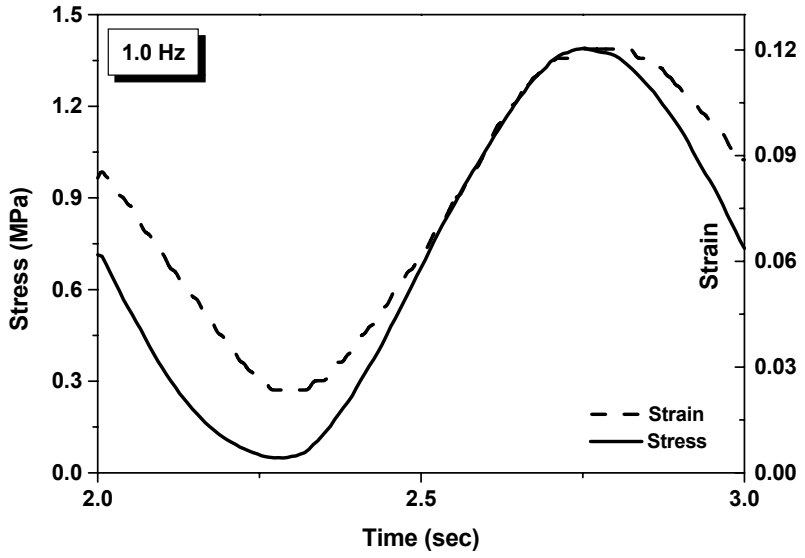

(a)

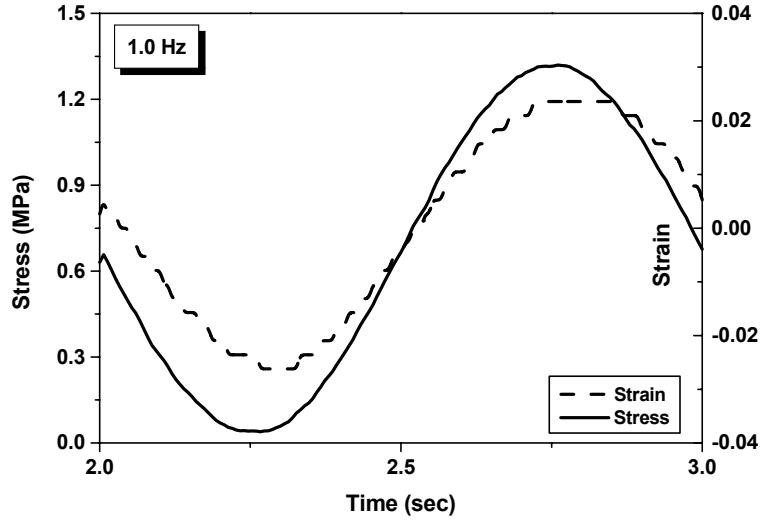

(b)

Figure 4.10. Sinusoidal stress-strain curves of (a) matrix (b) HG-MAC with air at 1.0 Hz.

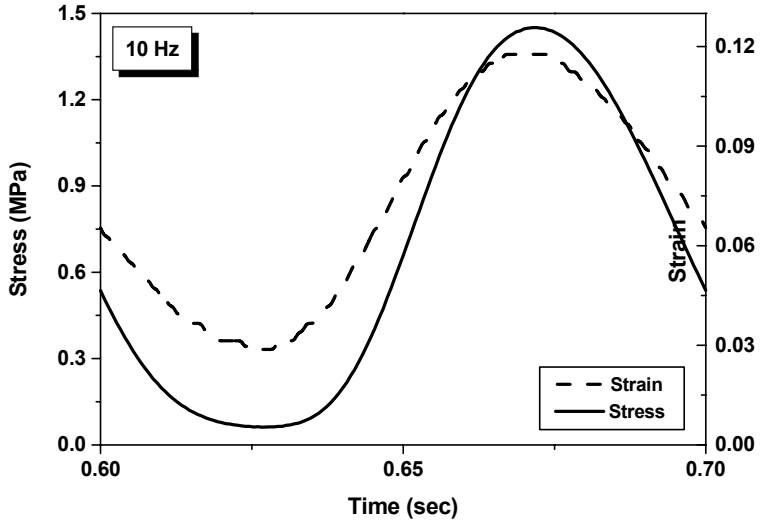

(a)

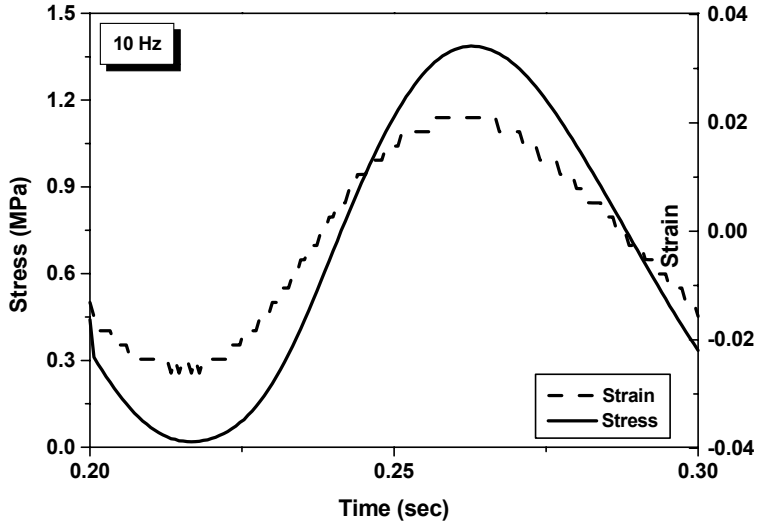

(b)

Figure 4.11. Sinusoidal stress-strain curves of (a) matrix (b) HG-MAC with air at 10 Hz.

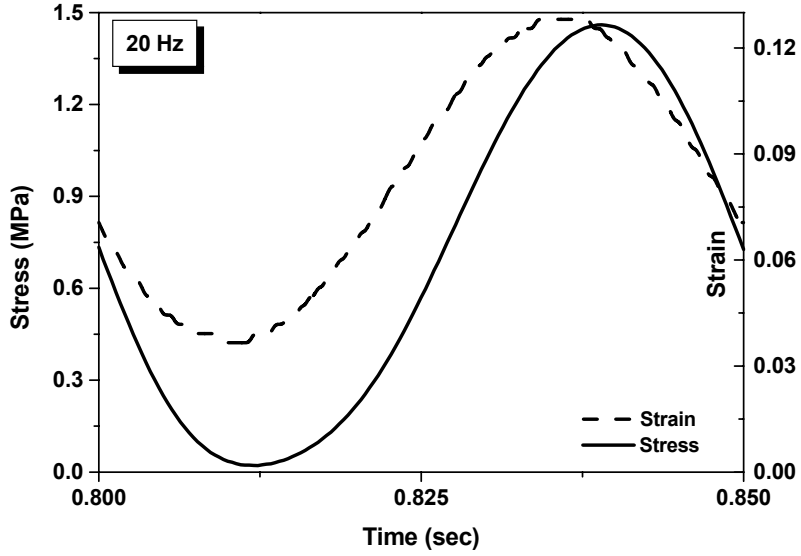

(a)

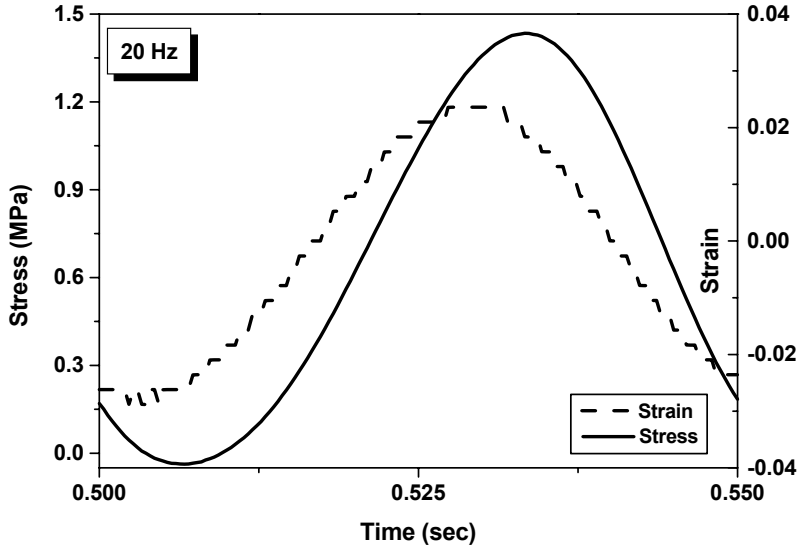

(b)

Figure 4.12. Sinusoidal stress-strain curves of (a) matrix (b) HG-MAC with air at 20 Hz.

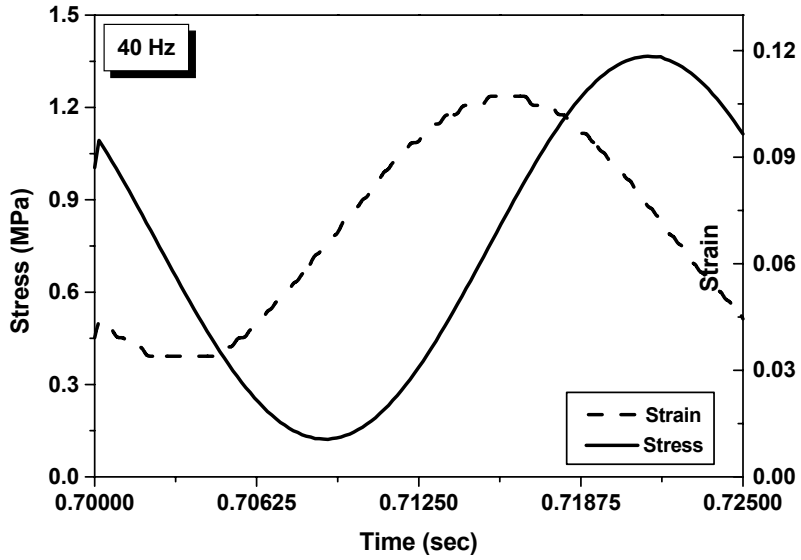

(a)

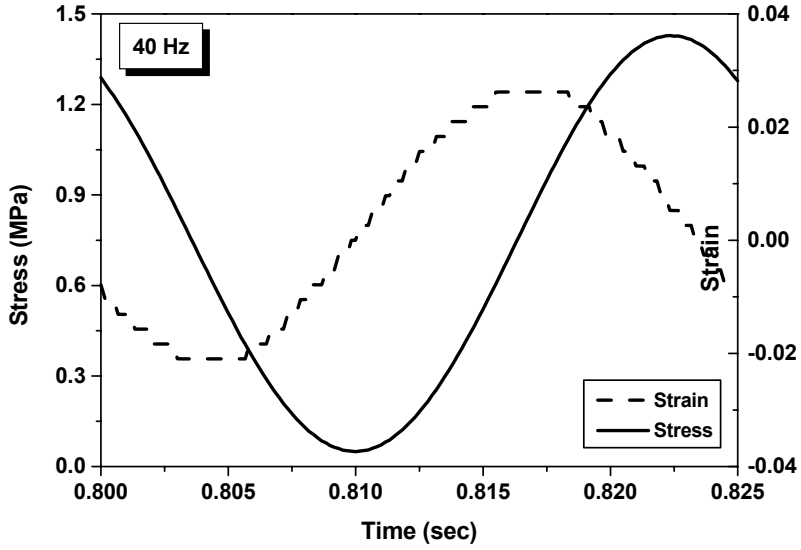

(b)

Figure 4.13. Sinusoidal stress-strain curves of (a) matrix (b) HG-MAC with air at 40 Hz.

Figure 4.14 is the summary of the dynamic test results on tan δ. From Figure 4.14 (a), the tan δ values under all different conditions are decreasing until the frequency of 10 Hz and then increase. The increment is almost linear from 10 ~ 80 Hz and after 80 Hz, the increase becomes less.

In general the most important effect of frequency on the damping properties is that modulus always increases with increasing frequency. Tan δ increases with increasing frequency in the rubbery region, takes on its maximum value in the transition region, and then decreases with increasing frequency in the glassy region [17]. This trend is also reported in the glass-epoxy composite system i.e., the measured and predicted loss moduli of the composites all increased with increasing frequency range from static to 500 Hz [59].

Figure 4.14 (a) shows that the calculated tan δ value of the HG-MAC is similar to that of matrix in the whole range but Figure 4.14 (b) shows the normalized tan δ with respect to the matrix of any conditioned HG-MAC shows large improvement in the frequency range of 1 ~ 40 Hz, but with complicated changes. In other words, when the HG-MAC was filled with 0.83 and 9.5 cps fluid, the measured tan δ value of the HG-MAC shows maximum 74 % and 75 % increase respectively with a peak at 1 Hz and in the cases of filled fluid viscosity varies from air, 985, and 4730 cps, the calculated tan δ value of the HG-MAC exhibits 89 %, 117 % and 31 % increase respectively at the frequency of 10 Hz.

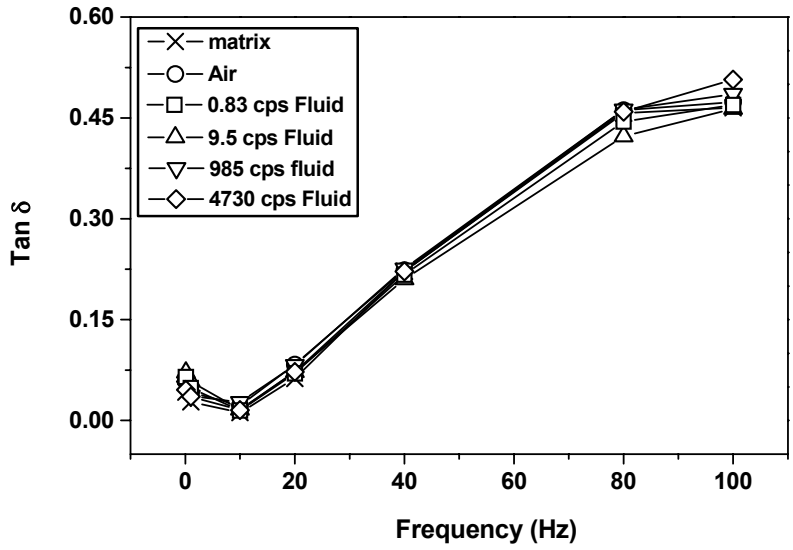

(a)

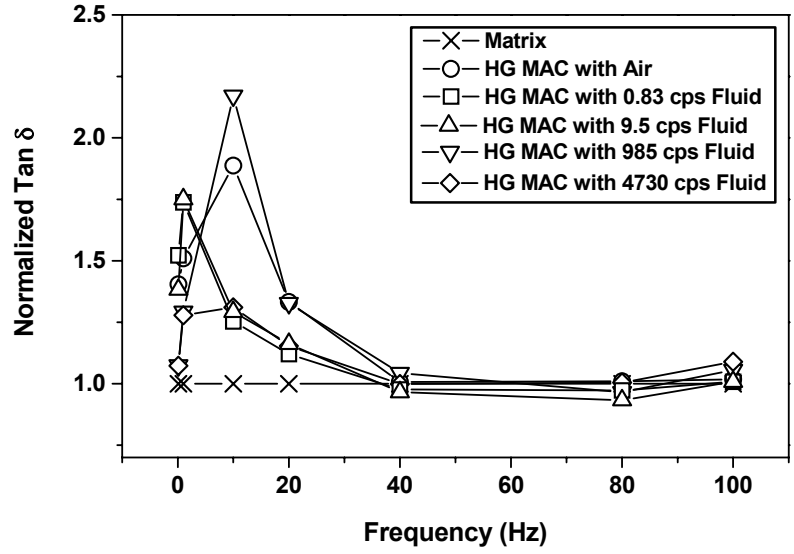

(b)

Figure 4.14. (a) Measured tan δ values under various viscosity fluids and frequency conditions (b) normalized tan δ value with respect to matrix tan δ value.

Figure 4.15 through Figure 4.19 exhibit the hysterisis loop of matrix and air-filled HG-MAC at different frequent conditions.

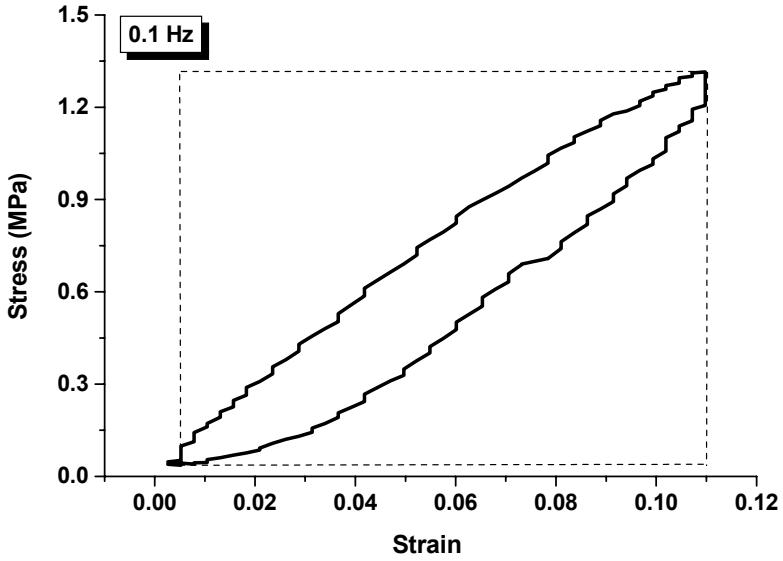

(a)

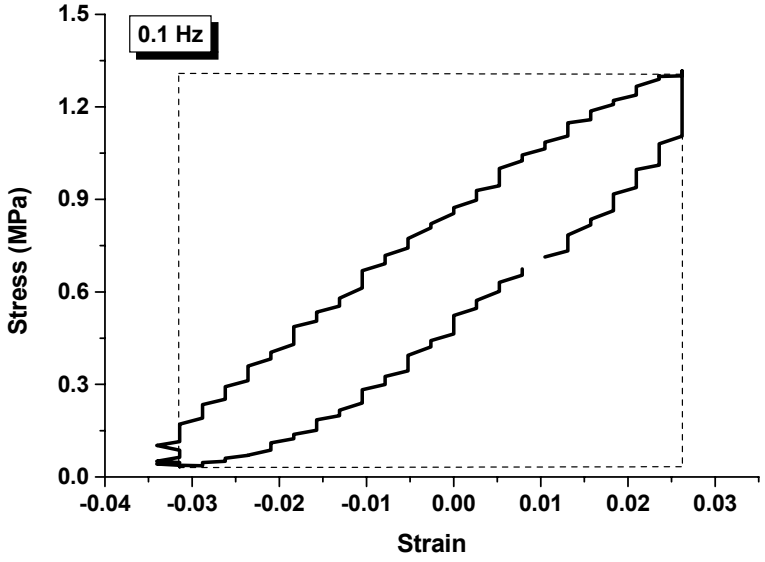

(b)

Figure 4.15. Hysterisis loop of (a) matrix and (b) air-filled HG-MAC at 0.1 Hz condition.

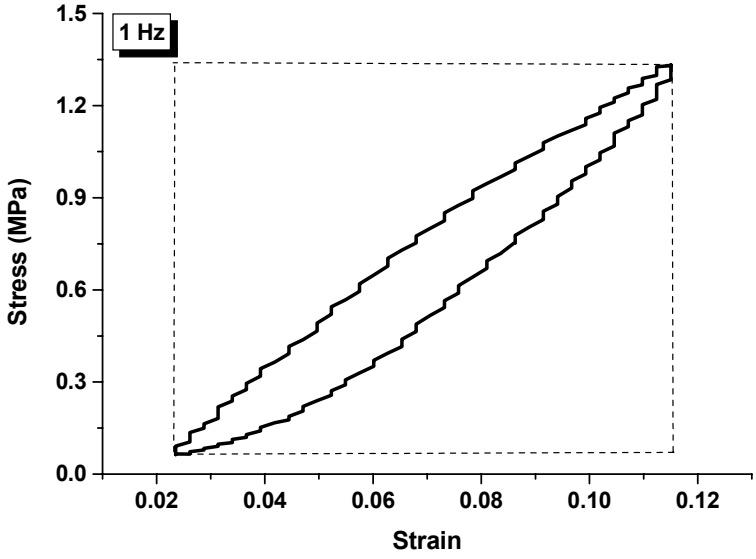

(a)

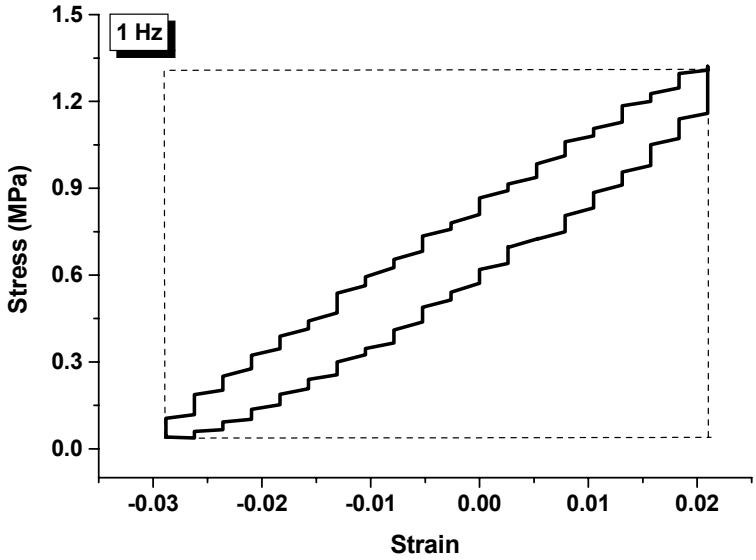

(b)

Figure 4.16. Hysterisis loop of (a) matrix and (b) air-filled HG-MAC at 1.0 Hz condition.

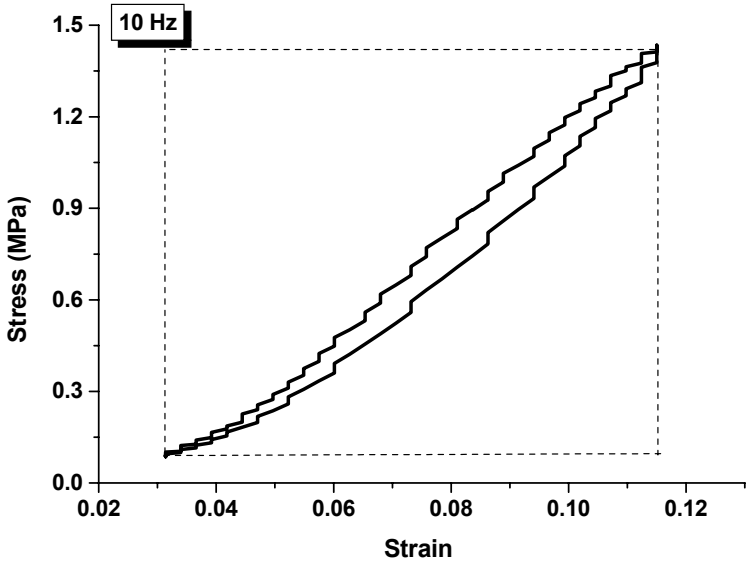

(a)

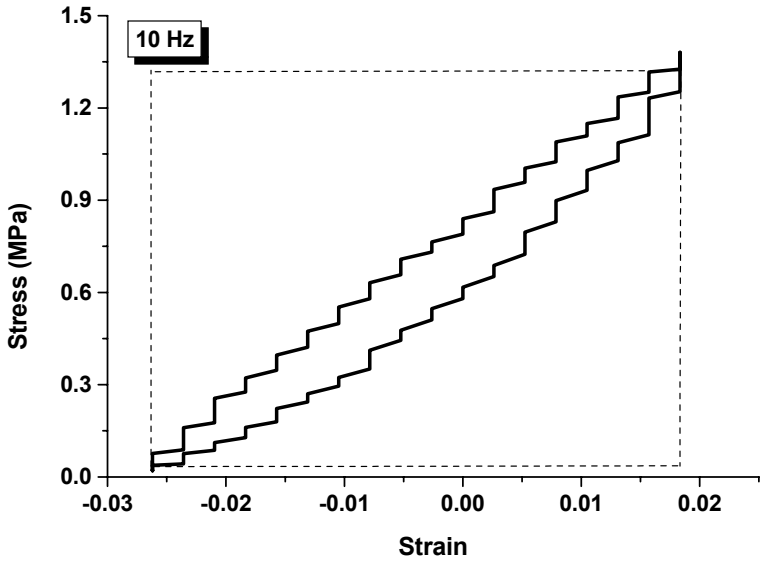

(b)

Figure 4.17. Hysterisis loop of (a) matrix and (b) air-filled HG-MAC at 10 Hz condition.

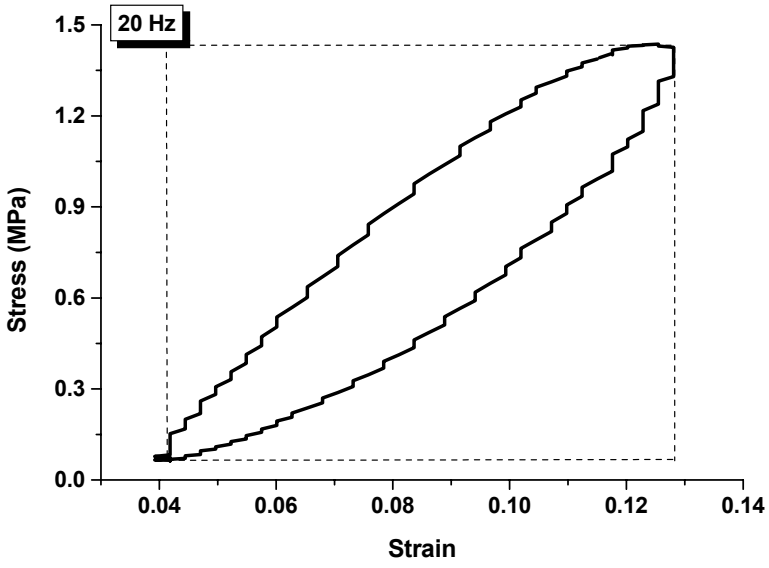

(a)

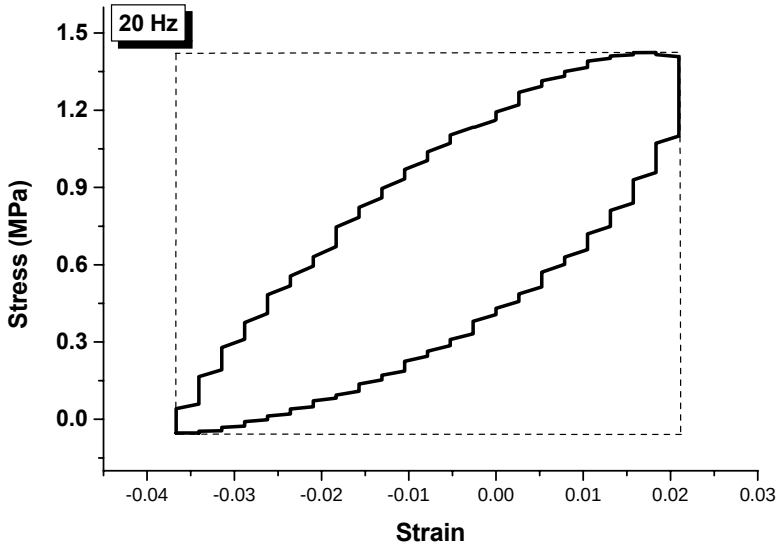

(b)

Figure 4.18. Hysterisis loop of (a) matrix and (b) air-filled HG-MAC at 20 Hz condition.

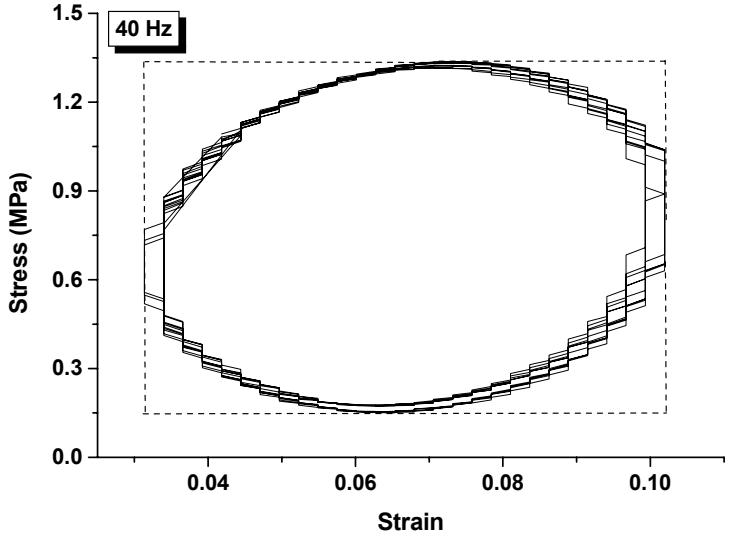

(a)

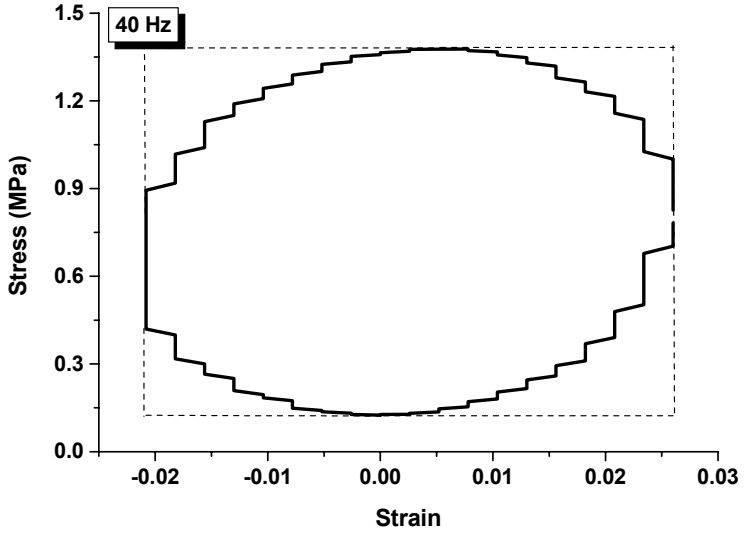

(b)

Figure 4.19. Hysterisis loop of (a) matrix and (b) air-filled HG-MAC at 40 Hz condition.

The approximate area ratio between ellipse region (energy dissipation) to rectangular region (energy input; inside the dashed line) at the frequency range of 0.1 Hz to 40 Hz of matrix and the HG-MAC is summarized in Table 4.4 and Figure 4.20. The area ratio becomes smaller as the frequency increase from 0.1 Hz to 10 Hz, but as frequency increase form 10 Hz to 40 Hz, the area ratio becomes larger and this trend is related with the tan δ value variation, which shown in Figure 4.14 (a). And in the case of the HG-MAC at 40 Hz condition, the area ratio is ~ 0.73, and this indicates that the HG-MAC can dissipate ~ 73 % input energy and the corresponding tan δ is 0.22 based on the experimental results. Also Figure 4.21 displays the relation between energy dissipation and tan δ based on the dynamic test of soft polyurethane matrix and the HG-MAC. From this chart, we can approximate the energy dissipation of the intermediate frequency condition.

Table 4.4. Comparison of energy dissipation between the matrix and the HG-MAC and corresponding tan δ value from the dynamic testing.

	Matrix		**HG-MAC**	
	Area ratio	**Tan δ**	**Area ratio**	**Tan δ**
0.1 Hz	**~0.20**	**0.04**	**~0.25**	**0.06**
1.0 Hz	**~0.15**	**0.03**	**~0.19**	**0.04**
10 Hz	**~0.10**	**0.01**	**~0.14**	**0.03**
20 Hz	**~0.30**	**0.06**	**~0.37**	**0.08**
40 Hz	**~0.72**	**0.22**	**~0.73**	**0.22**

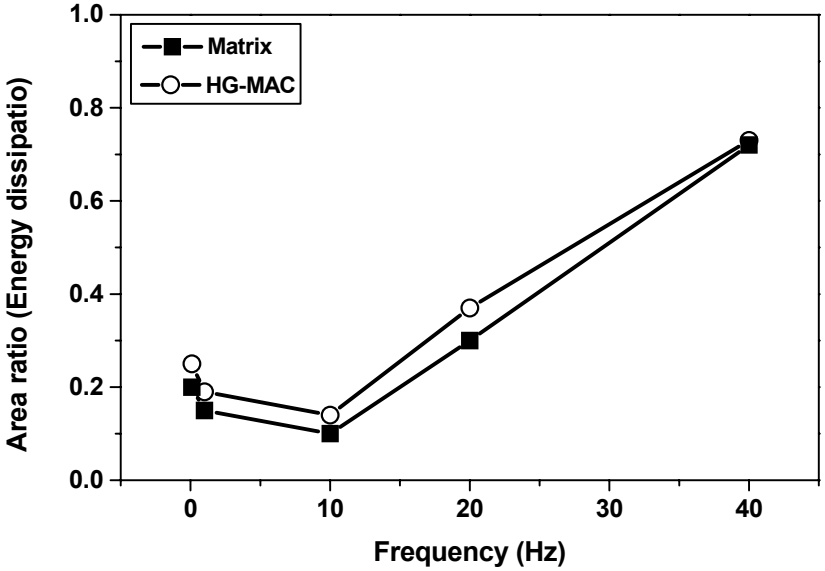

Figure 4.20. Comparison of the area ratio (% energy dissipation) between matrix and the HG-MAC as a function of frequency.

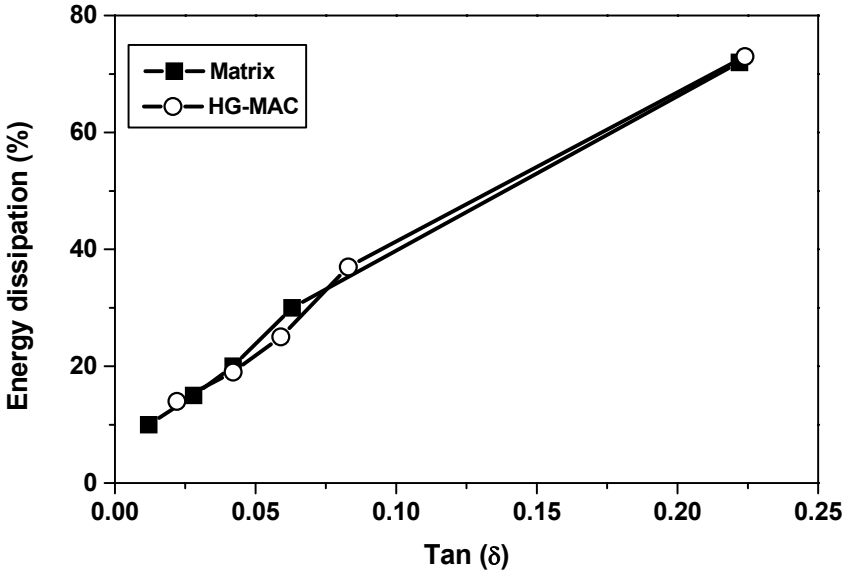

Figure 4.21. Energy dissipation and tan δ relation based on the dynamic testing of the soft polyurethane matrix and the HG-MAC in the frequency range of 0.1 Hz to 40 Hz.

However, the tan δ values of the HG-MAC between the frequency of 40 and 100 Hz regions were almost same or slightly higher than those of matrix. This is due to a dynamic testing limitation of the system employed. At frequency over 40 Hz condition, the piston can not apply desired load or displacement to fully bend the HG machine's wall and only the surface of the specimens were slightly compressed. By this reason, only similar to matrix damping properties were obtained on the HG-MAC at high frequency regions and this situation is shown by Figure 4.22.

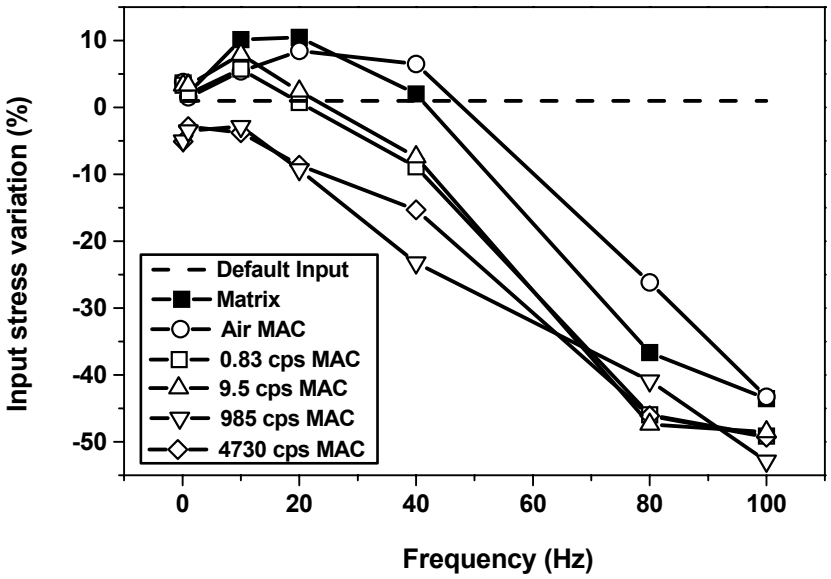

Figure 4.22. Input load variations as a function of frequency.

Because of the improved tan δ and moreover, since the storage modulus (E') of the HG-MAC is about 130 % higher than that of matrix, the calculated loss modulus (E''), which is expressed in Equation (2.7) is also increased as shown in Figure 4.23.

In Figure 4.23, only air, 0.83 and 4730 cps conditions are compared because intermediate viscosity fluid does not have much effect on the overall damping behavior of the HG MAC.

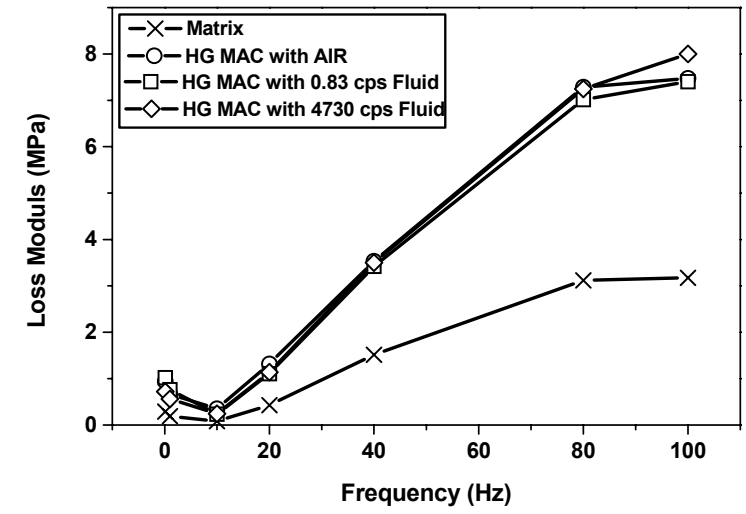

(a)

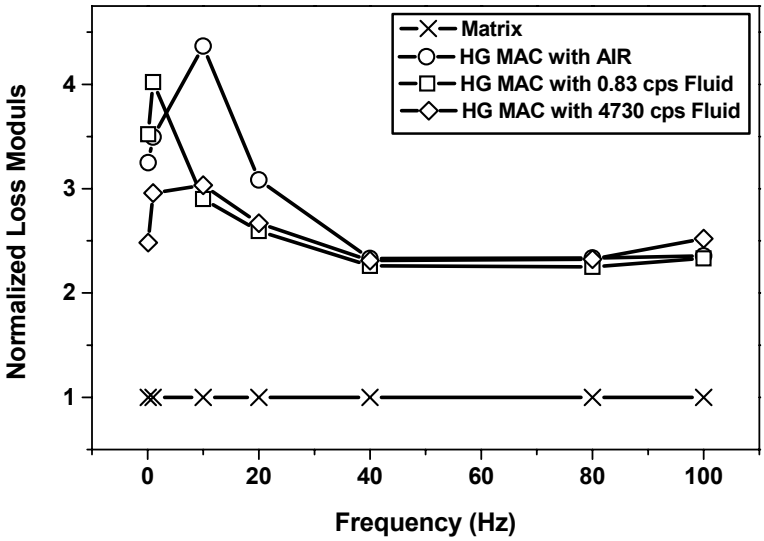

(b)

Figure 4.23. (a) Calculated loss modulus (E") values from the previously obtained tan δ (b) normalized loss modulus value with respect to that of matrix.

The possibility that immersion of the matrix and HG-MAC samples contributed to damping by a displacement driven diffusion of the surrounding fluid into the elastomer was investigated. We started with static soak test so that the susceptibility of the elastomer to each fluid could be quantified. Figure 4.24 and 4.25 exhibits the static soaking test results on the matrix at various viscosity fluid conditions. From these tests, we know that water (low viscosity fluid) can be absorbed easily into the soft polyurethane matrix. For example, the weight gains of the matrix by water absorption are ~0.45 % and ~4.3 % for 20 minutes and 24 hours exposure respectively. For the other fluids the absorption and corresponding weight gains are much smaller.

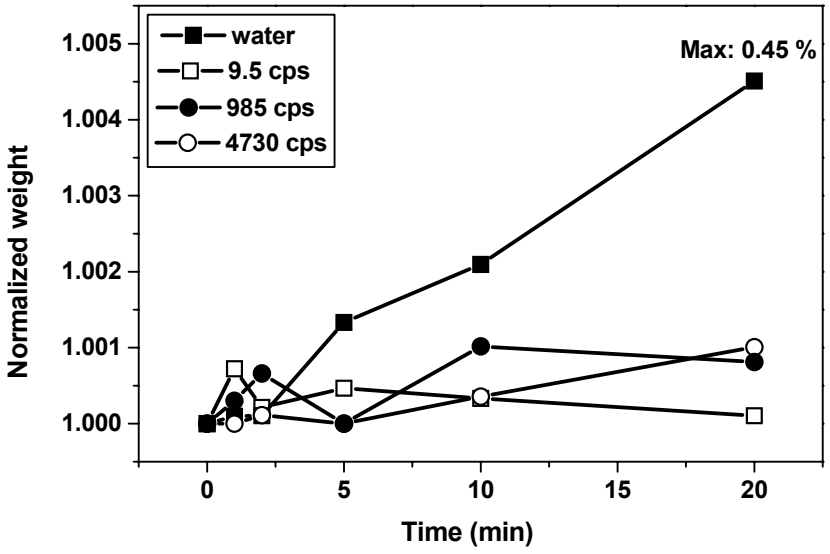

Figure 4.24. Static soak test results of matrix by using water (0.83 cps), 9.5 cps, 985 cps, and 4730 cps fluid in short time period.

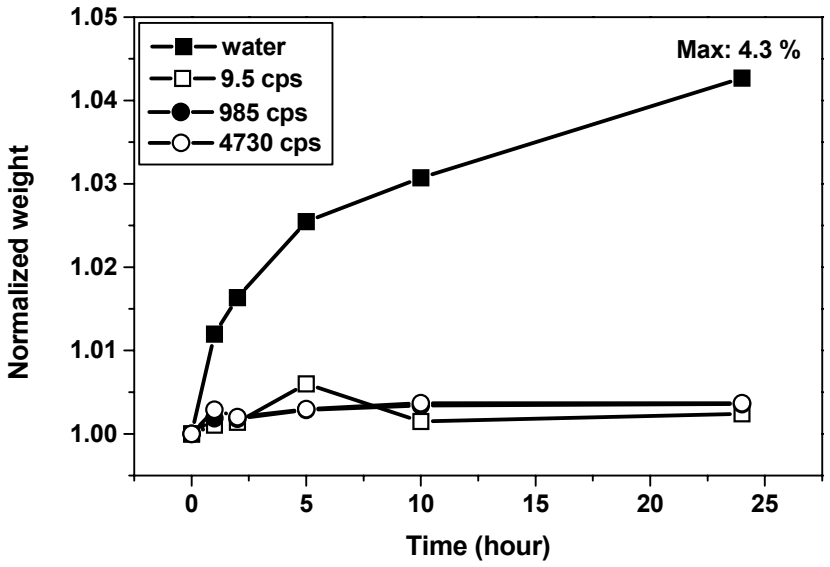

Figure 4.25. Static soak test results of matrix by using water (0.83 cps), 9.5 cps, 985 cps, and 4730 cps fluid in long time period.

Previous experiments compared the damping of the HG-MAC in fluids with the matrix sample dry. Since the matrix can take up some fluid, we repeated the matrix damping experiment with the matrix immersed in water and 9.5 cps silicone fluid. The results are shown in Figure 4.26.

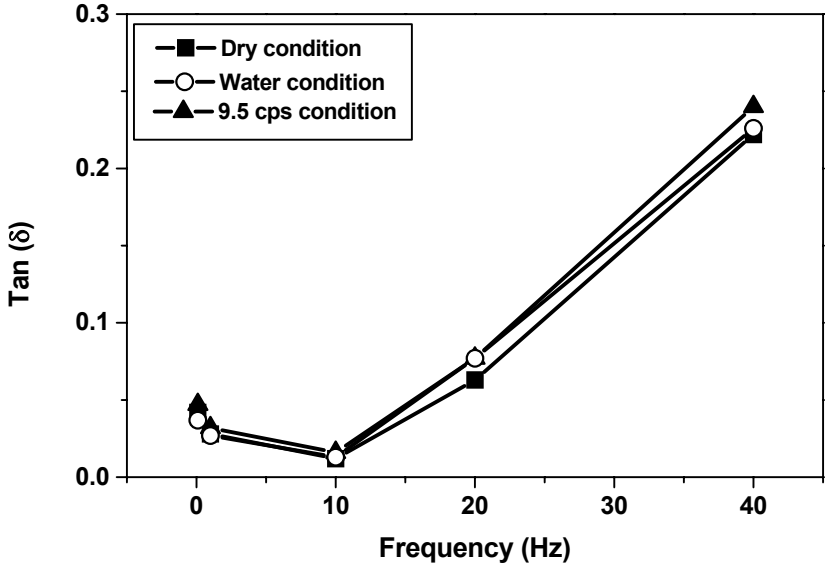

Figure 4.26. Dynamic testing results on the matrix, which is in various viscous fluids, as a function of frequency.

According to Figure 4.26, the tan δ value increased slightly when the specimen was immersed, but the amount of increase is small.

The data in Figure 4.26 allow us to make an "apples-to-apples" comparison of HG-MAC damping with the inherent damping of the matrix material. Previously all HG-MAC results were compared with the dry matrix damping at each frequency. Now we can normalized the tan δ of the HG-MAC to the tan δ of the matrix when both are immersed in same fluid. Figure 4.27 through Figure 4.29 show the normalized damping value of the HG-MAC at dry, water and 9.5 cps condition and the base line (matrix) is also constructed at the same condition as HG-MAC.

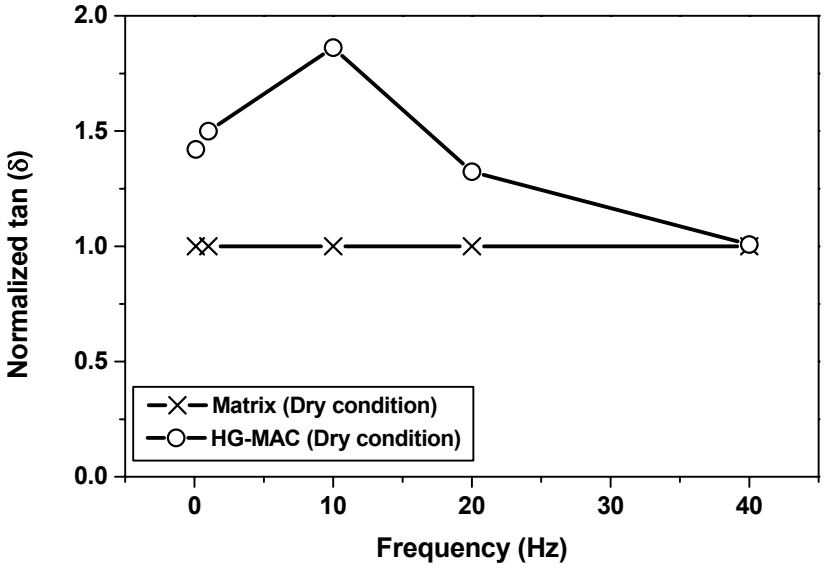

Figure 4.27. Normalized tan δ value with respect to matrix at dry condition.

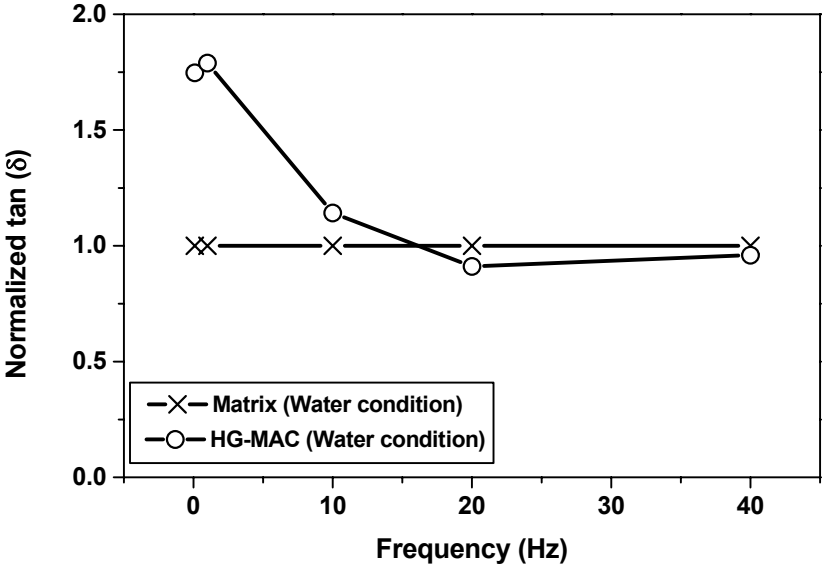

Figure 4.28. Normalized tan δ value with respect to matrix at water condition.

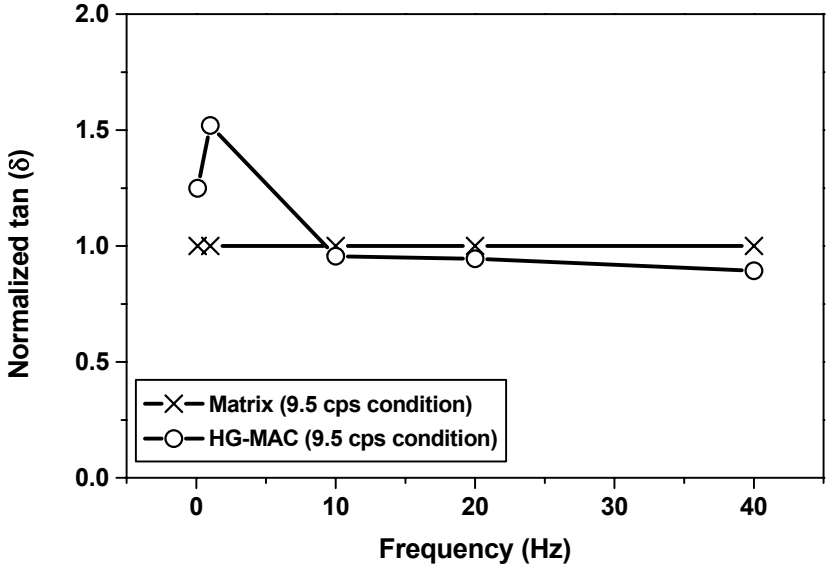

Figure 4.29. Normalized tan δ value with respect to matrix at 9.5 cps fluid condition.

In each case the damping of the HG-MAC is approximately the same or it is higher than the damping of the matrix. This occurs even though the HG-MAC material is much stiffer than the matrix alone.

The possibility of heat generation and corresponding possible damping change was also investigated and the results are displayed in Figure 4.30. Since a dissipative material or structure is cyclically deformed, the energy lost is usually released as heat and when elastomers are heated, they might dissipate energy more easily and this might account for the performance of the HG-MAC material in some conditions.

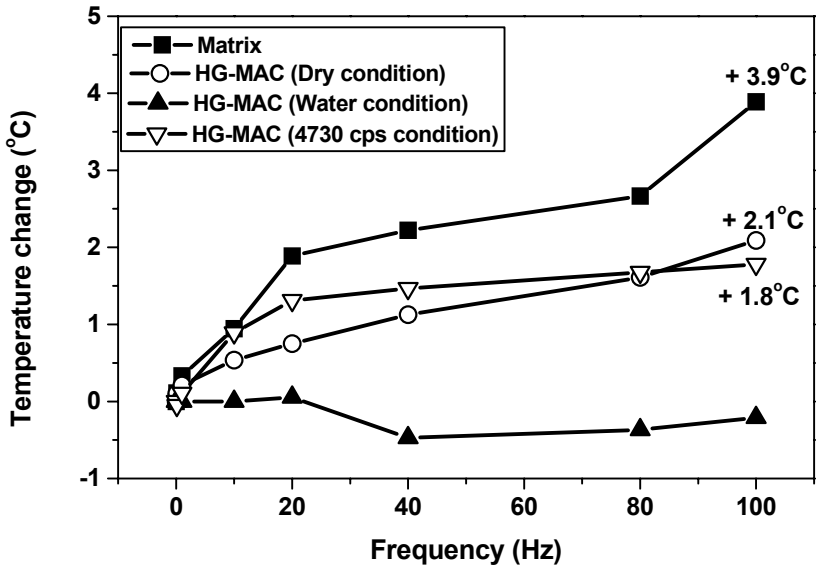

Figure 4.30. Measurement of temperature change of matrix, air-filled, water filled and 4730 cps fluid filled HG-MAC as a function of frequency.

Figure 4.30 shows that the matrix temperature rises with frequency and at 100 Hz the temperature of the specimen is ~ 4 ^{o}C higher than the initial condition. For the air and 4730 cps fluid-filled HG-MAC the temperature rise is smaller and the temperature at 100 Hz is ~ 2 ^{o}C higher than initial condition. When the channel is filled with water, the temperature is almost unchanged up to 40 Hz. Then temperature slightly decreases ~ 0.5^{o}C at 40 Hz. At 40 Hz the low viscosity water may be flowing in and out of the HG machines fast enough to cool the channels.

These experiments quantified the temperature increase as a function of frequency. Now we must determine whether this temperature rise is sufficient to account for the good damping properties measured in the material. The matrix sample reached its

highest temperature when cycled at 100 Hz, therefore we used 100 Hz to preconditioning the matrix sample to a temperature ~ 4 ^{o}C higher than its initial temperature. About 1 minute after a stable input load and temperature were reached at 100 Hz, we dropped the frequency to 40 Hz and collected the load/displacement data necessary for calculating the tan δ. The prior experiments at 40 Hz showed that tan δ is 0.22. Tan δ of the heated matrix was measured at 0.20, which is within experimental error, the same value. Therefore we conclude that the heating of the matrix is not sufficient to account for the retained damping capability of the HG-MAC material.

Also from this testing, we observed that the fluid viscosity does not significant effect on the total damping behaviors of the HG MAC. Since the HG-MAC includes open inner channels, the HG-MAC is assumed to be one of the conventional open cell foams and especially when the cells are filled with some viscous fluids, the situation is much similar to our case and we can expect viscous dissipation damping. Namely when open cell elastomeric foam is compressed, energy is absorbed in the bending and buckling of the cell walls and expulsion of the pore fluid when extended and removing the outer loading the fluid is drawn in. Through this mechanism, we can expect viscous dissipation and this mechanism is strongly dependent on strain-rate and that, unless the cells are small and the cell fluid is very viscous, it becomes important at high strain rate (10^3/s or more) [60] and the normalized energy absorption of open cell is defined as [60]

$$\frac{W}{E_S} = 0.05\left(\frac{\rho^*}{\rho_S}\right)^2\left(1-1.4\frac{\rho^*}{\rho_S}\right)+\frac{C\mu\dot{\varepsilon}}{E_S}\left(\frac{L}{l}\right)^2\ln\left(\frac{1}{1.4\rho^*/\rho_S}\right) \tag{4.2}$$

where ρ^* and ρ_s are the density of the HG MAC and density of its constituent materials respectively. E_s is the Young's modulus of the cell material, μ is the dynamic viscosity of the fluid, L is the sample dimension, *l* is the cell size and C is a constant close to unity. According to Equation 4.2, when the second term is much smaller than the first, viscous dissipation is negligible. But when the second term is comparable with, or larger than the first-higher strain-rate or higher viscosity of fluid- then this new contribution becomes important [60].

Because the HG MAC's dynamic testing condition lies between the frequency range of 0.1 ~ 100 Hz with amplitude of 2340 N, correspond to the strain-rate ($\dot{\varepsilon}$) of 0.014 ~ 8.175 /s, the strain-rate is well below to the effective strain-rate (10^3/s or more) and due to this difference we suspect that the viscous dissipation effect was minimal.

The required fluid viscosity for generating measurable viscous damping can be approximated by using conventional fluid dynamics with simple circular pipe geometry, which has the same dimension as the HG machine. The average energy dissipation at 40 Hz testing condition from the five different fluids (air, 0.83 cps, 9.5 cps, 985 cps and 4730 cps) is ~ 70 % and if we want to see the viscous fluid effect, the energy dissipation should be at least 85%. From this information and using basic fluid dynamics concept (head loss from the horizontal circular pipe) we can set the following equation:

$$\frac{(0.85-0.70)\times Energy\_input}{g_{(fluid\_moved)}} = \frac{0.15\times(Energy\_input)}{\rho V_{(fluid\_moved)}} = \frac{128\mu LQ}{\rho\pi D^4} \tag{4.3}$$

where D is the diameter of circular pipe which is converted from the hydraulic diameter of the inner-channel of the HG machine, μ is the viscosity of fluid, L is the pipe length and Q is the flow rate (m^3/sec).

Since the energy input is 51.26 x 10^{-3} (Nm) and D is 2.08 x 10^{-3} m, L is 0.05 m, and if we assume 37 % inner-channel area reduction has occurred (Maximum inner-channel area change of the HG machine by full compression is ~ 37 %) and then the volume change will be 1.25 x 10^{-9} m^3 (assume 1 mm thickness fluid) and corresponding flow rate Q at 40 Hz condition will be 100 x 10^{-9} m^3/s. With this information and using equation (2), the required fluid viscosity can be calculated. The calculated fluid viscosity for the measurable viscous damping is 88.92 Kg/m s = 889,230 cps. This value is almost 19 times higher than the most viscous fluid which we used in our real experiment. From this, we can suspect that the small viscous damping in the real experiments is due to the insufficient fluid viscosity. Also according to the flow visualization test results, when the highest viscosity fluid was used, the motion of the air bubble at the channel entrance was consistent and slow even at high frequency. This observation confirms that the silicone fluids were flowing in each experiment. However, the inefficient design of the HG machine channel could not accelerate the fluid to high velocity.

From the experimental results, the damping mechanism of the HG-MAC can be expected like Figure 4.31.

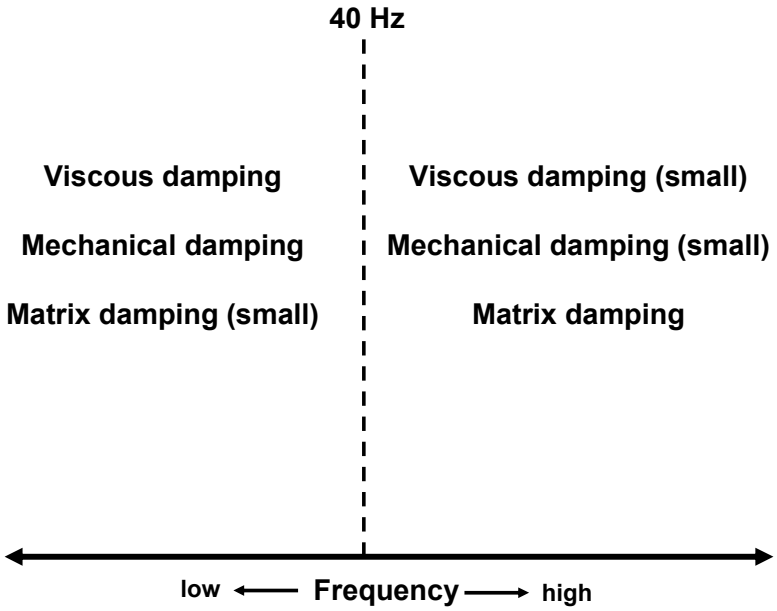

Figure 4.31. Expected frequency dependent damping mechanism of the HG-MAC based on this study.

4.4. Numerical Analysis of Unit Cell Behaviors

In numerical analysis, the performance of the HG-MAC is determined by the inner-channel gap closure amount, which is defined as the reduction of the distance between the middle points of the HG machine's wall because the approximated inner-channel area reduction of the HG machine is composed of both change in height ΔL_2 and middle line length ΔL_1 of the HG machine as shown in Figure 3.1 (a).

Since the expected damping enhancement of the HG-MAC comes from both mechanical, which depends on the geometry of the machine shape, and viscous dissipation damping, the large reduction of ΔL_1 will be good for better damping because the viscous dissipation damping by fluid flow will be proportional to the inner channel

area reduction. Also the inner-channel of each machine is assumed to be filled with air and the volume fraction of the machine includes the volume of the inner-channel area.

The lamina or laminated HG-MAC, which is displayed in Figure 3.1 (b) can be fabricated by continuously adding solitary HG-MAC (unit cell) in the horizontal or vertical direction, so the unit cell behaviors were firstly explored by varying the Poisson's ratio of the matrix, stiffness ratio between HG machine and matrix ($E_{machine}/E_{matrix}$) and volume fraction of the HG machine and these conditions are summarized in Table 4.5.

Table 4.5. Detailed input conditions for numerical analysis.

Material	**E (MPa)**	**Stiffness ratio $E_{HG\ machine}/E_{matrix}$**	**Poisson's ratio (υ)**	**Volume fraction**
HG machine	**1649 (Fixed)**		**0.33 (Fixed)**	**0.1, 0.18, 0.2, 0.24, 0.3, 0.36, 0.4**
Matrix	**1649**	**1**	**0.33, 0.40, 0.49**	**1-($V_{HG\ MACHINE}$)**
	82.45	**20**	**0.33, 0.40, 0.49**	**1-($V_{HG\ MACHINE}$)**
	32.98	**50**	**0.33, 0.40, 0.49**	**1-($V_{HG\ MACHINE}$)**
	16.49	**100**	**0.33, 0.40, 0.49**	**1-($V_{HG\ MACHINE}$)**
	8.25	**200**	**0.33, 0.40, 0.49**	**1-($V_{HG\ MACHINE}$)**
	4.12	**400**	**0.33, 0.40, 0.49**	**1-($V_{HG\ MACHINE}$)**

4.4.1. Effect of Poisson's ratio on the Matrix

The gap closure behavior changes in matrix Poisson's ratio and with $E_{machine}/E_{matrix}$ at several values with a fixed volume fraction of the HG machine ($V_{HG\ machine}$) = 0.3 shows in Figure 4.32. As shown in Figure 4.32, the highest gap closure was obtained when the Poisson's ratio of the matrix was 0.49. This is true at every stiffness ratio ranges. The same trend was observed for other volume fractional cases.

This result makes sense because as the Poisson's ratio of the matrix approaches 0.49 the lateral expansion of the matrix becomes easier due to increase in bulk modulus (K) under compression. Meanwhile an HG machine with an empty inner-channel has structural negative Poisson's ratio. The compressed matrix expands in both lateral inward and outward directions and pushes the walls of the HG machine.

Figure 4.32 shows that, when the $E_{machine}/E_{matrix}$ is 1, the gap opens rather than closes and there is no significant effect of matrix Poisson's ratio on the gap closure however as the stiffness ratio varies from 20 to 400, the gap closure amount differences between the matrix Poisson's ratio of 0.33 and 0.49 varies from ~ 50 % to ~ 113 % . Finally, there is a peak gap closure point when $E_{machine}/E_{matrix}$ is around 30. This means that maximum performance of the HG-MAC, requires an optimum $E_{machine}/E_{matrix}$ value.

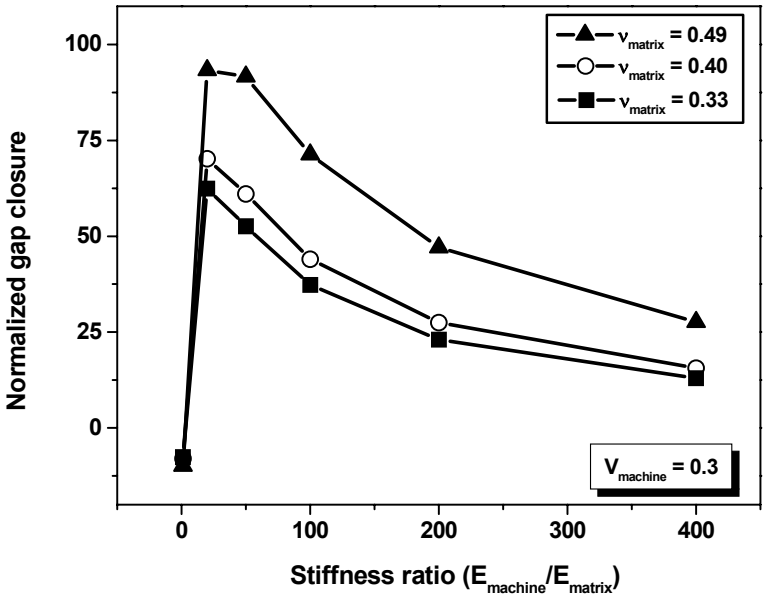

Figure 4.32. The effect of matrix Poisson's ratio on the gap closure of the unit HG-MAC with fixed machine volume fraction of 0.3.

4.4.2. Stiffness Ratio ($E_{machine}/E_{matrix}$) and Volume Fraction Effects

4.4.2.1. Impact on Performance

The effect of the $E_{machine}/E_{matrix}$ and volume fraction of the machine with fixed matrix Poisson's ratio of 0.49 on the gap closure of the unit cell appears in Figure 4.33. The volume fraction of the composite was made by the varying of the horizontal dimension of the matrix as shown in Figure 4.34.

Figure 4.33 shows that, as we increase the $E_{machine}/E_{matrix}$, the gap closure amount rises from almost 0 to 100 % and then decreases again. This happening for all volume fractional cases. Also low volume fraction of machine cause more gap closure when

$E_{machine}/E_{matrix}$ is above 100, but when $E_{machine}/E_{matrix}$ is below 100, gap closure and stiffness ratio does not follow this pattern.

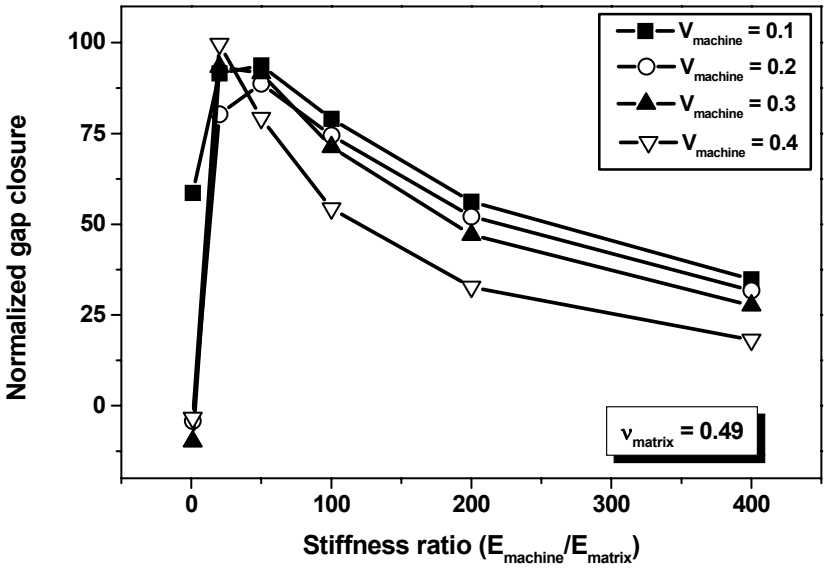

Figure 4.33. The effect of machine volume fraction on the performance of the unit HG-MAC.

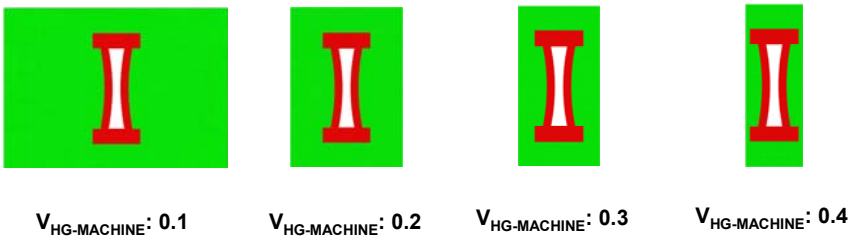

Figure 4.34. Volume fraction changes were modeled by changing the RVE width alone.

Figure 4.35 displays this gap closure over narrow range of stiffness ratios. From this chart, we observed that increasing the volume fraction of the machine cause increasing the overall gap closure except volume fraction of 0.1 and there are optimum stiffness ratios in every volume fractional case, which is marked as number in the parentheses.

If we start at a volume fraction of 0.1 (solid squares), we are in the middle of Figure 4.35 (a) and the best stiffness ratio for optimum gap closure is 35. The next volume fraction (0.18, shown by open squares) is reached by following path 1 in the Figure 4.4.4 (a) and the required stiffness ratio increases 42 and gap closure falls ~ 12 %. When the volume fraction rises from 0.18 to 0.2, which is shown by path 2, the effect of increase volume fraction is reversed. The gap closure increase ~ 5 % and the best stiffness ratio decreases to 40. And as we further increase the volume fraction of machine to 0.4, this trend; gap closure increases and the stiffness ratio decreases is continued and when the volume fraction of machine is 0.4, the required stiffness ratio for optimum gap closure is 18. This is because, the whole gap closure behaviors of the HG-MAC is combination of the HG machine's structural characteristic itself and the deformation of the rubber like matrix. In other words, when the HG-MAC is compressed, the upper portion of the matrix will be compressed firstly and then transfer the compressive load into the HG machine and other remaining matrix. Consequently both HG machine's wall bent inward by the transferred compressive load from the top, lateral expansion of left and right portions of matrix and the characteristics of machine.

Through these machine and matrix deformation, the inner-channel area becomes effectively reduced as long as the matrix has proper stiffness.

As the volume fraction of the HG machine increases from 0.16 to 0.4, the matrix aided deformation becomes less since the gap closure behavior becomes mostly governed by the deformation of the HG machine itself due to not sufficient left and right volume of matrix. And to transfer the compressive stress effectively to the HG machine, the matrix should have higher stiffness. However when the volume fraction of the HG machine is low i.e., below 0.16, the matrix effect is more dominant than machine effect and the gap closure depends mostly on the matrix behavior. In this case, if the stiffness of the matrix is not high enough then the upper portion of the matrix can not transfer the compressive stress effectively to the remaining matrix and the walls of the HG machine may not be pushed effectively form the left and right portions of matrix. These results are displayed in Figure 4.35 (b) with schematic deformation mechanism and the arrow size of Figure 4.35 (b) indicates which constituent effect is more dominant.

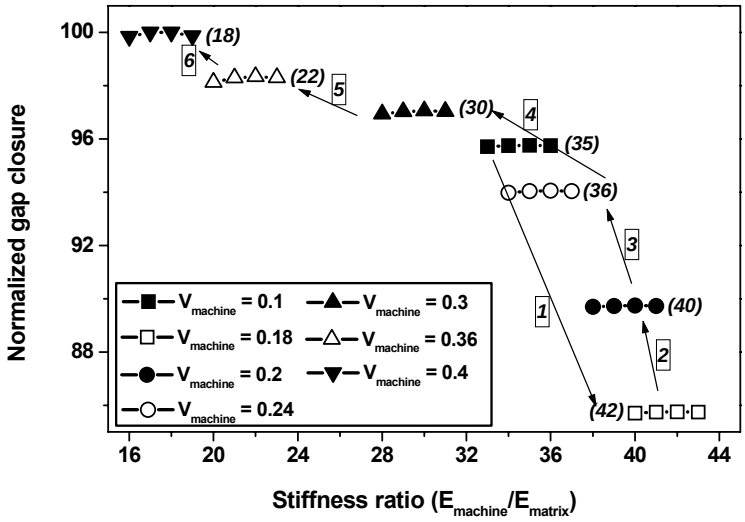

(a)

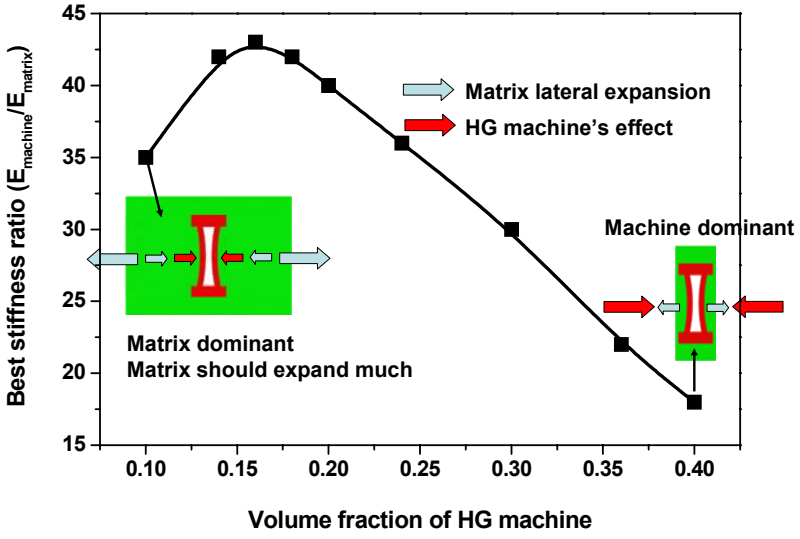

(b)

Figure 4.35. (a) Optimum stiffness ratio variation as a function of machine volume fraction (b) schematic deformation mechanism of unit cell.

Figure 4.36 shows the normalized gap closure of a unit HG-MAC as a function of machine volume fraction. Each point value in Figure 4.36 is obtained by using the optimum stiffness ratio values as shown in Figure 4.35 (a).

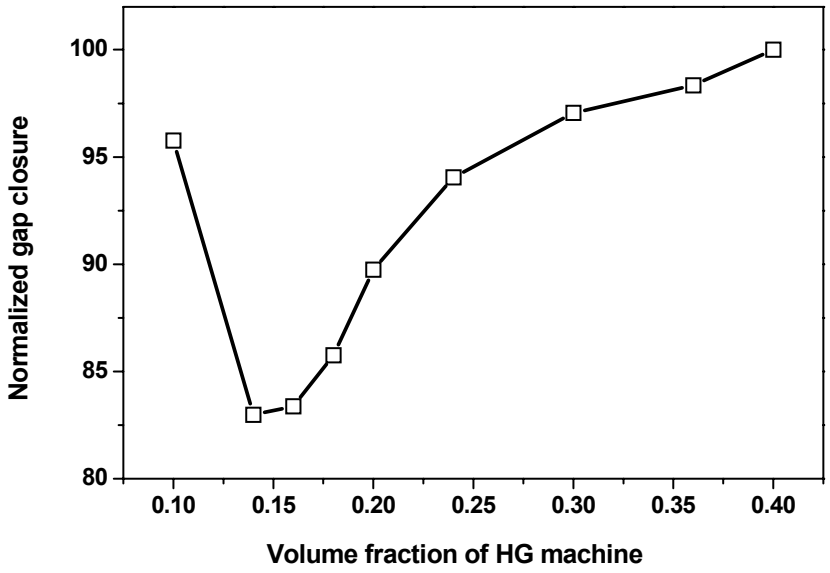

Figure 4.36. Normalized gap closure variation as a function of machine volume fraction of unit cell. Each point in the figure is calculated using the best stiffness ratio at that volume fraction.

4.4.2.2. Impact on Apparent Composite Stiffness

The machine volume fraction effects the constrained stiffness (E_{33}) and constrained Poisson's ratio (υ_{32}) of the unit cell, which are displayed in Figure 4.37 (a) and (b) respectively. In Figure 4.37, we compare the solitary cell properties with those of a matrix that contains no machine. Again each point value in the figure was obtained by using the optimum stiffness ratio.

The compression mechanical properties of elastomer like materials are sensitive to the shape factor and boundary conditions, which can be a bonded metal surface, unbonded clean surface, unbonded lubricated surface [61]. Here we use a 2D analysis with the plane strain assumption with attached skin surface conditions like Figure 3.12 (b). Also since we changed only the model width to generate each machine volume fraction this changes the shape factor. Therefore the apparent matrix stiffness values are different at each point and the Poisson's ratio value of matrix is much higher than its material properties. These calculated mechanical properties are the structural values and not the material properties.

Figure 4.37 (a) shows that increasing the volume fraction of the HG machine increases the stiffness of the HG-MAC like conventional fiber-reinforced composite materials. The stiffness of the unit HG-MAC shows 71 % ~ 200 % higher values than that of the matrix as the volume fraction of the machine increases.

The υ_{32} value of the solitary HG-MAC changes from 0.71 to 0.15 with increasing volume fraction and the value differences between the HG-MAC and the matrix becomes larger as the volume fraction increase as shown in Figure 4.37 (b). This is because as the volume fraction of the machine increases, the HG machine's roll becomes more dominant.

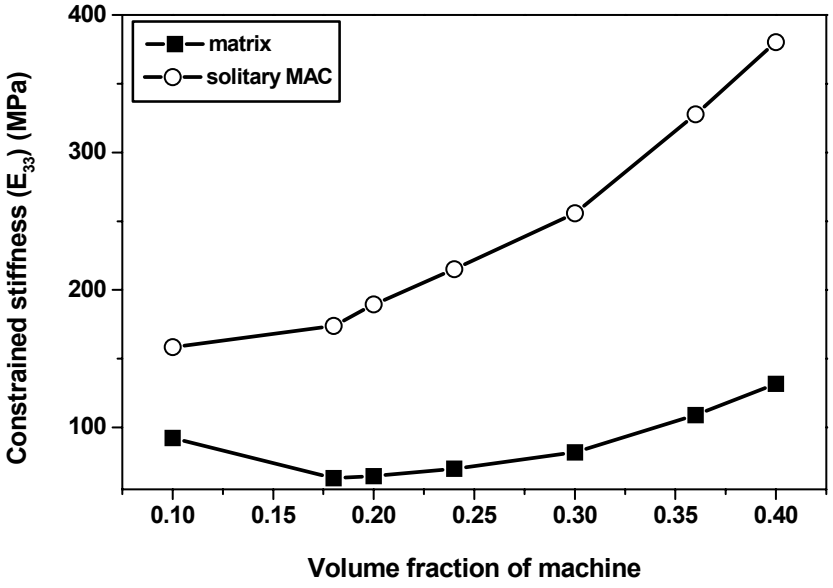

(a)

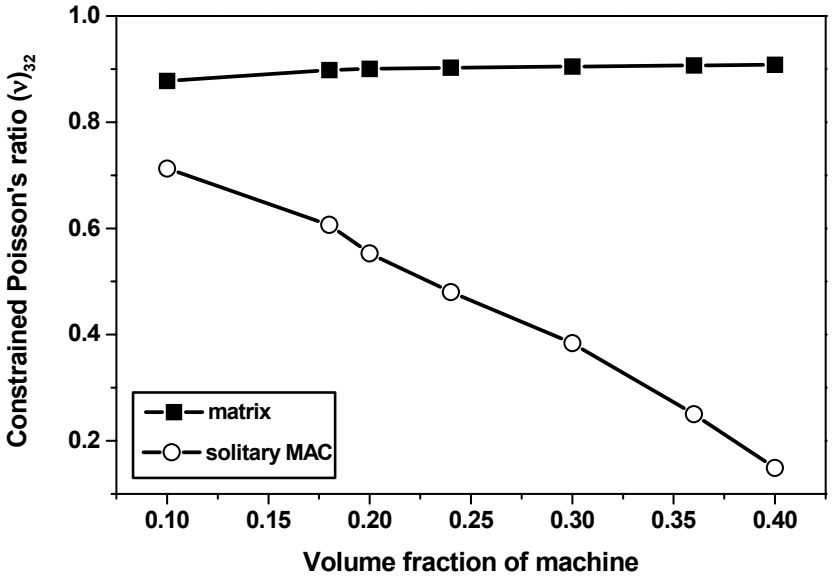

(b)

Figure 4.37. (a) E_{33} variation and (b) υ_{32} variation through change in volume fraction of the HG machine of solitary cell.

4.5. Numerical Analysis of Multi Cell Behaviors

The following analysis shows that HG-MAC lamina deformation behaviors are different from the single cell behaviors. The lamina mode was generated by using a series of 3, 5, 7, 9, and 11 cell arrays at each volume fraction. For this analysis the input material properties are the optimum properties obtained in the unit cell analysis with the applied pre-described displacement used before. Figure 4.38 (a) describes the matrix Poisson's ratio effect on the gap closure of a multi-cell array with a machine volume fraction of 0.3. As found in the unit cell cases, higher matrix Poisson's ratio produces more effective gap closure.

The gap closure behaviors with increasing the cell numbers in each volume fraction of machine appear in Figure 4.38 (b). Unlike the single cell case, increasing the volume fraction cause decreases the gap closure. In single cells, the edge of the HG-MAC is free to expand but when cells are buried in an array the edge of each HG-MAC works like a constraint and finally make the matrix movement difficult to outside and tends to move inside and push the HG machine's wall more strongly and this is the reason why multi-cell HG-MAC especially, low volume fraction of machine embedded HG-MAC, which has large amount of matrix volume cause the large gap closure than that of unit cell. The schematic deformation mechanism of multi cell is displayed in Figure 4.39. Also the gap closure comparison between unit cell and multi-cell as a function of volume fraction of machine is displayed in Figure 4.42 (a).

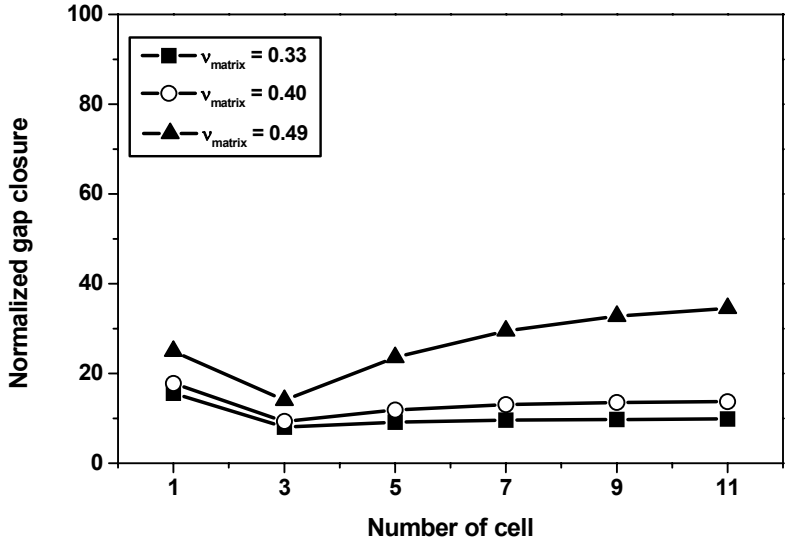

(a)

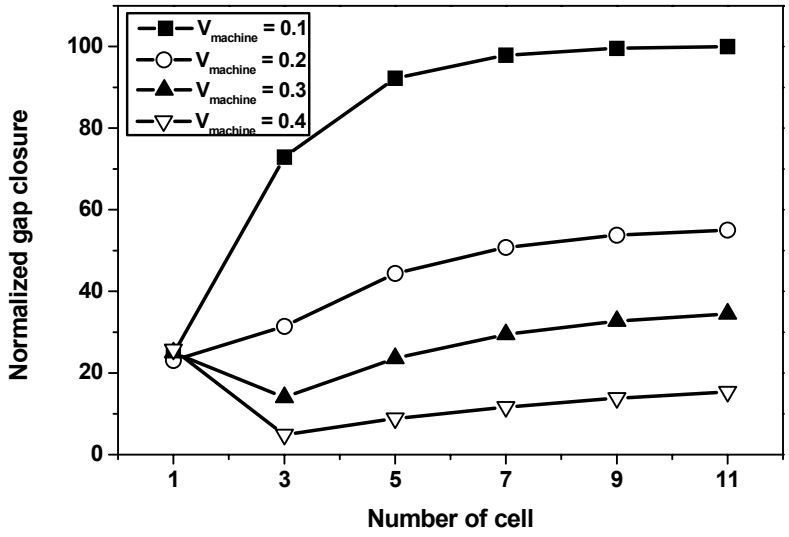

(b)

Figure 4.38. (a) Matrix Poisson's ratio dependent gap closure behavior with fixed machine volume fraction of multi-cell (b) gap closure variation as a function of number of cells.

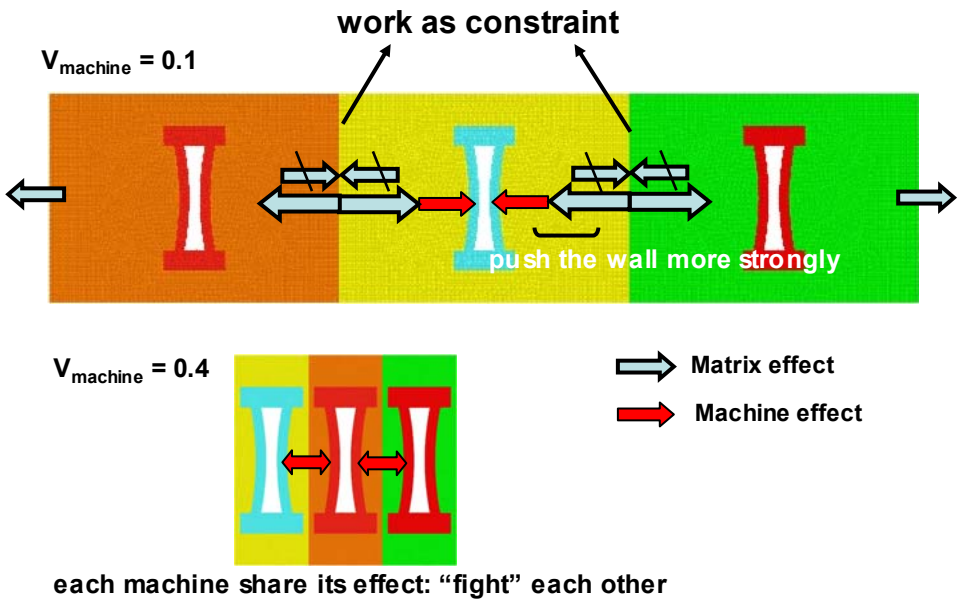

Figure 4.39. Schematic drawing of multi cell deformation behavior in low and high machine volume fraction cases.

With this machine volume fraction and adding array of cell relation, the performance of the HG-MAC can be determined with respect to the volume fraction of the HG machine.

There are two types of damping performance that we hope to achieve with machine augmented composites. The first type is inherent damping. We want to keep as much of the inherent damping that is present in the polymer matrix as possible. In this research that damping was measured experimentally. The second type of damping that we seek to employ is the damping that occurs from the fluid/solid interaction between the hourglass cells and the viscous fluid that they hold. This viscous damping cannot occur unless the HG MAC channels collapse and force the viscous fluid to flow.

Therefore, an objective of the research was to find the combination of materials that could produce the HG-MAC while maintaining the closing and opening of the channels. This need was used to define the pumping performance parameter. Therefore if the fluid pumped amount by same input condition is high we can speculate that the corresponding viscous dissipation is also high. The amount of fluid squeezed is proportional to the inner channel area reduction because of the incompressibility of the fluid. For these reasons, the performance of the HG-MAC was quantified by multiplying the percentage of inner-channel gap closure by the volume fraction of the machine. This product is proportional to the fluid pumping performance, however, it has no dimensions and it does not directly give a value for the fluid moved by the material. This study employ the 'performance' factor with a number with units of fluid volume moved per unit cell area, this has units of mm^3/mm^2. Figure 4.40 and 4.41 represent the relation between cross sectional area change and corresponding volume change with respect to the % gap closure respectively.

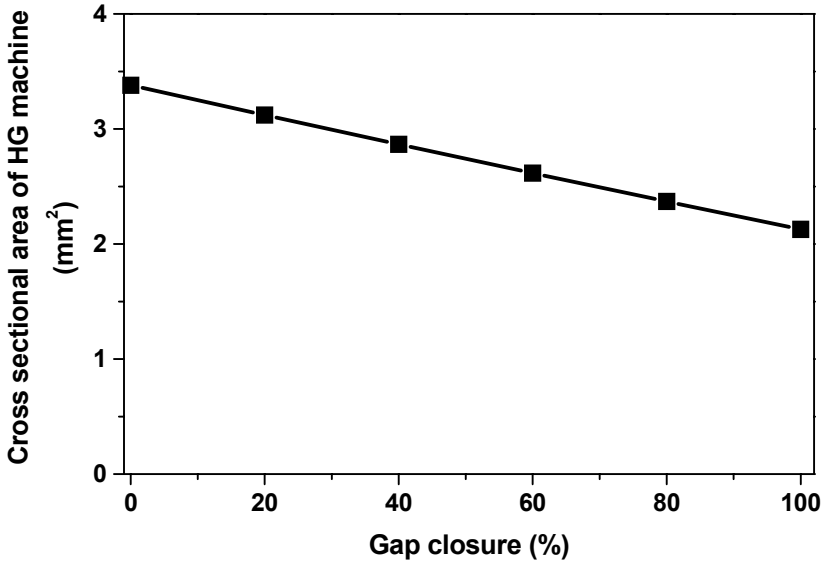

Figure 4.40. Relation between the cross sectional area change and the % gap closure of the inner channel of the HG machine.

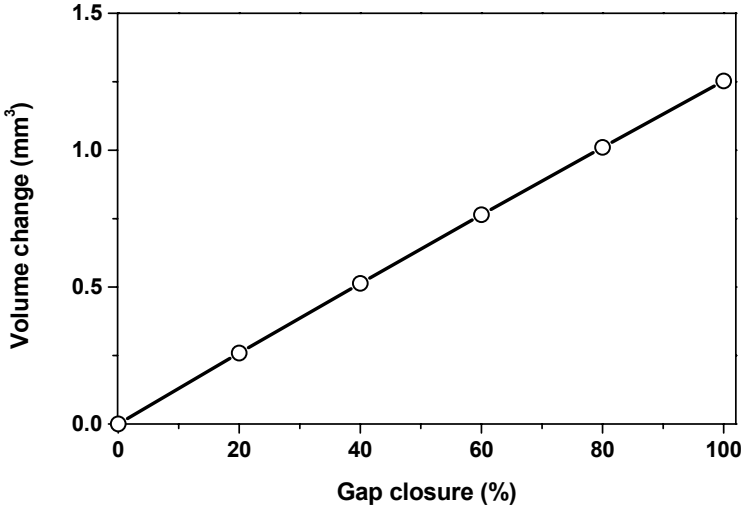

Figure 4.41. Relation between the volume change and the % gap closure of the inner channel of the HG machine.

With these reasons the performance is calculated by multiplying the normalized gap closure amount at 11 cell array in each machine volume fraction and the volume fraction of machine. This parameter indicates that if we apply same input, the resulting gap closure is affected by the machine volume fraction and there is an optimum volume fraction of machine for optimum efficiency. According to Figure 4.42 (a), we expected better performance of a unit cell when the volume fraction of the HG machine is high. However, in the multi cell case (Figure 4.42 (b)) the optimal performance of the HG-MAC is obtained when the volume fraction of machine is between 0.15 and 0.20. This means that lower or higher volume fraction of the machine decreases the HG-MAC lamina performance.

Figure 4.43 describes the required input displacements for 100 % gap closing of the center RVE of the model lamina HG-MAC, which is composed of 11 cells. As the machine volume fraction increases to 0.3, the required input displacement is almost linearly increased, but for the volume fraction of 0.4 case, we need larger input to overcome the machine effect.

Also from this chart we can make low frequency effective or high frequency effective HG-MAC by choosing the proper volume fraction of machine. Namely, we can not expect more damping from the HG-MAC than matrix at high frequency region because of physical limitation as shown in Figure 4.11, but since the low volume fractional machine augmented HG-MAC will work (viscous damping is possible) with smaller input, we can expect increased damping property at high frequency region when

we use the low volume fractional machine augmented composite with proper stiffness matrix.

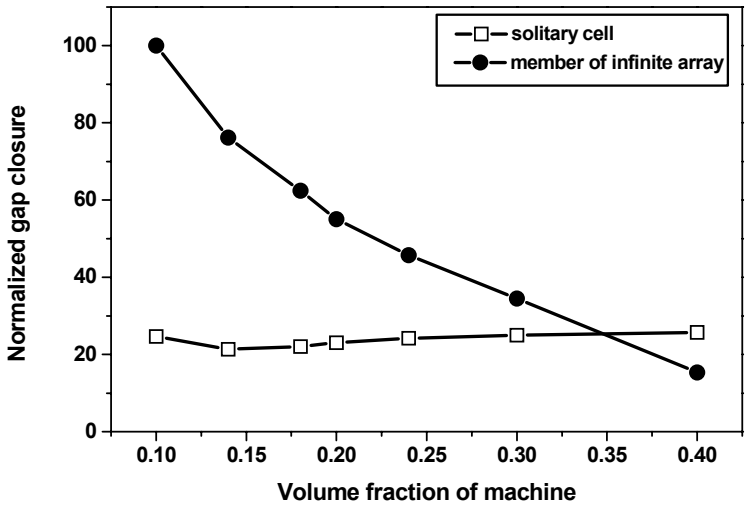

(a)

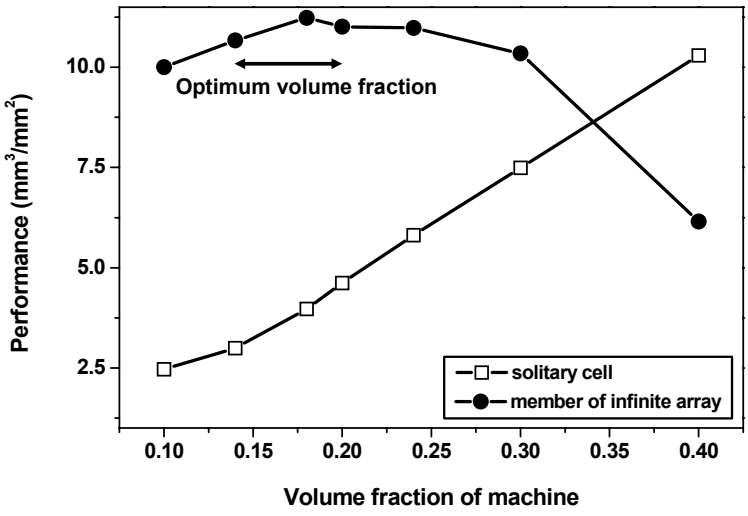

(b)

Figure 4.42. Comparison of unit cell and multi cell behaviors as a function of volume fraction of machine. (a) gap closure and (b) performance.

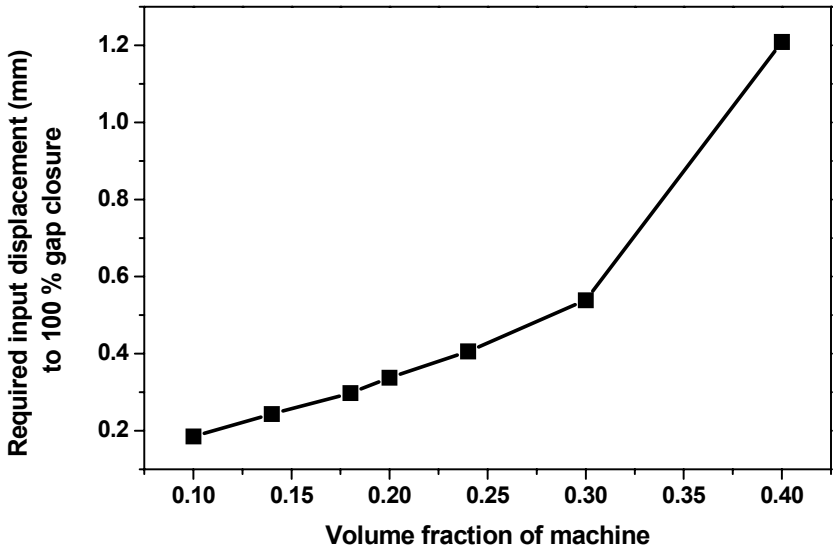

Figure 4.43. Required input displacement for 100 % gap closure for each volume fraction of machine.

At this point the ability of the HG-MAC to maintain -and in some conditions improve- inherent damping while gaining stiffness can not be explained. Although temperature of the elastomer rises during the experiments, it does not rise enough to contribute to damping. Although the matrix can absorb some of the immersion fluid, the damping with and without the fluid present is approximately the same. Therefore, we now look to the numerical analysis for evidence of a mechanism that presents high damping in a stiff structure.

Most constrained-layer damping treated structures are used in cyclic bending; the energy dissipation of these structures is due to the shear deformation of the damping layer. However when the shear modulus of the damping layer is low, the energy dissipation is minimal even though the shear deformation in the damping layer is high. According to the FEA study on the matrix and the HG-MAC, the in plane (σ_{yz}) and out

of plane (σ_{yx}) shear moduli of the 4 HG machine embedded HG-MAC (same as the experimental specimen) are ~ 8 times and ~ 130 times higher than those of the matrix.

The experimental results of this study showed the HG-MAC has similar damping properties as matrix irrespective of its ~130 % higher compressive stiffness. To see the cause of this result, strain energy (U) was investigated through FEA. The strain energy is composed of sum of the dilatational energy due to change in volume, which is a shear-free deformation, and the distortional or deviatoric energy, which includes shear strains. The definition of distortional energy is the potential energy that results from the change in shape of an elastically deformed body. We suspect that the reason HG-MAC can keep the damping properties comes from higher strain energy density due to the existence of the rigid HG machine.

The FEA analysis was performed to calculate the distortional energy of the neat matrix and the matrix portion of the HG-MAC. Two forms of HG-MAC were used. The first was a solitary HG machine in an elastomer matrix. The second was a three machine array; only the deviatoric energy of the center cell was calculated because this is more characteristic of a representative volume element in a large or infinite array of machines. The distortional energy at each case is calculated by using following equation:

$$U_{Distortional} = \frac{1}{12G}[(\sigma_1 - \sigma_2)^2 + (\sigma_2 - \sigma_3)^2 + (\sigma_1 - \sigma_3)^2] \tag{4.4}$$

where σ_3, σ_2, σ_1 is the minimum, intermediate, and maximum principle stresses respectively. G is the matrix shear modulus.

Figure 4.44 displays the comparison of the distortional energy between the neat matrix and the matrix portion of the HG-MAC and the material for both cases are assumed to be soft polyurethane with E = 4.12 MPa and υ = 0.49. The Figure 4.44 shows that the distortional energy from the HG-MAC (0.20 J/m^3) is ~ 6 times higher than the neat matrix (3.15 x 10^{-2} J/m^3) and also from Figure 4.45, the distortional energy of the HG-MAC is almost unchanged with respect to the measured position (0.225 J/m^3 from the edge and 0.229 J/m^3 from the middle) while those from the neat matrix decreased ~ 30 % as the measured position moved into the middle portion. (4.763 x 10^{-2} J/m^3 from the edge and 3.677 x 10^{-2} J/m^3 from the middle) Form this, we can suspect that in the HG-MAC case uniformly introduced rigid structure (HG machine) cause uniform distribution of the distortional energy in everywhere among the matrix and this cause the HG-MAC contains high inherent damping.

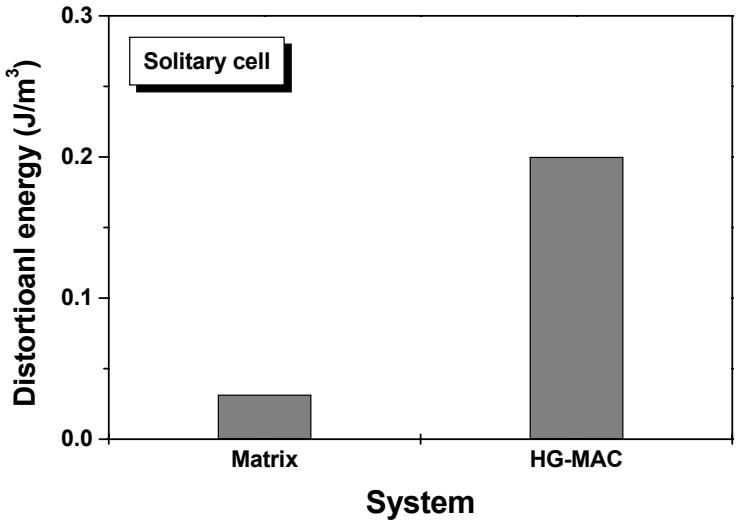

Figure 4.44. Distortional energy comparison between neat matrix and the matrix portion of the HG-MAC of a solitary cell.

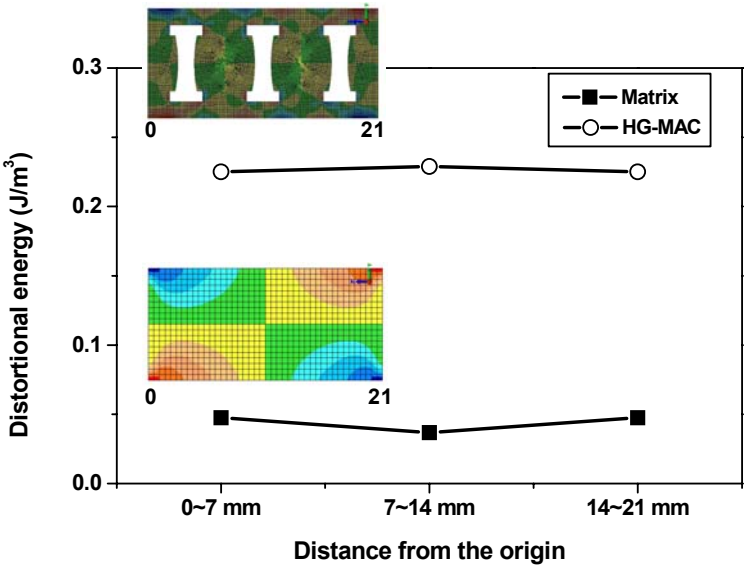

Figure 4.45. Distortional energy comparison between neat matrix and the matrix portion of the HG-MAC of 3 cell array as a function of distance.

4.6. Enhancement of HG-MAC's Functionality

From the previous numerical analysis, the optimum performance of the HG-MAC lamina can be available when the Poisson's ratio of the matrix is 0.49, which shows Figure 4.32, the volume fraction of the HG machine is between 0.15 and 0.2, which Figure 4.42 (b) shows and the $E_{machine}/E_{matrix}$ ratio is between 40 and 43, which Figure 4.35 shows.

According to the analytical and experimental results, currently measured longitudinal (11 direction) and transverse directional (33 direction) stiffness of the 4 HG machine embedded HG-MAC were 236 MPa and 15.78 MPa respectively and the measured transverse directional tan δ value was 0.05 ~ 0.22 at the frequency of 1 ~ 40

Hz and with these experimental results, we can locate our current status like Figure 4.46 (a) and (b) respectively and every data in this figure is obtained from 25 ^{o}C testing [9].

The dashed line in Figure 4.46 guides the eye to show the stiffness/damping limit of current structural materials. As the material properties approaches to the upper right corner the material can be thought of as a high performance material.

In other words, materials like steel and aluminum alloy are stiff with lower damping but polymer materials like PMMA have lower stiffness with high damping. This inversely proportional stiffness-damping relationship places performance limits on materials chosen for structures.

In Figure 4.46 the HG-MAC shows improvement in both longitudinal and transverse stiffness values without sacrificing the tan δ value with respect to the matrix but the stiffness of the HG-MAC, especially the transverse directional stiffness is still relatively low when compared with other structural materials.

This low stiffness in 33 direction of the HG-MAC is caused by the inner channel of the HG machine. Namely, to maintain or enhance the damping property of the HG-MAC we have introduced an inner channel into the HG machine as shown in Figure 3.1 (a). This structural characteristic makes the transverse stiffness of the HG-MAC smaller.

Also, the numerical analysis results show that our experimental parameters were not the optimum values for the best performance of the HG-MAC. The stiffness ratio of experimental materials was 400; this is much higher than the optimum stiffness ratio of 42 ~ 43. This means the stiffness of the matrix used in the experiments was ~ 10 times

lower, i.e., too compliant than desired and that due to this the HG-MAC shows low efficiency in both gap closing and stiffness.

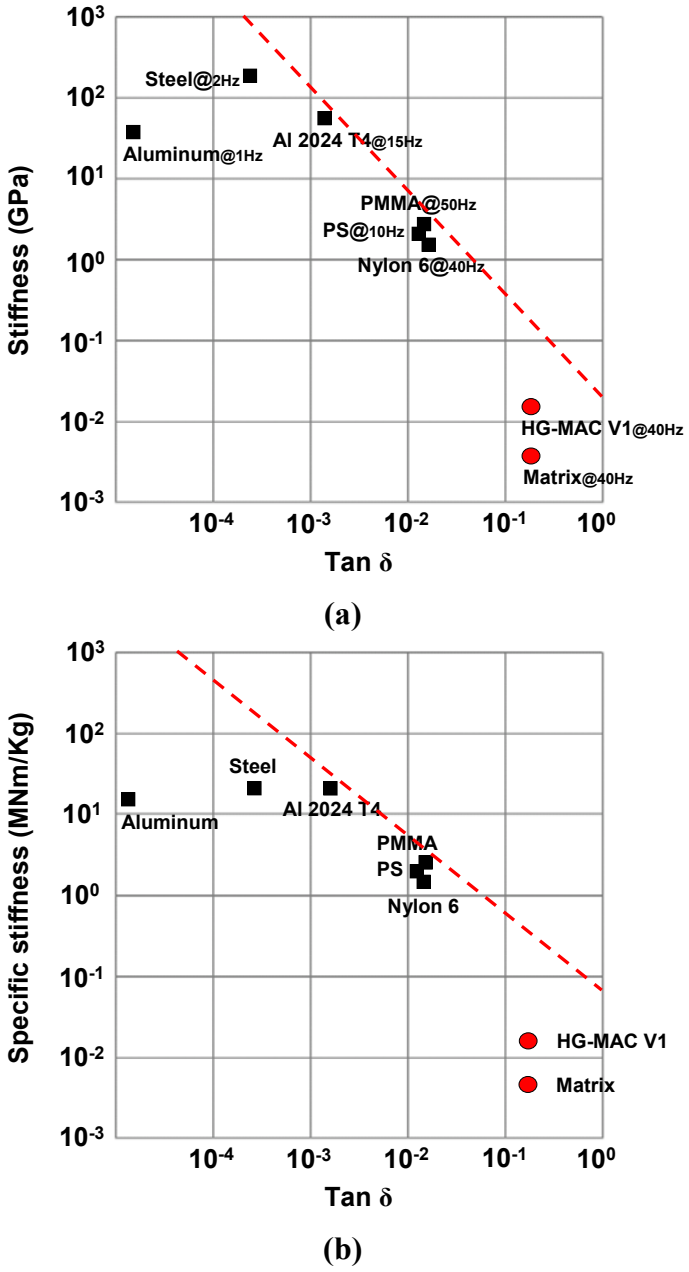

Figure 4.46. Current status of the HG-MAC at 40 Hz in (a) stiffness/tan δ domain and (b) specific stiffness/ tan δ domain.

The FEA results show that there are ways of increasing the multi functionality (enhancement of both stiffness and damping) of the current HG-MAC can be achieved by modifying the matrix property and the composite geometry.

4.6.1. Stiffening Method of HG-MAC

In this sub section, the possible stiffening method of current HG-MAC and corresponding damping properties change will be discussed.

The first option for increasing the stiffness of the HG-MAC is to replace the soft polyurethane matrix with an optimum stiffness material that is ~ 10 times stiffer.
This stiffer material would produce a small-input displacement HG-MAC that would be especially good for a high frequency damping application. The numerical analysis show that the gap closure will be increased ~57 % and the stiffness will rise ~330 %.

However if we keep the current HG machine material with E equals to 1649 MPa, there are no materials for matrix that have a stiffness of ~ 39 MPa and a Poisson's ratio of 0.49. Figure 4.47 [63, 64] shows a sample of polymer arranged by their Poisson's ratio and the ratio of their stiffness and rigid polyurethane. Choosing a material softer than desired would give worse performance than the optimum. Choosing a stiffer material –those in the left of the target- would require replacing the HG machine material with a higher stiffness material.

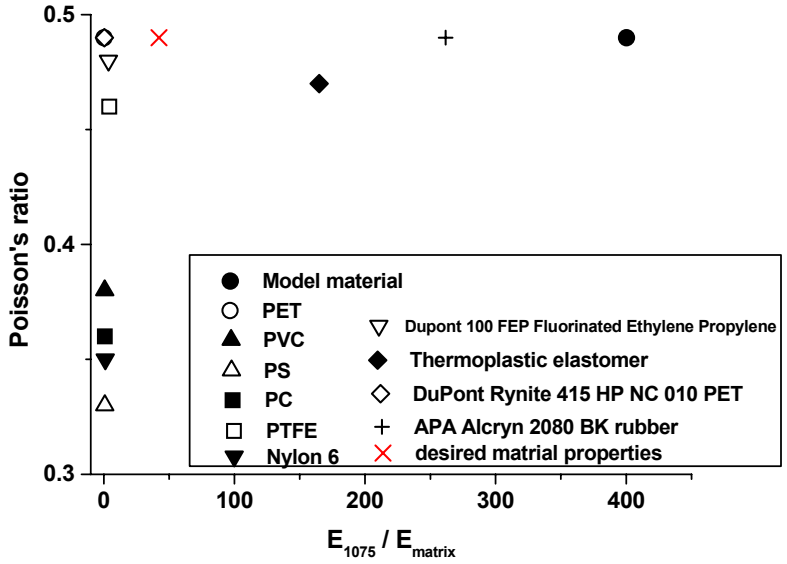

Figure 4.47. Mechanical properties of polymer materials.

Another option for increasing the stiffness of the HG-MAC is to convert the current HG-MAC structure into a sandwich structure by replacing the top and bottom regions of soft polyurethane with high stiffness skins such as steel, Al 2024-T4 or high stiffness composite materials. A schematic view of this stiffening method appears Figure 4.48 and the mechanical properties of each face material appear Table 4.6.

The basic assumption of this approach is that the damping of the HG-MAC structure depends on the amount of gap closing, i.e., as long as the inner-channel gap is properly closed, the damping of the structure will not be changed.

The first step in creating a sandwich MAC is to determine both the right volume fraction of the HG machine and appropriate matrix stiffness through numerical analysis of an array of HG-MAC cells.

The numerical analysis result is similar to the previous cases, i.e., gap closure is affected by the matrix Poisson's ratio and stiffness. However, at this time the HG machines are directly compressed by the face materials. This makes the optimum matrix stiffness much smaller. Therefore, the soft polyurethane model material was set as component B in Figure 4.48 and we calculated the other properties.

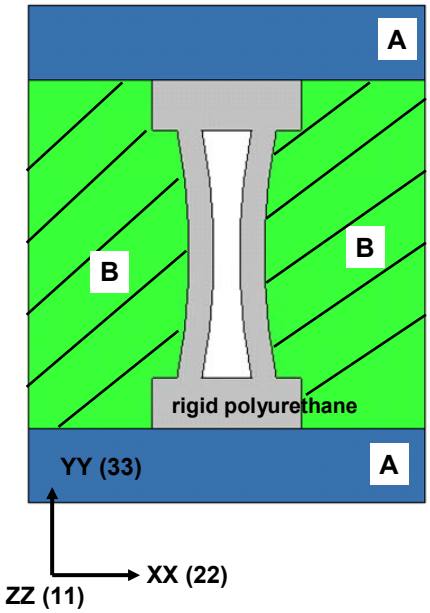

Case	Skin material (A)
V1	Soft polyurethane
V2	Rigid polyurethane
V3	Steel
V4	Aluminum
V5	Al2024 T4
V6	Nylon 6
V7	Polystyrene (PS)
V8	PMMA
V9	E-glass/epoxy (11 direction)
V10	Kevlar/epoxy (11 direction)
V11	Carbon/epoxy (11 direction)
V12	Graphite/epoxy (11 direction)

Figure 4.48. Stiffening methods for HG-MAC include converting the material into a sandwich structure. In every case B is whatever matrix that further FEA is needed for produce an effective panel.

Table 4.6. Basic mechanical properties of face materials.

Face materials	E_{11} (GPa)	E_{22} (GPa)	$\upsilon_{12} = \upsilon_{13}$	υ_{21}	Density (g/cm^3)	Classification V = version
1075 Rigid polyurethane	1.65	1.65	0.33	0.33	1.14	V2
Steel	207	207	0.3	0.3	7.85	V3
Aluminum	69	69	0.33	0.33	2.71	V4
Al 2024 T4	72.4	72.4	0.33	0.33	2.77	V5
Nylon6	2.3	2.3	0.35	0.35	1.17	V6
Polystyrene	2.5	2.5	0.33	0.33	1.05	V7
PMMA	3.0	3.0	0.40	0.4	1.19	V8
E-glass/epoxy ($V_f = 0.55$)	39	8.6	0.28	0.06	2.10	V9
Kevlar/epoxy ($V_f = 0.6$)	87	5.5	0.34	0.02	1.38	V10
Carbon/epoxy ($V_f = 0.65$)	177	10.8	0.27	0.02	1.60	V11
Graphite/epoxy ($V_f = 0.57$)	294	6.4	0.23	0.01	1.59	V12

Figure 4.49 compares the normalized gap closure of a solitary cell between the best stiffness ratio applied HG-MAC and the sandwich HG-MAC (using rigid

polyurethane face: HG-MAC V2) as a function of machine volume fraction. Also Figure 4.50 (a) displays the normalized gap closure of the sandwich HG-MAC as a function of number of cell. The trend of gap closure behavior is same as before i.e., increasing the volume fraction of machine causes less gap closure due to the machine effect and after adding 3 cells, the whole gap closure is almost same up to 15 cells in all different volume fractional cases.

However the gap closure amount of the sandwich HG-MAC is much higher both solitary cell and infinite array cases than the previous best stiffness ratio applied HG-MAC case like Figure 4.50 (b), because of the direct compression of the HG machine.

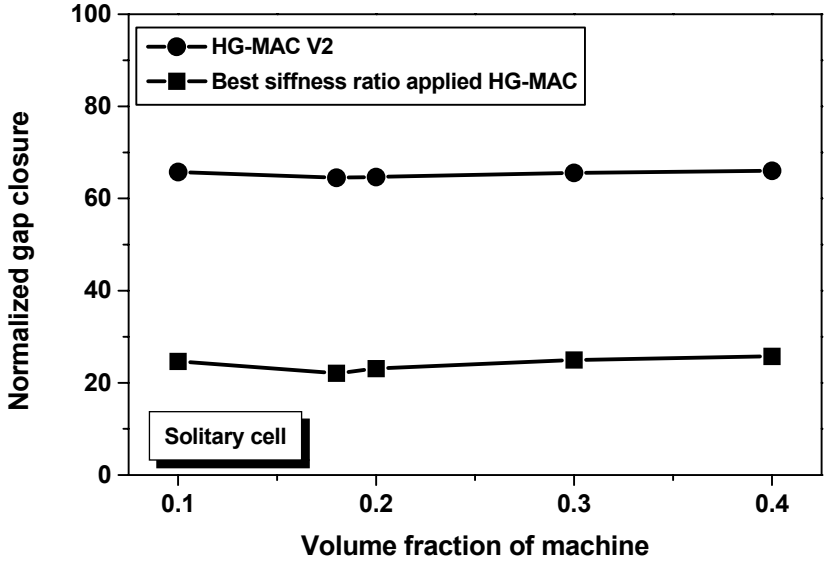

Figure 4.49. Gap closure comparison between the best stiffness ratio applied HG-MAC and rigid PU skin sandwich HG-MAC (HG-MAC V2) of a solitary cell.

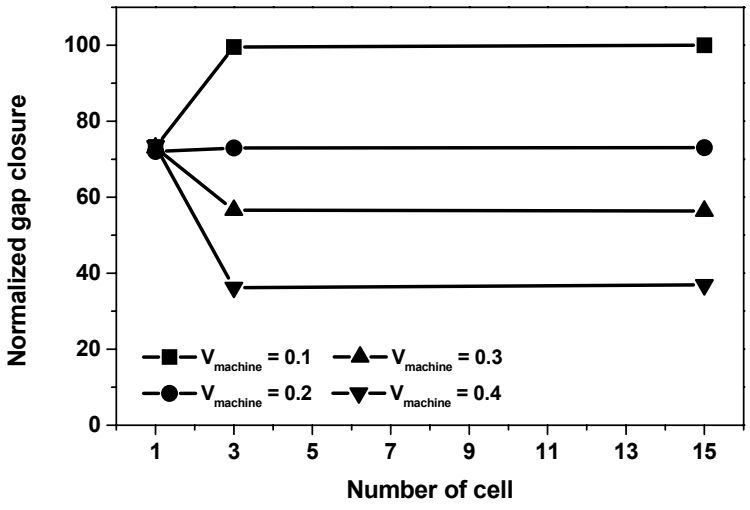

(a)

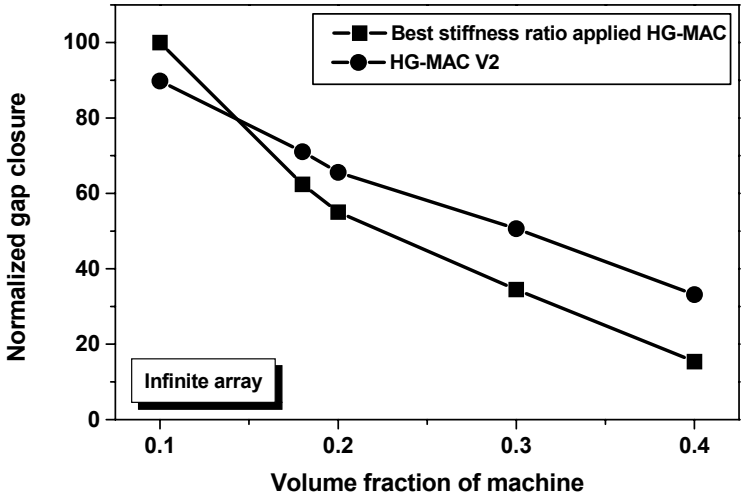

(b)

Figure 4.50. (a) Gap closure of the sandwich HG-MAC (HG-MAC V2) as a function of number of cells and (b) Gap closure comparison between the best stiffness ratio applied HG-MAC and HG-MAC V2 of infinite array.

From these results, the performance of the HG-MAC V2 can be predicted and Figure 4.51 presents the performance comparison of a solitary cell and an infinite array between the best stiffness ratio applied HG-MAC and sandwich HG-MAC.

In Figure 4.51 (a) the performance of the solitary celled HG-MAC V2 (rigid PU skin) increases as the volume fraction of machine increases and like the best stiffness applied HG-MAC. However the performance of the HG-MAC V2 is higher than the best stiffness applied HG-MAC because the gap closure is more effective.

Figure 4.51 (b) also shows, the overall performance of the infinite arrayed HG-MAC V2 is higher than that of best stiffness applied HG-MAC and the optimum volume fraction of the HG-MAC V2 was 0.3.

The preferred volume fraction of the HG machine for the optimum performance shifts from 0.2 to 0.3 as the HG-MAC becomes sandwich structure and this is due to the less differences of gap closure between each volume fractional case in sandwich HG-MAC structure.

Based on these results the thickness direction (33) stiffness and gap closure of sandwich HG-MAC (HG-MAC V2 through V12) was studied with $V_{machine}$ set to 0.3. The expected properties were obtained on the assumption that the sandwich HG-MAC structure is infinitely long in 11 direction – that is plane strain in 11 direction- and also that was in the 22 direction (infinitely wide in 22 direction) , and these conditions were obtained by adding symmetry conditions on vertical walls of a solitary cell. Other boundary conditions are same as previous numerical analysis and the differences

regarding gap closure and stiffness of this analysis are less than 5% from the previous 11 ~ 15 cell added model.

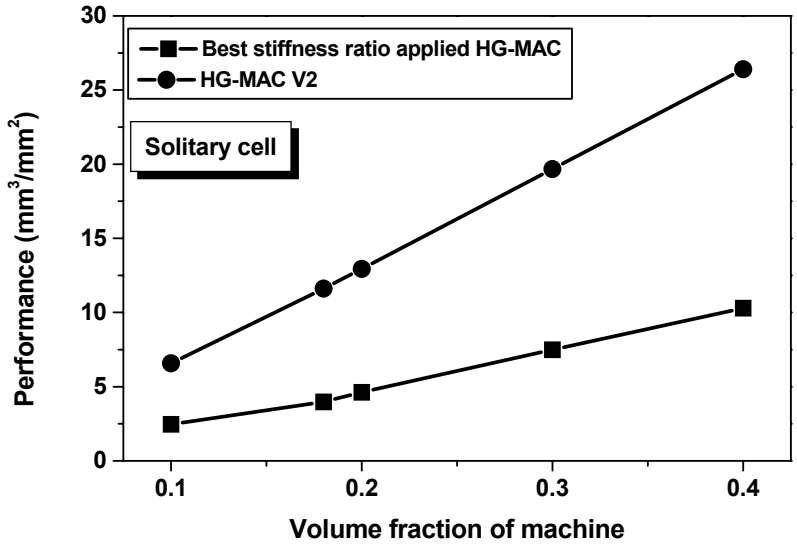

(a)

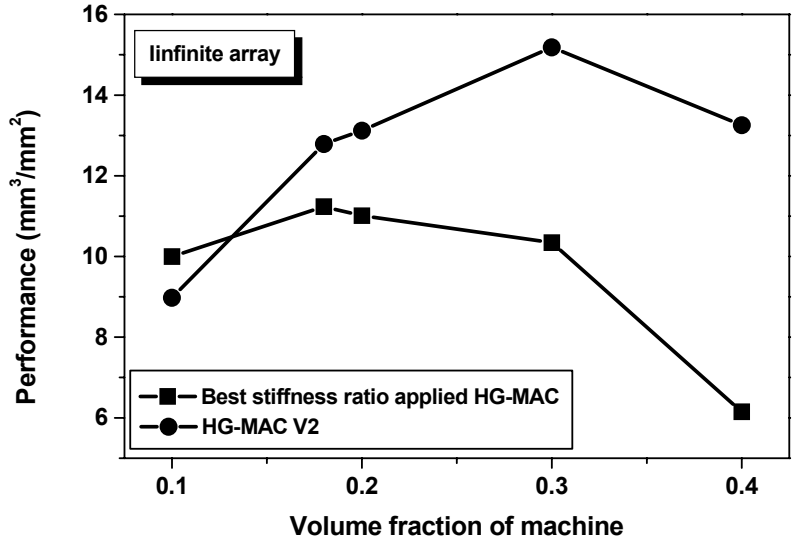

(b)

Figure 4.51. Performance comparison between best stiffness ratio applied HG-MAC and HG-MAC V2 of (a) solitary cell and (b) infinite array cases.

Figure 4.52 and Figure 4.53 compare the expected gap closure and 33 directional compressive stiffness of various face material attached sandwich HG-MAC with those of the default HG-MAC V1 that had a soft polyurethane matrix and rigid polyurethane machines through numerical analysis. Converting the HG-MAC structure into the sandwich structure enhances gap closure by ~ 90 % and increases stiffness by ~ 500 %. However, Figure 4.52 and Figure 4.53 show that once the top and bottom portions of the HG-MAC is replaced by any stiff skin, i.e., as long as $E_{face}/E_{machine} \geq 1$ there is little difference in gap closure and 33 directional stiffness. These results also show that there is a limitation to increasing the 33 directional stiffness of the HG-MAC that is caused by the open channel of the HG machine.

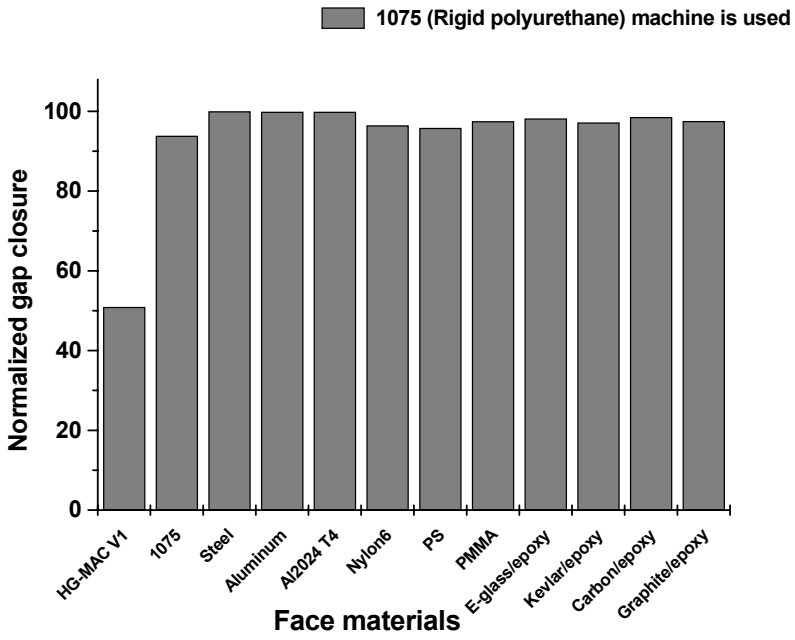

Figure 4.52. Gap closure comparisons between default HG-MAC with various face material attached sandwich HG-MAC.

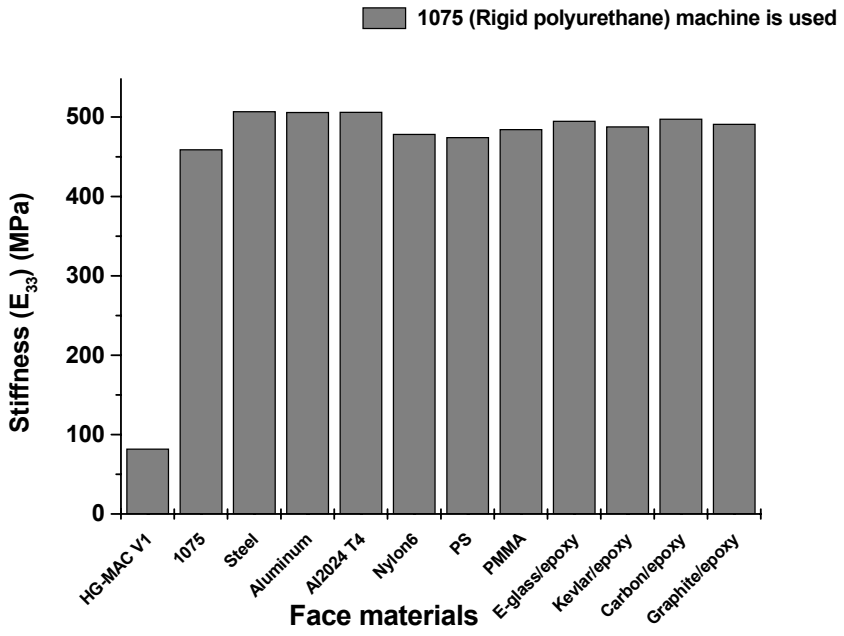

Figure 4.53. The 33 directional stiffness comparisons between default HG-MAC with various face material attached sandwich HG-MAC.

At this point the only way of further increasing the 33 directional stiffness is replacing the machine materials with stiffer materials like Nylon 6. Making the machine materials stiffer will work because the sandwich HG-MAC performs better at a high $E_{machine}/E_{matrix}$ ratio and Nylon 6 machines in soft polyurethane matrix material would have a ratio of 650. Figure 4.54 (a) displays the expected 33 directional stiffness of sandwich HG-MAC at this condition and through this modification, we can expect an additional ~ 60 % enhanced stiffness and finally we can construct theoretical stiffness-loss map like Figure 4.54 (b) on the assumption of that damping is not changed.

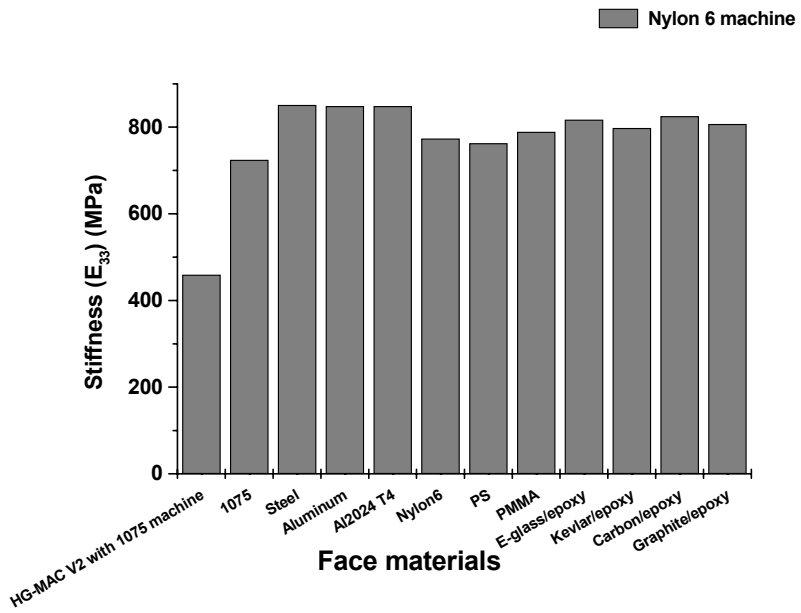

(a)

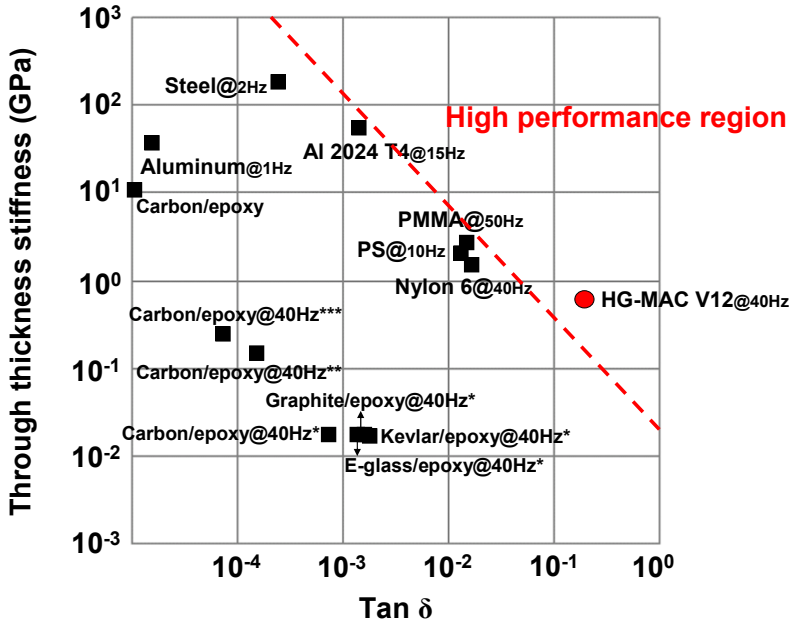

(b)

Figure 4.54. (a) Expected 33 directional stiffness with Nylon 6 machine and various face materials (b) stiffness-loss map of Nylon 6 machine reinforced sandwich HG-MAC and various structural materials including a standard composite/elastomer panel.

Figure 4.54 (b) shows the result of my analysis of carbon, Kevlar, and glass panels with a damping layer of elastomer attached to them with composite/elastomer layer thickness ratios of 1, 0.5, and 0.25. As the elastomer rises from 50% of the panel volume it improves the damping, but at the cost of decreasing the stiffness of the laminate.

FEA analysis provided the stiffness of each panel. The tan δ of a free-layer damping treatment can be modeled using Equation 2.15 in the dissertation while using a tan δ of 0.2, which is my measured value for the soft polyurethane. Figure 4.54 (b) shows that carbon/epoxy without the elastomer layer is almost as stiff as aluminum, but it has a lower tan δ. Adding an equal thickness of elastomer drops the stiffness by over one order of magnitude while it almost increases the damping by one order of magnitude. However, the carbon/epoxy+elastomer still has a lower tan δ than a steel plate. Increasing the elastomer to 2/3 of the panel volume slightly lowers stiffness and slightly increases the lass factor. Finally, if the elastomer is 75% of the panel volume, a loss factor that is two orders of magnitude higher than carbon/epoxy alone is obtained. Unfortunately this came with a stiffness reduction of 3 orders of magnitude. The HG MAC panels appear in the region of high damping and moderate stiffness.

4.6.2. Bending Stiffness of HG-MAC

The other advantage of transferring the HG-MAC structure into the sandwich structure will be the increased bending stiffness (D_{ij}) and bending stiffness of the sandwich structure can be approximated with conventional laminate composite analysis [11, 55, 56, 57, 58, 65].

In most structural applications composite materials are used in the form of thin lamina loaded laminate like Figure 4.55.

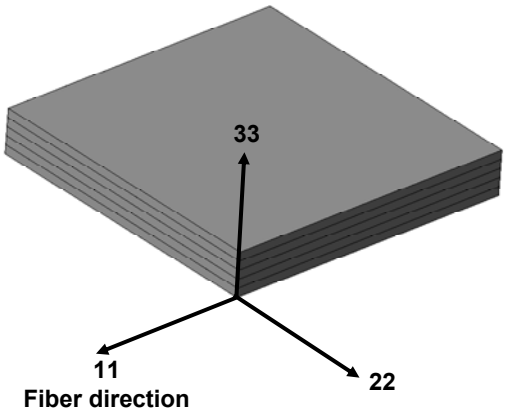

Figure 4.55. Laminate shape composed of thin 5-ply lamina.

Thus composite lamina can be considered to be under a condition of plane stress, i.e.,

$$\sigma_{33} = 0 \quad \tau_{23} = \tau_{13} = 0 \tag{4.5}$$

Then the orthotropic stress-strain relation becomes

$$\begin{bmatrix} \sigma_{11} \\ \sigma_{22} \\ 0 \\ 0 \\ 0 \\ \tau_{12} \end{bmatrix} = \begin{bmatrix} C_{11} & C_{12} & C_{13} & 0 & 0 & 0 \\ C_{12} & C_{22} & C_{23} & 0 & 0 & 0 \\ C_{13} & C_{23} & C_{33} & 0 & 0 & 0 \\ 0 & 0 & 0 & C_{44} & 0 & 0 \\ 0 & 0 & 0 & 0 & C_{55} & 0 \\ 0 & 0 & 0 & 0 & 0 & C_{66} \end{bmatrix} \begin{bmatrix} \varepsilon_{11} \\ \varepsilon_{22} \\ \varepsilon_{33} \\ \gamma_{23} \\ \gamma_{13} \\ \gamma_{12} \end{bmatrix} \tag{4.6}$$

when we expand above matrix

$$\begin{aligned}
\sigma_{11} &= C_{11}\varepsilon_{11} + C_{12}\varepsilon_{22} + C_{13}\varepsilon_{33} \\
\sigma_{22} &= C_{12}\varepsilon_{11} + C_{22}\varepsilon_{22} + C_{23}\varepsilon_{33} \\
0 &= C_{13}\varepsilon_{11} + C_{23}\varepsilon_{22} + C_{33}\varepsilon_{33} \\
\gamma_{23} &= \gamma_{13} = 0 \\
\tau_{12} &= C_{66}\gamma_{12}
\end{aligned} \tag{4.7}$$

elimination of ε_{33} from equation (4.7) yields

$$\begin{aligned}
\sigma_{11} = \sigma_1 &= (C_{11} - \frac{C_{13}C_{12}}{C_{33}})\varepsilon_1 + (C_{12} - \frac{C_{13}C_{23}}{C_{33}})\varepsilon_2 = Q_{11}\varepsilon_1 + Q_{22}\varepsilon_2 \\
\sigma_{22} = \sigma_2 &= (C_{12} - \frac{C_{23}C_{13}}{C_{33}})\varepsilon_1 + (C_{22} - \frac{C_{23}C_{23}}{C_{33}})\varepsilon_2 = Q_{12}\varepsilon_1 + Q_{22}\varepsilon_2 \\
\tau_{12} = \tau_6 &= C_{66}\gamma_6 = Q_{66}\gamma_6
\end{aligned} \tag{4.8}$$

Thus in-plane stress-strain relations for an orthotropic layer under plane stress can be expressed in the reduced stiffnesses Q_{11}, Q_{22} and Q_{66} using this equation;

$$\begin{bmatrix} \sigma_1 \\ \sigma_2 \\ \tau_6 \end{bmatrix} = \begin{bmatrix} Q_{11} & Q_{12} & 0 \\ Q_{12} & Q_{22} & 0 \\ 0 & 0 & Q_{66} \end{bmatrix} \begin{bmatrix} \varepsilon_1 \\ \varepsilon_2 \\ \gamma_6 \end{bmatrix} \tag{4.9}$$

where

$$\begin{aligned}
Q_{11} &= \frac{E_1}{1 - \upsilon_{12}\upsilon_{21}} \\
Q_{12} &= \frac{E_1\upsilon_{21}}{1 - \upsilon_{12}\upsilon_{21}} = \frac{E_2\upsilon_{12}}{1 - \upsilon_{12}\upsilon_{21}} \\
Q_{22} &= \frac{E_2}{1 - \upsilon_{12}\upsilon_{21}} \\
Q_{66} &= G_{12}
\end{aligned} \tag{4.10}$$

When we consider the elastic behavior of multidirectional laminates then the strains at any point in the laminate to the reference plane strain (ε_i^0) and the laminate curvatures (κ_i^0) can be expressed as follows

$$\begin{bmatrix} \varepsilon_x \\ \varepsilon_y \\ \gamma_s \end{bmatrix} = \begin{bmatrix} \varepsilon_x^{\,0} \\ \varepsilon_y^{\,0} \\ \gamma_s^{\,0} \end{bmatrix} + z \begin{bmatrix} \kappa_x \\ \kappa_y \\ \kappa_s \end{bmatrix} \tag{4.11}$$

After transformation to the laminate coordinate system, equation (4.6.5) can be expanded as

$$\begin{bmatrix} \sigma_x \\ \sigma_y \\ \tau_s \end{bmatrix} = \begin{bmatrix} Q_{xx} & Q_{xy} & Q_{xs} \\ Q_{yx} & Q_{yy} & Q_{ys} \\ Q_{sx} & Q_{sy} & Q_{ss} \end{bmatrix}_k \begin{bmatrix} \varepsilon_x \\ \varepsilon_y \\ \gamma_s \end{bmatrix} = \begin{bmatrix} Q_{xx} & Q_{xy} & Q_{xs} \\ Q_{yx} & Q_{yy} & Q_{ys} \\ Q_{sx} & Q_{sy} & Q_{ss} \end{bmatrix}_k \begin{bmatrix} \varepsilon_x^{\,0} \\ \varepsilon_y^{\,0} \\ \gamma_s^{\,0} \end{bmatrix} + z \begin{bmatrix} Q_{xx} & Q_{xy} & Q_{xs} \\ Q_{yx} & Q_{yy} & Q_{ys} \\ Q_{sx} & Q_{sy} & Q_{ss} \end{bmatrix}_k \begin{bmatrix} \kappa_x \\ \kappa_y \\ \kappa_s \end{bmatrix}$$

$$\therefore [\sigma]^k{}_{x,y} = [Q]^k{}_{x,y}[\varepsilon^0]_{x,y} + z[Q]^k{}_{x,y}[\kappa]_{x,y} \tag{4.12}$$

Because of the discontinuous variation of stresses from layer to layer, it is more convenient to deal with the integrated effect of these stresses on the laminate like Figure 4.56 and this figure shows the resulting forces, moments of the lamina plate.

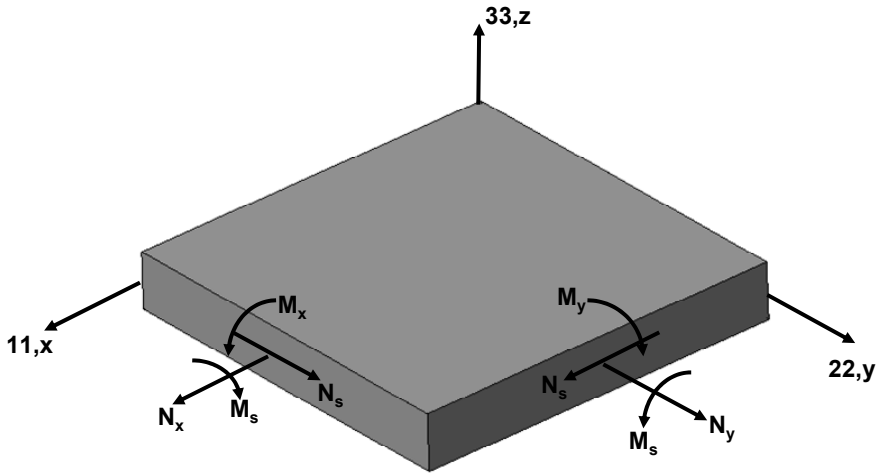

Figure 4.56. Element of single layer with force and moments resultants.

The resulting forces and moments are

Normal force/unit length (N_x^k, N_y^k):
$$N_x^k = \int_{-t/2}^{t/2} \sigma_x dz \qquad N_y^k = \int_{-t/2}^{t/2} \sigma_y dz \tag{4.13}$$

Shear force/unit length ($N_{xy}^k = N_s^k$): $N_s = \int_{-t/2}^{t/2} \tau_s dz$ (4.14)

Bending moment/unit length (M_x^k, M_y^k):
$$M_x^k = \int_{-t/2}^{t/2} \sigma_x z dz \qquad M_y^k = \int_{-t/2}^{t/2} \sigma_y z dz \tag{4.15}$$

Twisting moment/unit length (M_s^k): $M_s = \int_{-t/2}^{t/2} \tau_s z dz$ (4.16)

Therefore the total force and moment are

$$\begin{bmatrix} N_x \\ N_y \\ N_s \end{bmatrix} = \sum_{k=1}^{n} \int_{h_{k-1}}^{h_k} \begin{bmatrix} \sigma_x \\ \sigma_y \\ \tau_s \end{bmatrix} dz = \sum_{k=1}^{n} \left\{ \begin{bmatrix} Q_{xx} & Q_{xy} & Q_{xs} \\ Q_{yx} & Q_{yy} & Q_{ys} \\ Q_{sx} & Q_{sy} & Q_{ss} \end{bmatrix}_k \begin{bmatrix} \varepsilon_x^0 \\ \varepsilon_y^0 \\ \gamma_s^0 \end{bmatrix} \int_{h_{k-1}}^{h_k} dz + \begin{bmatrix} Q_{xx} & Q_{xy} & Q_{xs} \\ Q_{yx} & Q_{yy} & Q_{ys} \\ Q_{sx} & Q_{sy} & Q_{ss} \end{bmatrix}_k \begin{bmatrix} \kappa_x \\ \kappa_y \\ \kappa_s \end{bmatrix} \int_{h_{k-1}}^{h_k} z dz \right\}$$

$$\begin{bmatrix} M_x \\ M_y \\ M_s \end{bmatrix} = \sum_{k=1}^{n} \int_{h_{k-1}}^{h_k} \begin{bmatrix} \sigma_x \\ \sigma_y \\ \tau_s \end{bmatrix} z dz = \sum_{k=1}^{n} \left\{ \begin{bmatrix} Q_{xx} & Q_{xy} & Q_{xs} \\ Q_{yx} & Q_{yy} & Q_{ys} \\ Q_{sx} & Q_{sy} & Q_{ss} \end{bmatrix}_k \begin{bmatrix} \varepsilon_x^0 \\ \varepsilon_y^0 \\ \gamma_s^0 \end{bmatrix} \int_{h_{k-1}}^{h_k} z dz + \begin{bmatrix} Q_{xx} & Q_{xy} & Q_{xs} \\ Q_{yx} & Q_{yy} & Q_{ys} \\ Q_{sx} & Q_{sy} & Q_{ss} \end{bmatrix}_k \begin{bmatrix} \kappa_x \\ \kappa_y \\ \kappa_s \end{bmatrix} \int_{h_{k-1}}^{h_k} z^2 dz \right\} \tag{4.17}$$

The equation (4.16) can be expressed in the reduced form as equation (4.18)

$$[N]_{x,y} = \{\sum_{k=1}^{n} [Q]^k{}_{x,y} \int_{h_{k-1}}^{h_k} dz\} [\varepsilon^0]_{x,y} + \{\sum_{k=1}^{n} [Q]^k{}_{x,y} \int_{h_{k-1}}^{h_k} z dz\} [\kappa^0]_{x,y}$$
$$= \{\sum_{k=1}^{n} [Q]^k{}_{x,y} (h_k - h_{k-1})\} [\varepsilon^0]_{x,y} + \{\frac{1}{2} \sum_{k=1}^{n} [Q]^k{}_{x,y} (h_k{}^2 - h_{k-1}{}^2)\} [\kappa^0]_{x,y} = [A]_{x,y} [\varepsilon^0]_{x,y} + [B]_{x,y} [\kappa^0]_{x,y}$$

$$[M]_{x,y} = \{\frac{1}{2} \sum_{k=1}^{n} [Q]^k{}_{x,y} (h_k{}^2 - h_{k-1}{}^2)\} [\varepsilon^0]_{x,y} + \{\frac{1}{3} \sum_{k=1}^{n} [Q]^k{}_{x,y} (h_k{}^3 - h_{k-1}{}^3)\} [\kappa^0]_{x,y} = [B]_{x,y} [\varepsilon^0]_{x,y} + [D]_{x,y} [\kappa^0]_{x,y}$$

(4.18)

where

A_{ij} B_{ij} and D_{ij} are extensional stiffness relating in plane loads to strains, coupling stiffness or in plane/flexure coupling laminate moduli, relating in plane loads to curvatures and moments to in plane strains and bending or flexural laminate stiffness relating moments to curvatures respectively.

$$A_{ij} = \sum_{k=1}^{n} Q_{ij}{}^{k}(h_k - h_{k-1})$$
$$B_{ij} = \frac{1}{2}\sum_{k=1}^{n} Q_{ij}{}^{k}(h_k{}^{2} - h_{k-1}{}^{2}) \qquad (4.19)$$
$$D_{ij} = \frac{1}{3}\sum_{k=1}^{n} Q_{ij}{}^{k}(h_k{}^{3} - h_{k-1}{}^{3})$$

For symmetric laminates with specially orthotropic layers case and k^{th} layer is oriented with its principal 1-direction along the x-axis then

$$Q_{xx}{}^{k} = Q_{11}{}^{k} = \frac{E_{11}{}^{k}}{1-\upsilon_{12}{}^{k}\upsilon_{21}{}^{k}}$$
$$Q_{xy}{}^{k} = Q_{12}{}^{k} = \frac{\upsilon_{21}{}^{k}E_{11}{}^{k}}{1-\upsilon_{12}{}^{k}\upsilon_{21}{}^{k}}$$
$$Q_{yy}{}^{k} = Q_{22}{}^{k} = \frac{E_{22}{}^{k}}{1-\upsilon_{12}{}^{k}\upsilon_{21}{}^{k}} \qquad (4.20)$$
$$Q_{xs}{}^{k} = Q_{16}{}^{k} = 0$$
$$Q_{ys}{}^{k} = Q_{26}{}^{k} = 0$$
$$Q_{ss}{}^{k} = Q_{66}{}^{k} = G_{12}{}^{k}$$

Finally the resultant force and moment equation becomes

$$\begin{bmatrix} N_x \\ N_y \\ N_s \end{bmatrix} = \begin{bmatrix} A_{xx} & A_{xy} & 0 \\ A_{yx} & A_{yy} & 0 \\ 0 & 0 & A_{ss} \end{bmatrix} \begin{bmatrix} \varepsilon_x^{\,0} \\ \varepsilon_y^{\,0} \\ \gamma_s^{\,0} \end{bmatrix}$$

$$\begin{bmatrix} M_x \\ M_y \\ M_s \end{bmatrix} = \begin{bmatrix} D_{xx} & D_{xy} & 0 \\ D_{yx} & D_{yy} & 0 \\ 0 & 0 & D_{ss} \end{bmatrix} \begin{bmatrix} \kappa_x^{\,0} \\ \kappa_y^{\,0} \\ \kappa_s^{\,0} \end{bmatrix} \tag{4.21}$$

We can apply this composite analysis into the sandwich structure analysis by simply define lamina 1 as the lower face, lamina 2 as the core and lamina 3 as the top face like Figure 4.57.

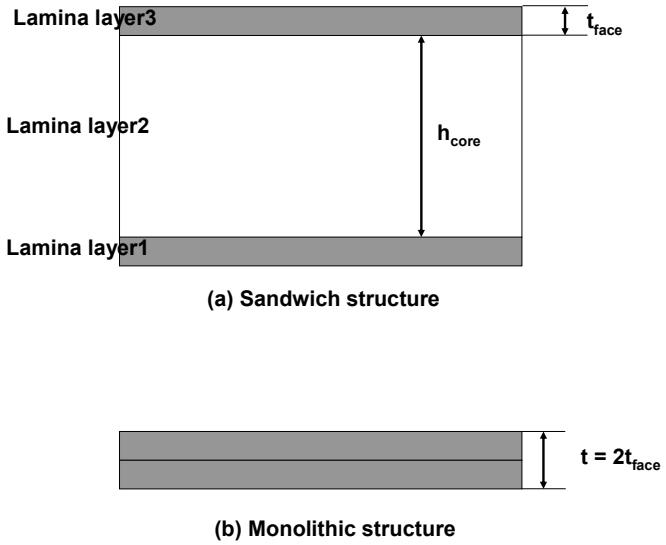

Figure 4.57. (a) Cross sectional shape of sandwich structure and (b) monolithic structure.

In this case, the extensional stiffness matrix [A] and bending stiffness matrix [D] become

$$A_{ij} = \sum_{k=1}^{3} Q_{ij}{}^{k}(h_k - h_{k-1}) = (Q_{ij})_{face}[-\frac{h_c}{2} - (-\frac{h_c}{2} - t_{face})] + (Q_{ij})_{core}[\frac{h_c}{2} - (-\frac{h_c}{2})] + (Q_{ij})_{face}[(\frac{h_c}{2} + t_{face}) - (\frac{h_c}{2})]$$

$$= (Q_{ij})_{face}(2t_{face}) + (Q_{ij})_{core}(h_c)$$

$$D_{ij} = \frac{1}{3}\sum_{k=1}^{3} Q_{ij}{}^{k}(h_k{}^{3} - h_{k-1}{}^{3})$$

$$= \frac{1}{3}(Q_{ij})_{face}[-(\frac{h_c}{2})^3 - (-\frac{h_c}{2} - t_{face})^3] + \frac{1}{3}(Q_{ij})_{core}[(\frac{h_c}{2})^3 - (-\frac{h_c}{2})^3] + \frac{1}{3}(Q_{ij})_{face}[(\frac{h_c}{2} + t_{face})^3 - (\frac{h_c}{2})^3] \tag{4.22}$$

when we assume the material axis and global axis are the same and use equation (4.10) then

$$A_{ij} = \frac{E_{ij(face)}(2t_{face})}{(1 - \upsilon_{12(face)}\upsilon_{21(face)})} + \frac{E_{ij(core)}(h_c)}{(1 - \upsilon_{12(core)}\upsilon_{21(core)})} \tag{4.23}$$

$$D_{ij} = \frac{1}{3}\{\frac{2E_{ij(face)}}{(1 - \upsilon_{ij(face)}\upsilon_{ji(face)}}[(\frac{3}{4})h_{core}{}^{2}t_{face} + \frac{3}{2}h_{core}t_{face}{}^{2} + t_{face}{}^{3}] + \frac{E_{ij(core)}}{(1 - \upsilon_{ij(core)}\upsilon_{ji(core)})}(\frac{h_c}{4})^3\} \tag{4.24}$$

Assume $E_{core} << E_{face}$ and $h_{core} >> t_{face}$ then

$$[A_{ij}] = \begin{bmatrix} \frac{2E_{11(face)}t_{face}}{(1 - \upsilon_{12(face)}\upsilon_{21(face)})} & \frac{2\upsilon_{21(face)}E_{11(face)}t_{face}}{(1 - \upsilon_{12(face)}\upsilon_{21(face)})} & 0 \\ \frac{2\upsilon_{21(face)}E_{11(face)}t_{face}}{(1 - \upsilon_{12(face)}\upsilon_{21(face)})} & \frac{2E_{22(face)}t_{face}}{(1 - \upsilon_{12(face)}\upsilon_{21(face)})} & 0 \\ 0 & 0 & 2G_{12(face)}t_{face} \end{bmatrix} \tag{4.25}$$

$$[D_{ij}] = \begin{bmatrix} \frac{E_{11(face)}(h_{core})^2 t_{face}}{2(1 - \upsilon_{12(face)}\upsilon_{21(face)})} & \frac{E_{11(face)}\upsilon_{21(face)}(h_{core})^2 t_{face}}{2(1 - \upsilon_{12(face)}\upsilon_{21(face)})} & 0 \\ \frac{E_{11(face)}\upsilon_{21(face)}(h_{core})^2 t_{face}}{2(1 - \upsilon_{12(face)}\upsilon_{21(face)})} & \frac{E_{22(face)}(h_{core})^2 t_{face}}{2(1 - \upsilon_{12(face)}\upsilon_{21(face)})} & 0 \\ 0 & 0 & \frac{G_{12(face)}(h_{core})^2 t_{face}}{2} \end{bmatrix}$$

(4.26)

If we compare the flexural stiffness per unit width, D between sandwich structure and monolithic structure, which has approximately same weight as sandwich structure then

$$D_{monlithic} = \frac{E_{face}(2t_{face})^3}{12(1-\upsilon_{face}{}^2)} = \frac{2E_{face}t_{face}{}^3}{3(1-\upsilon_{face}{}^2)} \tag{4.27}$$

and the bending stiffness ($D_{sandwich}$) of the sandwich structure (assuming face material is a homogeneous material, which used in monolithic structure) is

$$D_{sandwich} = \frac{E_{face}(t_{face})(h_{core})^2}{2(1-\upsilon_{face}{}^2)} \tag{4.28}$$

Therefore the ratio $D_{sandwich}$ to $D_{monolithic}$ is

$$\frac{D_{sandwich}}{D_{monolithic}} = \frac{3}{4}(\frac{h_c}{t_f})^2 \tag{4.29}$$

When we apply equation (4.29) into our case i.e., thickness of face (t_{face}) = 1.5 mm and height of core (h_{core}) = 7 mm, the flexural stiffness of modified HG-MAC (sandwich structure) will be 16 times stiffer than monocoque structure, which is made of 3 mm (2 t_{face}) thickness face material.

Also when we use 1.5 mm graphite/epoxy system in the face material (HG-MAC V12) then the bending stiffness (D_{11}) of this structure is almost same as 9 mm thickness steel plate and we can expect ~ 93 % weight saving from this sandwich HG-MAC structure. Table 4.7 compares the bending stiffness of various face material attached sandwich structure cases. Figure 4.58 exhibits the specific bending stiffness and tan δ of the sandwich and monolithic structures. Also 4.59 exhibits the weight comparison of

various structural materials to get the same bending stiffness as HG-MAC V12. (graphite/epoxy skin HG-MAC) According to Figure 4.6.13, specific bending stiffness improved the stiffness of the carbon/epoxy+elastomer panels. However the damping does not change. HG MAC sandwich panels are stiff in bending with high inherent damping that is two orders of magnitude higher than standard composites laminated with a plain elastomer sheet.

Table. 4.7. Flexural stiffness comparison between sandwich structure and monolithic structure.

Face material	$D_{(11)sandwich}$ (Nm/m)	$D_{monolithic}$ (Nm/m)	Density (g/cm^3)	Classifications (Version)
Rigid polyurethane	68.0	4.16	1.14	V2
Steel	8359	511.81	7.85	V3
Aluminum	2845	174.22	2.71	V4
Al 2024 T4	2985	182.81	2.77	V5
Nylon6	93	5.90	1.17	V6
PS	103	6.31	1.05	V7
PMMA	131	8.04	1.19	V8
E-glass/epoxy	1457	89.25	2.10	V9
Kevlar/epoxy	3219	197.09	1.38	V10
Carbon/epoxy	6540	400.41	1.60	V11
Graphite/epoxy	10829	663.02	1.59	V12

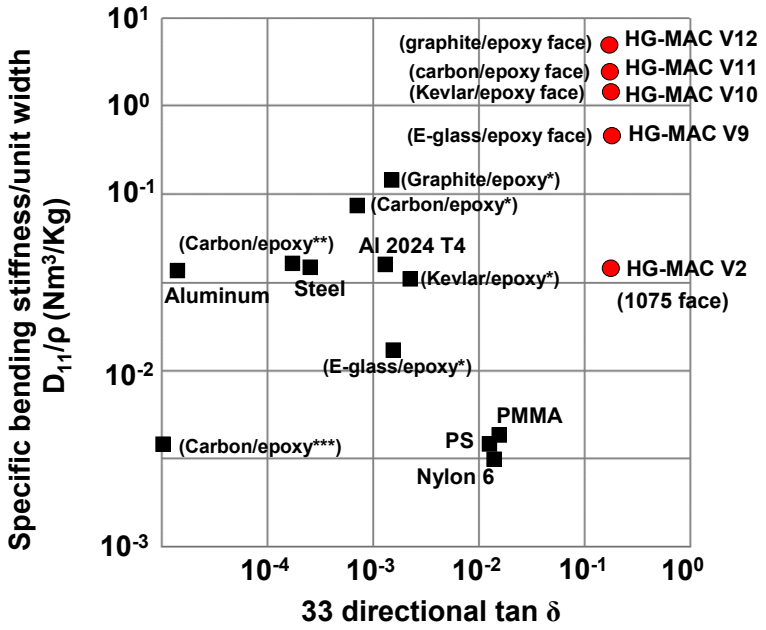

Figure 4.58. Specific bending stiffness (D_{11}/ρ) of various structural materials.

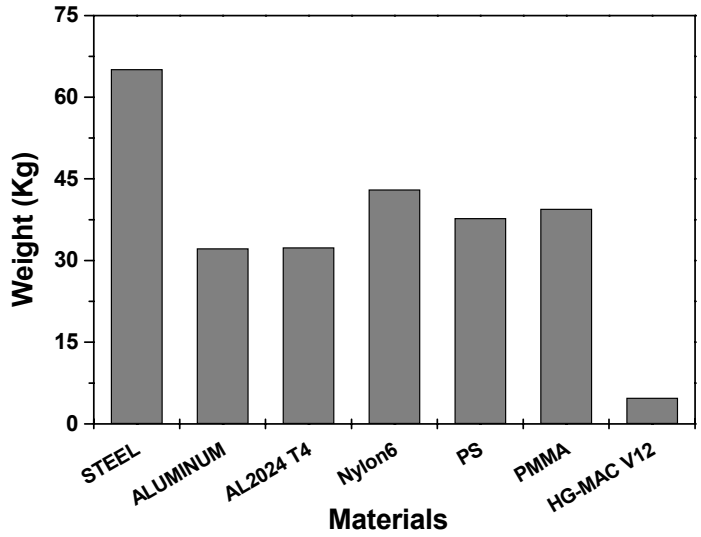

Figure 4.59. Required weight of various structural materials to get the same bending stiffness (D_{11}) as HG-MAC V12 (graphite/epoxy skin HG-MAC).

4.6.3. Experimental Damping Characteristics of the Stiffened HG-MAC (Sandwich HG-MAC)

The basic assumption of the previous stiffening analysis was that the damping property (tan δ) will not be changed as long as the inner-channel of the HG machine is properly closed. In this sub section, this basic assumption is verified by the dynamic testing of the rigid polyurethane face attached sandwich HG-MAC (HG-MAC V2).

Figure 4.60 (a) and (b) display the schematic drawing of fabrication method of HG-MAC V2 and its real cross sectional shape respectively.

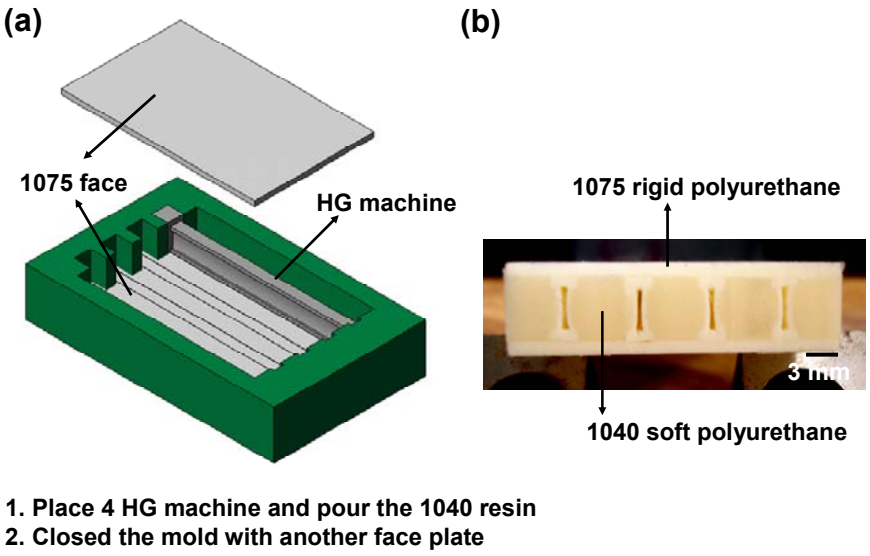

Figure 4.60. (a) Schematic drawing of sandwich HG-MAC fabrication procedure and (b) 0.18 $V_{machine}$ reinforced sandwich HG-MAC (HG-MAC V2).

Also Figure 4.61 displays the compressive stress strain curve of HG-MAC V2 through static test. The measured 33 directional stiffness (E_{33}) was ~ 82 MPa and compared with that of previous HG-MAC (HG-MAC V1) case (~16 MPa), the sandwich structure HG-MAC shows ~ 413 % stiffer characteristics. Also the compressive strain for full gap closure in the HG-MAC V2 (rigid PU skin), the required strain for gap closing was only ~ 4.5 % but in the HG-MAC V1 (default HG-MAC), the full gap closure was occurred at ~ 11 %. From these results, we can claim that the sandwich HG-MAC shows better performance than previous HG-MAC.

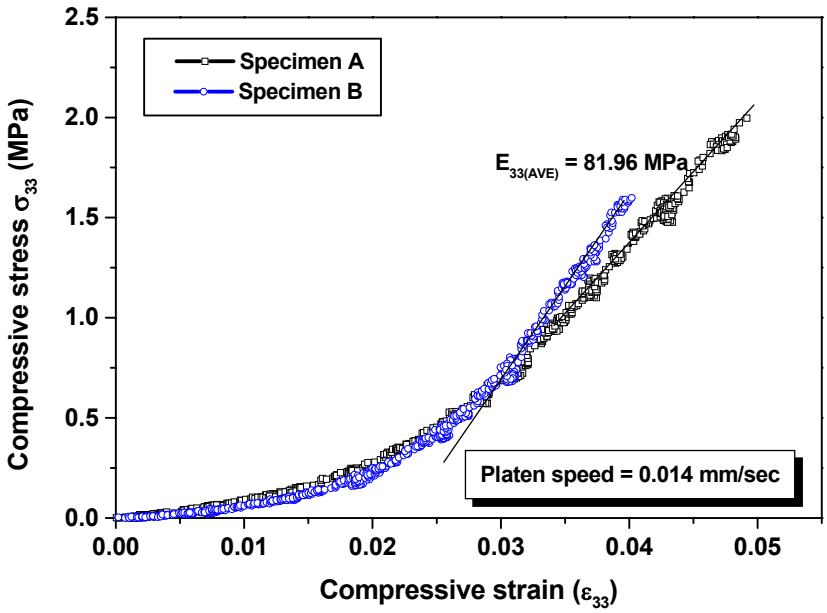

Figure 4.61. Compressive stress-strain curves of sandwich HG-MAC (HG-MAC V2) by static testing.

To see the dynamic properties of HG-MAC V2, same load-controlled dynamic test was performed and Figure 4.62 shows the dynamic testing results. As in the previous cases, the measured tan δ values increase as the frequency increase from 10 to 100 Hz and again, fluid effect is very small due to the large dead volume in the inner-channel, insufficient fluid viscosity, and insufficient strain rate.

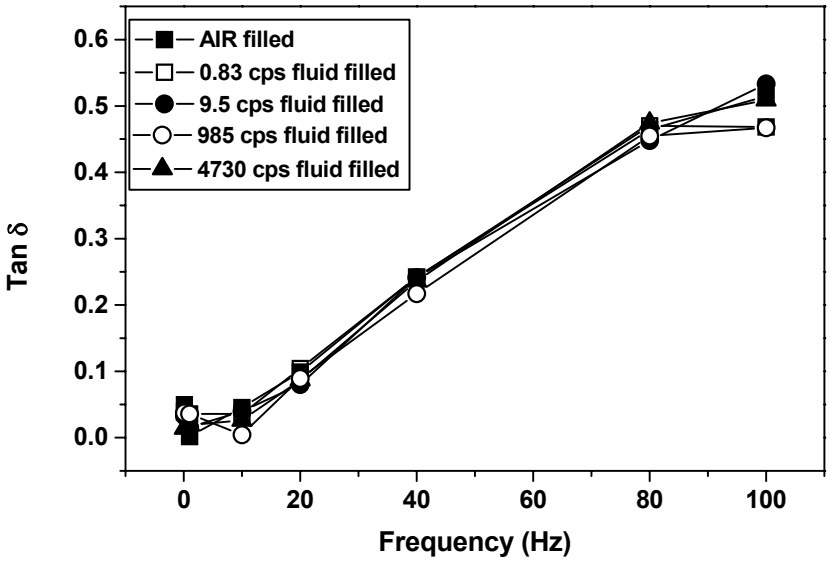

Figure 4.62. Dynamic test results of sandwich HG-MAC. (HG-MAC V2)

Figure 4.63 (a) and (b) compares the tan δ values of air-filled and 4730 cps fluid filled HG-MAC V1 and HG-MAC V2. From these charts we observe that the damping property of the sandwich structure HG-MAC is almost same as the previous cases. Therefore, we can claim that the transverse directional damping of the HG-MAC structure is mainly depends on the gap closure.

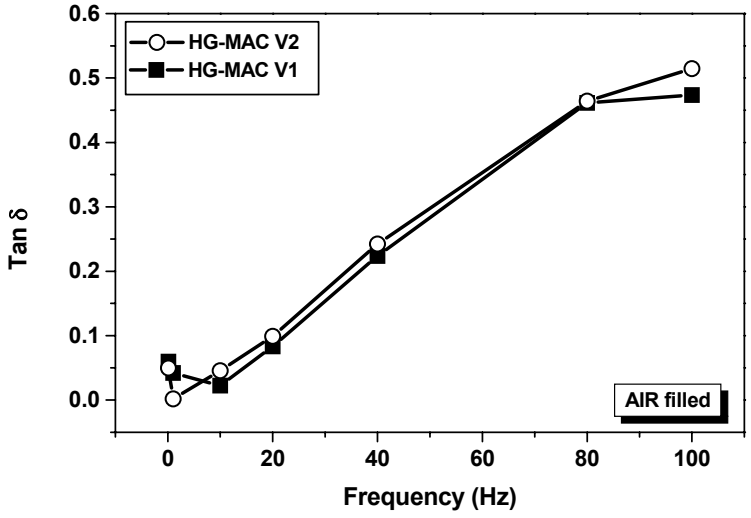

(a)

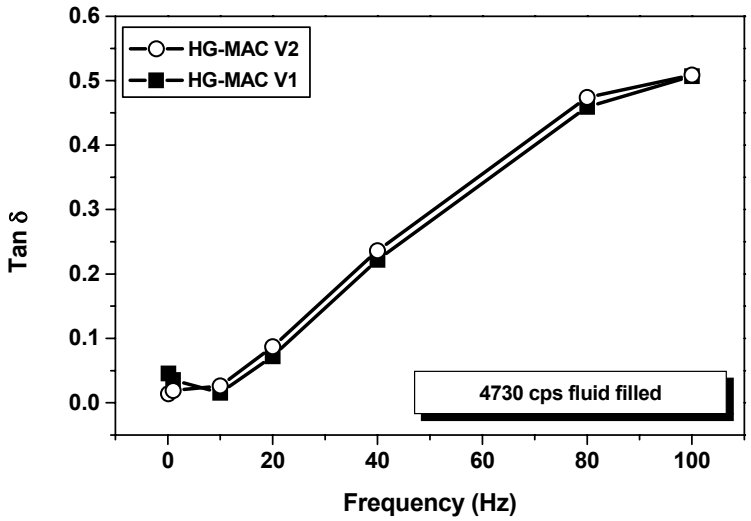

(b)

Figure 4.63. Tan δ value comparisons between HG-MAC V1 and HG-MAC V2 of (a) air filled condition and (b) 4730 cps fluid filled condition.

Figure 4.64 exhibits the loss modulus (E") of matrix, default HG-MAC (V1) and rigid polyurethane skin sandwich HG-MAC (V2). Since the storage modulus of the sandwich structure is much higher than matrix and default HG-MAC, the resulting loss modulus, which is defined as the product of storage modulus and tan δ is also high and this means, the stiffer structure (HG-MAC V2) can dissipate more energy than soft structure.

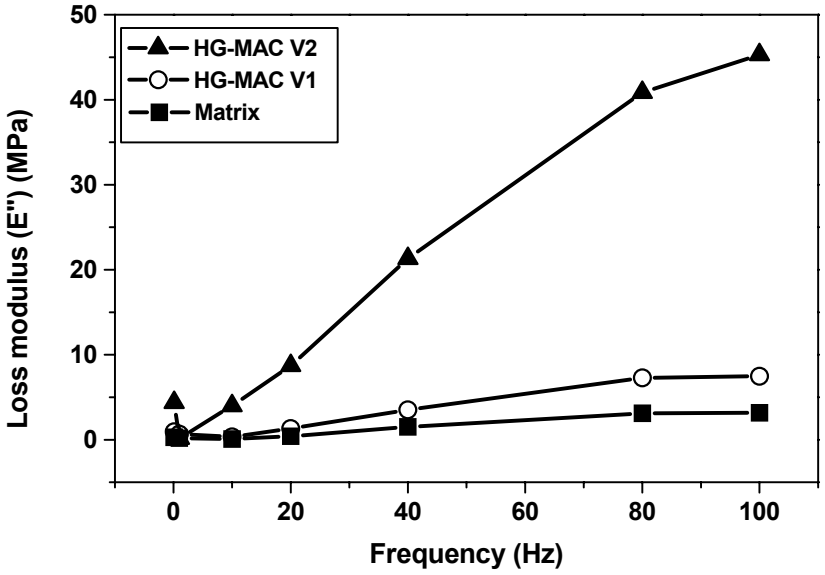

Figure 4.64. Loss modulus comparison between soft polyurethane matrix, default HG-MAC (V1) and sandwich HG-MAC (V2), which has rigid polyurethane skin.

4.7. Summary

Through the experimental testing and numerical analysis following information was obtained.

Through the load-controlled dynamic testing, the tan δ values were measured in the frequency of 0.1 to 100 Hz ranges and the calculated tan δ was increased as the testing frequency increases.

The fluid effect on damping is negligible because of several reasons such as the dead volume of the inner channel is too big, not sufficient fluid viscosity and strain rate.

The HG-MAC shows enhanced damping properties when compare with matrix at the frequency of 0.1 to 40 Hz ranges and also exhibits ~ 130 % higher 33 directional stiffness than matrix, consequently, the loss modulus (E") is also enhanced.

The optimum performance of the HG-MAC was obtained when the Poisson's ratio of the matrix was 0.49 and there are relations between the volume fraction of the machine and the stiffness ratio ($E_{machine}/E_{matrix}$) between machine and matrix.

The gap closure characteristics of a solitary cell and an infinite array were different. For the solitary cell case, increasing the volume fraction of the machine cause increases the gap closure. For the infinite array case, increasing the volume fraction of the machine cause decreases the gap closure and the optimum performance was obtained when the volume fraction of the HG machine was between 0.2 and 0.3.

The HG-MAC can be further stiffened (~ 500 %) by making the previous HG-MAC structure to the sandwich structure (replace the upper and lower portions of the current HG-MAC with stiffer material) without losing current high damping. Also this modified sandwich structure shows high specific bending stiffness (D_{11}) due to the basic characteristics of sandwich structure.

CHAPTER V

CONCLUSIONS, APPLICATIONS, AND FUTURE WORK

This final chapter presents the conclusions obtained from careful examination of the analysis and experiments, some possible applications of this passive damping technology, and suggested future work for better understanding, design, and research in advanced versions of this technology.

5.1. Conclusions

The advanced composite structure for multifunctional properties were successfully fabricated and tested. From this study following conclusions can be obtained through experiments and numerical analysis.

By embedding the specially designed machine (HG machine) into the soft polyurethane matrix, we could fabricate the advanced composite structure, which had about 130 % higher stiffness and better damping property than soft matrix.

This means that the structure can dissipate more energy than soft polyurethane matrix because the loss modulus (E"), of the advanced composite structure is also higher than matrix.

Also the default structure could be further stiffened by converting the default HG-MAC into the sandwich structure, which had stiff face skin. The damping property of this modified HG MAC structure was almost same as the default HG-MAC and this implies that the structure can be stiffened without loosing damping unlike the damping of material decrease as stiffened.

Because this modified sandwich HG-MAC was about 6 times stiffer than the default HG-MAC and since the damping of this structure was not decreased, the energy dissipation from this structure was much higher than soft polyurethane matrix.

Through the numerical analysis result, we found that an optimum machine volume fraction exist both default and sandwich HG-MAC and lower or higher machine volume fraction cause worse the performance of the HG-MAC system.

Here are the detailed overall summaries of this study.

Through the load-controlled dynamic testing of the elastomer like matrix and the HG-MAC, the tan δ values were measured in the frequency ranges of 0.1 to 100 Hz and the calculated tan δ value of the HG-MAC showed noticeable improvement in the frequency range of 1 ~ 40 Hz. That is when the HG-MAC was filled with 0.83 and 9.5 cps fluid, the measured tan δ value of the HG-MAC showed maximum 74 % and 75 % increment respectively at 1 Hz and in the cases of filled fluid viscosity varies from air, 985, and 4730 cps, the calculated tan δ value of the HG-MAC exhibited 89 %, 117 % and 31 % increment respectively at the frequency of 10 Hz.

Also the HG-MAC showed ~ 130 % higher transverse directional compressive stiffness than matrix and consequently the loss modulus (E") was also enhanced.

However, the fluid effect on damping was small because of several suspected reasons such as the dead volume of the inner channel was too big, the filled fluid viscosity and the strain rate was not high enough.

The optimum performance of the HG-MAC was obtained when the Poisson's ratio of the matrix was 0.49 and there are corelations between the volume fraction of the machine and the stiffness ratio ($E_{machine}/E_{matrix}$).

The gap closure characteristics of the solitary cell and infinite array were different and for the solitary cell case, increasing the volume fraction of the machine cause increasing the performance but for the infinite array case, increasing the volume fraction of the machine cause decreasing the gap closure due to the machine and matrix interaction and the optimum performance was obtained when the volume fraction of the HG machine was between 0.15 and 0.2.

The HG-MAC can be further stiffened by making the previous HG-MAC structure to the sandwich structure (replace the upper and lower portions of the current HG-MAC with stiffer material) and the enhanced transverse directional stiffness was ~ 1100 % compared with that of matrix.

This modified structure prefer high $E_{machine}/E_{matrix}$ ratio because the gap closure was occurred by the direct compression from the stiff surface skin. The optimum performance of this modified structure was obtained when the volume fraction of the machine was 0.3.

The measured tan δ values of this modified HG-MAC structure was almost same as previous HG-MAC and this means the HG-MAC structure can be stiffened without losing current high damping.

Also this modified sandwich structure shows high specific bending stiffness (D_{11}) due to the basic advantage of sandwich structure.

5.2. Applications

From the previous analysis results, the possible application areas of the HG-MAC can be outlined as in Table 5.1. Also, Figure 5.1 displays the required structural properties of automotive floor panel and commercial air plane skin structures.

Table 5.1. Structural properties comparison between metals (monolithic), rubber constrained sandwich structure, which has metal skins, composite materials and HG-MAC system.

	Required property		
	Damping	**Bending stiffness**	**Compressive stiffness**
Metals (monolithic)	**Poor**	**Good**	**Good**
Rubber constrained sandwich structure	**Good**	**Poor**	**Poor**
Honeycomb core sandwich structure	**Poor**	**Good**	**Good**
Composite materials	**Poor**	**Good**	**Good**
HG-MAC system	**Good**	**Good**	**Good**

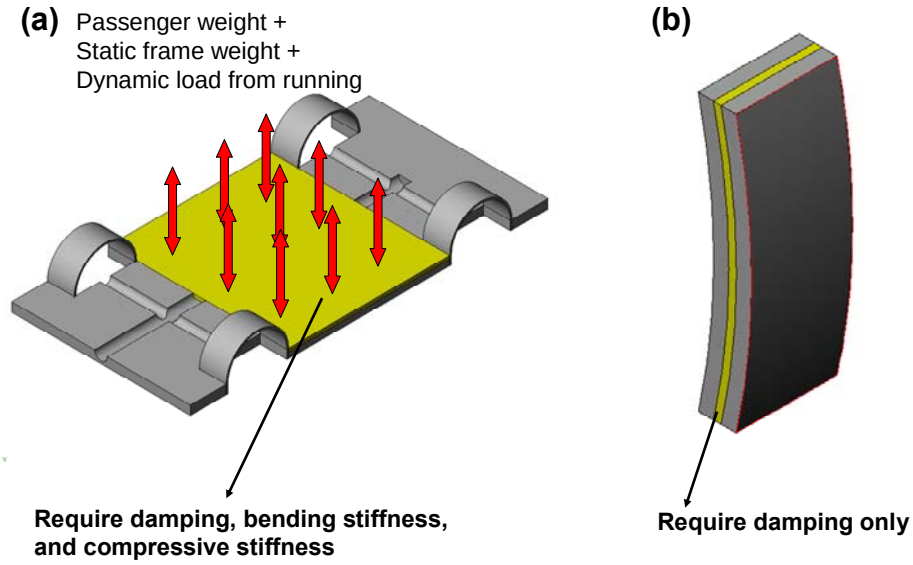

Figure 5.1. Expected structural requirements on (a) automobile and (b) airplane skin structures.

According to Table 5.1, the HG-MAC structure shows good structural properties in both damping and stiffness.

However in terms of fabrication cost, the HG-MAC structure does not have advantage over rubber constrained sandwich structure in damping applications also does not have advantage over other metals, rubber constrained sandwich structure and composite materials in bending stiffness. But when we consider multifunctional structural properties; complex structural applications i.e., require damping, bending stiffness, and compressive stiffness, only the HG-MAC system has all those properties at the same time. And since the structural properties of the HG-MAC can be tailored easily

by changing the volume fraction of machine, modifying the constituent material properties and stacking sequence of the lamina, this new composite structure has big advantage on complex structural applications. Also when we replace the machine material with aluminum in case of impact damage like Figure 5.2, i.e., neglect damping effect from cyclic loading, this HG-MAC structure can be applied in the automobile body, because this HG-MAC structure can absorb large amount of impact energy through the bending of the machine walls.

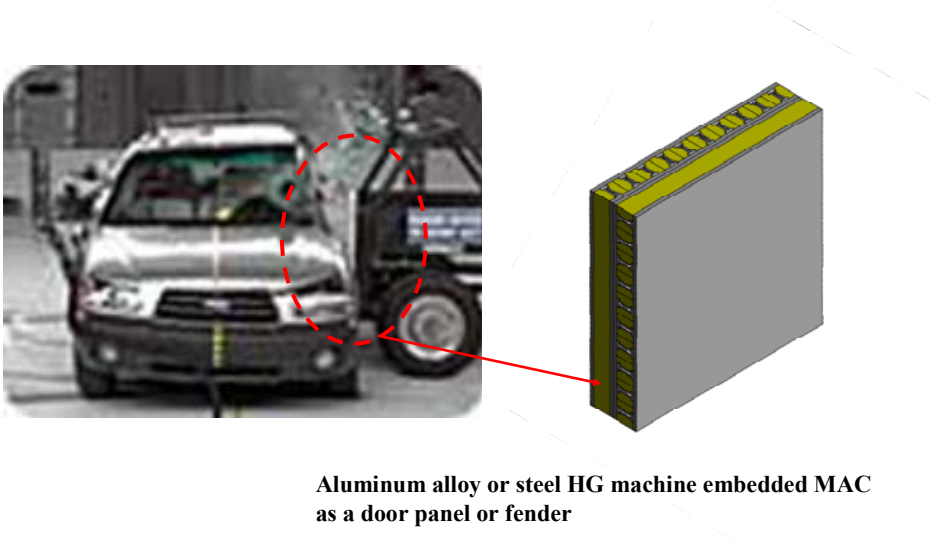

Figure 5.2. Possible application of HG-MAC system on the impact damage.

Another possible application of this HG-MAC structure is for protection of the building structures from earthquake. Since the wave of earth quake is sometimes horizontal and at this situation we need certain modification of current HG-MAC structure. In other words to convert shear input to compressive output; to initiate the working mechanism of HG-MAC, we have to combine Z-machine [1] with current HG-

machine like Figure 5.3 and by constructing part of the foundation of the building structure with this advanced structure, certain amount of earthquake energy might be absorbed.

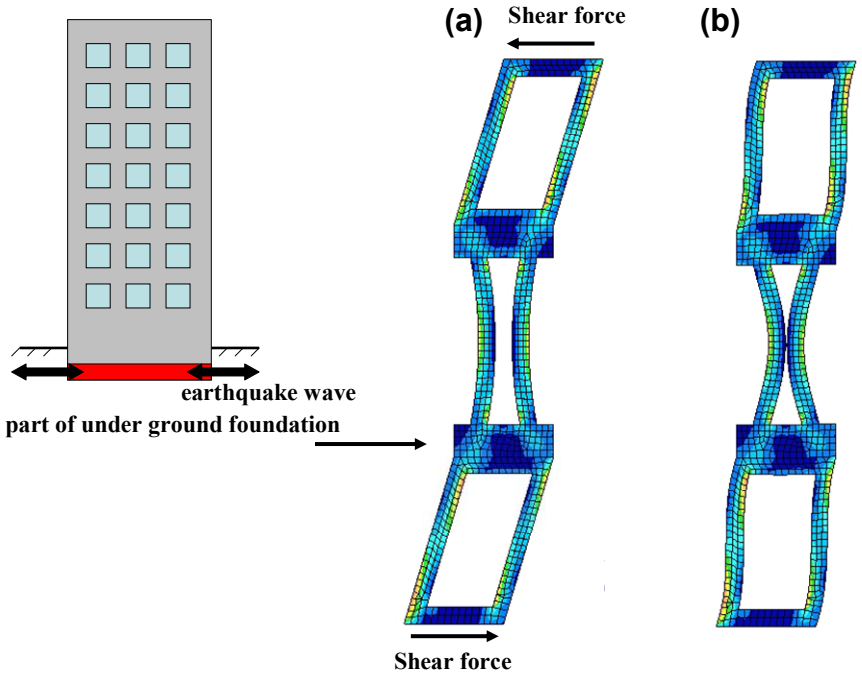

Figure 5.3. Combination of Z-machine and HG-machine for converting shear stress input to compressive stress output.

5.3. Future Work

In this study, the basic deformation mechanism and concept of the lamina shape HG-MAC system was explored.

To extend this structural concept more applicable, this structure should be made into the laminate structure like other conventional fiber-reinforced composite and the laminate HG-MAC structure should be analyzed. To achieve these goals, the stiffness

[C] or compliance [S] matrix for each lamina HG-MAC structure should be constructed first through an homogenization method. Also the effect of stacking sequence of individual lamina HG-MAC on damping and other mechanical properties should be examined through experiments and analytical approaches. The viscous fluid effect on damping as well as viscous fluid flow behavior in terms of external loading and geometry of the inner-channel should be characterized for the better understanding of viscous damping.

The most important work should be carried in the future will be find out the optimum composite structure and constituent material properties by combination of this study results and those of previous study [54] for the optimum multifunctional composite structure.

REFERENCES

[1] Hawkins GF. Augmenting the mechanical properties of materials by embedding simple machines. J. Advanced Materials 2002;34(3):16-20.

[2] Chandra R, Singh SP, Gupta K. Damping studies in fiber-reinforced composite- a review. Composite Structures 1999;46:41-51.

[3] NASA Practice No. PD-ED-1259 Acoustic noise requirement. 1996;1-6, May.

[4] Scharton TD. Vibration and acoustic testing of spacecraft. Sound and Vibration 2002; 1-5.

[5] Saravanos DA, Chamis CC. Integrated mechanics for the passive damping of polymer-matrix composite and composite structures. Mechanics and Mechanisms of Material Damping, ASTM STP 1169 1992;Philadelphia: 471-489.

[6] Leo DJ, Anderson EH. Vibroacoustic modeling of a launch vehicle payload fairing for active acoustic control. AIAA-98-2086 1997; 1-12.

[7] Rivin EI. Stiffness and damping in mechanical design. New York: Marcel Decker, Inc; 1999.

[8] Jones DIG. Handbook of viscoelastic vibration damping. New York: John Wiley & Sons. Ltd; 2001.

[9] Lazan B. Damping of materials and members in structural mechanics. New York: Pergamon Press; 1968.

[10] Johnson CD. Design of passive damping system. Trans ASME. 1995;117(B).

[11] Daniel IM, Ishai O. Engineering mechanics of composite materials, New York: Oxford University Press, Inc; 1994.

[12] Ferry JD. Viscoelastic properties of polymers. 3rd edition. New York: John Wiley & Sons, Inc; 1980.

[13] Rodriguez F. Principles of polymer systems. 2nd edition. New York: McGraw-Hill; 1982.

[14] McCrum NG, Buckley CP, Bucknall CB. Principles of polymer engineering. 2nd edition. New York: Oxford University Press; 1997.

[15] Rosen SL. Fundamental principles of polymeric materials. 2nd edition. New York: John Wiley & Sons, Inc; 1993.

[16] Cremer L, Heckl M, Ungur EE. The structure-borne sound; Structural vibrations and sound radiation at audio frequencies. Berlin: Springer-Verlag; 1973.

[17] Nashif AD, Jones DIG, Henderson JP. Vibration damping. New York: John Wiley & Sons, Inc; 1985.

[18] Lakes RL. High damping composite materials: Effect of structural hierarchy. Journal of Composite Materials. 2002;36 (3): 287-297.

[19] Crema LB, Castellani A, Drago U. Damping characteristics of fabric and laminated Kevlar composites. Composites. 1989;20: 593-595.

[20] Gibson RF, Hwanf SJ, Kwak H. Micromechanical modeling of damping in composites including interphase effect. Proceedings of the 36th International SAMPE Symposium, Society for the Advancement of Material and Process Engineering, Covina, Italy 1, 592-606, 1991.

[21] Chinquin J, Chabert B, Chauchard J, Morel E, Totignon JP. Characterization of thermoplastic (polyamide) reinforced with unidirectional glass fibers, matrix

additives and fibers surface treatment influence on mechanical and viscoelastic properties. Composite 1990; 21:141-147.

[22] Chandra R. A study of dynamic behavior of fiber-reinforced composites. Proceedings of a workshop on solid mechanics, University of Roorkee, India, 59-63, 1985.

[23] Kenny JM, Marchetti M. Elasto-plastic behavior of thermoplastic composite laminates under cyclic loading. Composite Structures 1995;32: 375-382.

[24] Curtis DC, Moore DR, Slater B, Zahlan N. Fatigue testing of multiangle laminates of CF/PEEK. Composites 1988;19: 446-455.

[25] Ni RG, Adams RD. A rational method for obtaining the dynamic mechanical properties of laminae for predicting the stiffness and damping of laminated plates and beams. Composite 1984;15 (3): 193-199.

[26] Adams RD. Damping properties analysis of composites. Engineered Material Handbook. ASM. 1. 1987; 206-217.

[27] Jones DIG. Handbook of viscoelastic vibration damping. New York: John Wiley & Sons Ltd; 2001.

[28] Ross D, Ungar EE, Kerwin EM. Damping of plate flexural vibrations by means of viscoelastic laminate. Structural damping, New York: ASME 1959; 49-88.

[29] Mead DJ. The effect of certain damping treatments on the response of idealized aeroplane structures exited by noise. AFML-TR-65-284, WPAFB, 1965.

[30] Preumont A. Vibration control of active structures, An introduction. 2nd edition. Portland: Kluwer Academic Publishers; 2002.

[31] Timoshenko SP, Goodier JN. Theory of elasticity. 3rd edition. New York: McGraw-Hill; 1970.

[32] Budynas RG. Advanced strength and applied stress analysis. 2nd edition. New York: McGraw-Hill; 1999

[33] Gere JM. Mechanics of materials. 5th edition. Belmont CA: Brooks/Cole; 2000.

[34] Slaughter WS. The linearized theory of elasticity. Boston: Birkhäuser; 2001.

[35] Lempriere BM. Poisson's ratio in orthotropic materials. AIAA, 1968;8(11): 2226-2227.

[36] Gibson LJ, Ashby MF, Schajer GS, Robertson CI. The mechanics of two dimensional cellular solids. 1982;Proc. R. Soc. Lond. A382: 25-42.

[37] Lakes RS. Foam structure with a negative Poisson's ratio. Science 1987;235: 1038-1040.

[38] Lakes RS. No contractile obligations. Nature 1992;358: 713-714.

[39] Lakes RS. Foam materials with a negative Poisson's ratio. Development in Mechanics 1987;14:758-763.

[40] Lakes RS. A broader view of membranes. Nature 2001;414: 503-504.

[41] Lakes RS, Prall D. Properties of a chiral honeycomb with a Poisson's ratio of -1. Int. J. Mech. Sci 1997;39(3): 305-314.

[42] Warren TL. Negative Poisson's ratio in a transversely isotropic foam structure. J. Appl. Phys. 1990;67(12): 7591-7594.

[43] Alderson KL, Evans KE. The fabrication of microporous polyethylene having a negative Poisson's ratio. Polymer 1992;33(20) 4435-4438.

[44] Caddock BD., Evans KE. Tensile network microstructures exhibiting negative Poisson's ratios. J. Phys. D., Appl. Phys. 1989;22: 1870-1876.

[45] Caddock BD, Evans KE. Microporous materials with negative Poisson's ratios I Microstructure and mechanical properties. J. Phys. D., Appl. Phys. 1989;22: 1877-1882.

[46] Caddock BD., Evans KE. Microporous materials with negative Poisson's ratios II Mechanisms and interpretation. J. Phys. D., Appl. Phys. 1989;22: 1883-1887.

[47] Almgren RF. An isotropic three-dimensional structure with Poisson's ratio = -1. J. Elasticity 1985;15: 427-430.

[48] Glieck J. A perverse creation of science: Anti-rubber. The New York Times 1987: April 14; C8.

[49] Milton G. Composite materials with Poisson's ratios close to -1. J. Mech. Phys. Solids 1992;40: 1105-1137.

[50] Prall D, Lakes RL. Properties of a chiral honeycomb with a Poisson's ratio of -1. International Journal of Mechanical Sciences 1997;39(3):305-314.

[51] Pecullan S, Gibiansky LV, Torquato S. Scale effects on the elastic behavior of periodic and hierarchical two-dimensional composites. Journal of the Mechanics and Physics of Solids 1999;47(7): 1509-1542.

[52] Sigmund O. Tailoring materials with prescribed elastic properties. Mechanics and Materials 1995;20: 351-368.

[53] Sigmund O. Materials with prescribed constitutive parameters: An inverse homogenization problem. International Journal of Solids and Structures

1994;31(17): 2313-2329.

[54] McCutcheon DM. Machine augmented composite materials for damping purpose. M.S. Graduate thesis. Texas A&M University; 2004.

[55] Herakovich CT. Mechanics of fibrous composites. New York: John Wiley and Sons, Inc; 1988.

[56] Broutman LJ, Krock RH. Composite materials. 2nd edition. New York: Academic Press, Inc; 1974.

[57] Garg SK, Svalbonas V, Gurtman GA. Analysis of structural composite materials New York: Marcel Dekker, Inc; 1973.

[58] Jones RM. Mechanics of composite materials. Philadelphia: Taylor & Francis; 1975.

[59] Gibson RF. Dynamic mechanical behavior of fiber-reinforced composites: Measurement and analysis. J. Composite Materials 1976;10: 325-341.

[60] Gibson LJ, Ashby MF. Cellular solids. Structure and properties. 2nd edition. New York: Cambridge University Press; 1997.

[61] Harper CA. Handbook of plastics and elastomers. New York: McGraw-Hill, Inc;1975.

[62] Brodt M, Lakes RL. Composite materials which exhibit high stiffness and high viscoelastic damping. Journal of Composite Materials 1995;29(14):1823-1833.

[63] Calister, WD. Fundamentals of materials science and engineering New York: John Wiley & Sons, Inc; 2001.

[64] Griffin RB. Materials and manufacturing selection and design. Englewood Cliffs, New Jersey: Prentice-Hall, Inc; 2001.

[65] Vinson JR. The behavior of sandwich structures of isotropic and composite materials. Lancaster, Pennsylvania: Technomic Publishing Company, Inc; 1999.

VITA

Jong Hyun Kim was born in Seoul, South Korea. He received his B.S. degree in August 1997 and M.S. degree in August 1999 from the Department of Materials Science and Engineering of Inha University, Inchon, South Korea and received another M.S. degree in 2000 from the Department of Mechanical Engineering at the University of Southern California, Los Angeles, California, U.S.A. He joined Texas A&M University, College Station, Texas to pursue his Ph.D. degree and received Ph.D. degree on August 2005.

Permanent mailing address is:

Kolon Lake Polis II A-1105

Janghang-Dong,

Ilsan-Gu,

Kyungido, South Korea.

e-mail address:

g9721021@hotmail.com